Experimental investigation
of VO_2-based field-effect devices

Marco Lanzano

Experimental investigation of VO_2-based field-effect devices

Von der Fakultät Mathematik und Physik der Universität Stuttgart
zur Erlangung der Würde eines Doktors
der Naturwissenschaften (Dr. rer. nat.) genehmigte Abhandlung

vorgelegt von

Marco Lanzano

aus Neapel, Italien

Hauptberichter:	Prof. Dr. J. Mannhart
Mitberichter:	Prof. Dr. P. Michler

Tag der mündlichen Prüfung: 27. September 2016

Max-Planck-Institut für Festkörperforschung, Stuttgart
Abteilung Mannhart

2016

Contents

Acknowledgments

I would like to thank all the people that have contributed at the fulfillment of the work described in these pages. During these years at the Max Planck Institute I had the opportunity to grow both professionally and personally. I will always be grateful for this.

I thank Prof. Dr. Jochen Mannhart for giving me the possibility of being part of his group, for managing to create a relaxed and collaborative environment in the group and for the precious advices.

I would like to thank also Prof. Dr. Michler and Prof. Dr. Daghofer for accepting the role of external members of my Ph.D. examination committee. Thanks to Dr. Giuliano Gregori and Dr. Pavel Ostrovsky for being external supervisors during my Ph.D.

My colleagues at the Max Planck Institute have played a central role in the creation of this work through the exchange of knowledge and experimental support.

Thanks to Dr. Hans Boschker for constantly stimulating me in the process of the scientific reasoning, Dr. Jone Zabaleta for being always present in the time of need, Dr. Cameron Hughes for the initial guidance, Dr. Takayuki Harada for the open scientific discussions, René for having always time for answering my questions, Georg and Carsten for the precious introductions and explanations.

The technical support is a fundamental part of most of the experiments shown in this work. I am very grateful to Wolfgang, Manny, Ingo and Konrad for the constant availability and willingness. Thanks to Kazushiro Kawashima for letting me use his PLD system to grow the first samples, Yvonne Link for the ALD deposition, Marion Hagel for the bonding of all my samples, Achim Güth for the drawing of the optical masks, Ben Stuhlhofer for the technical support. The aid of Renate was also very important, especially to integrate myself in the new contest.

I acknowledge Daniel Pröpper for introducing me to the ellipsometry measurements, Vesna Srot for helping me with the TEM and EDX measurements, Helga Hoier for contributing to the XRD characterization of my samples and Bernhard Fenk for guiding me for the SEM measurements.

I believe that a part of this work has been possible also thanks to the personal relationships that have been built during my time at the MPI. Even if with different importance, I value every personal exchange. For this reason I thank all the people that have crossed my way in these years. Special thanks to the people that have been always there, no matter what. Truly thanks to Jone, Jelena, Yeliz, Aggelos and Cyril for sharing with me a part of them. Merci à Pierre pour la patience e le soutien. Grazie a Gianni, Flora e Chiara e a tutta la mia famiglia per non avermi mai fatto sentire solo.

Zusammenfassung

Die Oxide der Übergangsmetalle werden aufgrund ihrer vielfältigen physikalischen Eigenschaften von der wissenschaftlichen Gemeinschaft mit großem Interesse untersucht. Hochtemperatur-Supraleitung, kolossaler Magnetowiderstand und Zustände mit verschiedenen elektrischen und magnetischen Eigenschaften sind lediglich einige Beispiele der faszinierenden Verhalten, welche in dieser Klasse von Materialien auftreten. In Übergangsmetall-Oxiden ist die Kopplung zwischen Ladung, Spin und Orbital-Freiheitsgraden außerordentlich stark. Daher können die klassischen Methoden der Festkörperphysik das Verhalten dieser Materialien unter äußerer Stimulation nicht detailliert vorhersagen. Die starke Korrelation der Elektronen untereinander ist ein besonderes Charakteristikum dieser Materialien, welches sie gegenüber den normalen Metallen und Halbleitern abgrenzt.

Vanadiumdioxid (VO$_2$) erfährt einen Metall-Isolator-Übergang (metal-insulator transition, MIT) bei näherungsweise Zimmertemperatur. Die einzigartigen Eigenschaften dieses Übergangs haben Forscher sowohl aus Gründen des fundamentalen Erkenntnisgewinns als auch wegen der technologischen Anwendungen, welche diesen Übergang ausnutzen können, fasziniert. Frühere Studien von VO$_2$ zeigten, dass dem Metall-Isolator-Übergang ein struktureller Phasenübergang (structural phase transition, SPT) folgt und dass die starke Korrelation der Elektronen der hauptsächliche Grund für diesen Übergang ist. Daher kann VO$_2$ im isolierenden Zustand als ein besonderer Mott-isolator betrachtet werden. In den letzten Jahren wurde von einigen Gruppen die Möglichkeit angezweifelt, ein auf VO$_2$ basierendes Feldeffekt-Bauelement zu konstruieren, welches einen Mott Metall-Isolator-Übergang im Material hervorrufen kann. In einem solchen Gerät würde das Anlegen einer kleinen Gate-Spannung eine sehr schnelle und starke Änderung des Widerstands im VO$_2$ –Kanal hervorrufen. Die Auswirkung

dieses Bauelements auf die moderne Technologie wäre substantiell, daher ist es von großer Wichtigkeit die Physik hinter dem Verhalten von VO_2 bei diesen Bedingungen zu verstehen. In der vorliegenden Arbeit untersuche ich das Verhalten mittels gepulster Laser-Deposition (pulsed laser deposition, PLD) gewachsener dünner Schichten von VO_2 auf unterschiedlichen Substraten, welche in die Konfiguration eines electric double layer transistor (EDLT) strukturiert wurden. Im Gegensatz zu herkömmlichen Transistoren wird beim EDLT das Gate vom Kanal durch ein flüssiges Elektrolyt getrennt anstatt durch ein festes Oxid. Auf diese Weise wirkt auf den Kanal ein stärkeres elektrisches Feld für geringere Gate-Spannungen. Jedoch muss die Reaktion des Elektrolyts auf das elektrische Feld und die Wechselwirkung zwischen Elektrolyt und Kanal-Material in Betracht gezogen werden, um die Leistung des Bauelements verstehen zu können. In dieser Arbeit untersuche ich die strukturellen und Transport-Eigenschaften dünner Schichten von VO_2 und zeige den Unterschied zwischen Schichten, welche auf dem oft verwendeten Substrat TiO_2 gewachsen wurden und solchen, welche auf dem Perovskit $LaAlO_3$ (111) gewachsen wurden. Im letzteren Fall nimmt der Film eine auffällige körnige Struktur an. Die Dichte und Größe der Körner kann mit den Depositionsparametern verändert werden; jedes Korn erfährt einen MIT und eine Perkolationsschwelle wurde für den MIT der gesamten Schicht gefunden. Die Kornstruktur beeinträchtigt das Verhalten des VO_2-basierten EDLT. Die Analyse dieses Verhaltens und der Vergleich mit dem Verhalten auf anderen Substraten gewachsener dünner Schichten unterstützen die Diskussion über die fundamentalen Ursachen des Feld-induzierten Phasenübergangs in VO_2. Insbesondere wird die isolierende Phase nicht wiederhergestellt wenn das Elektrolyt nach dem Gating von der Schichtoberfläche entfernt wird, was auf irreversible Veränderungen der Schichtstruktur hinweist. Dieses Verhalten wurde ebenfalls in auf Al_2O_3 $(10\bar{1}0)$ gewachsenen Filmen gefunden, nicht aber in auf TiO_2 (001) gewachsenen. Das unterschiedliche Verhalten wird den unterschiedlichen Filmeigenschaften wie Stress-Relaxation und Oberflächen-Rauheit, welche die Interaktion zwischen Schicht und Elektrolyt beeinflussen, zugeschrieben.

Die Messung der spektralen Zustandsdichte (density of states, DOS) eines Materials ist ein wichtiges Werkzeug um die elektronische Phase dieses

Materials präzise zu charakterisieren. Insbesondere für Übergangsmetall-Oxide ist die Modifikation der Besetzung der Energiebänder der Hauptgrund für die verschiedenen Verhalten dieser Materialien, denn sie beeinflusst die Stärke der Korrelation zwischen den Elektronen. Die Zustandsdichte kann durch Tunnelmessungen bestimmt werden. Der Tunnelstrom hängt von der Zustandsdichte der Konstituenten des Tunnel-Bauelements ab. Durch die Messung des Tunnelstroms durch die Tunnelbarriere kann die Zustandsdichte bestimmt werden. In einigen Fällen, wie z.B. bei VO_2, ist es notwendig die Zustandsdichte an der Seite zu messen, welche der der Umwelt ausgesetzten Seite gegenüber liegt um zwischen den Effekten des ausgedehnten Körpers und der Dünnschicht einerseits und durch externe Faktoren erzeugten Oberflächeneffekten andererseits unterscheiden zu können. Übergangsmetall-Oxide als Tunnelbarrieren sind jedoch eine ungewöhnliche Methode zur Messung der Zustandsdichte, da es schwierig ist diese Materialien mit hinreichenden strukturellen und Transporteigenschaften für Tunnelbarrieren zu wachsen. Die Eigenschaften von Übergangs-Metalloxiden als Dünnschichten sind besonders empfindlich gegenüber den Depositionsbedingungen und es ist daher eine Herausforderung, Barrieren ohne Defekte für verlässliche Tunnelmessungen zu erstellen. In dieser Arbeit untersuche ich das Wachstum mittels PLD von Übergangsmetall-Oxid-Dünnschichten für Tunnelbauelemente. Ich konzentriere mich insbesondere auf Oxide mit Rutil (001)- und Perovskit (111)-Struktur. Entlang der [111]-Achse orientierte Perovskite finden aufgrund ihrer einzigartigen Kristallstruktur wachsendes Interesse in der Forschergemeinschaft. Die Kopplung zwischen elektronischen und Gitter-Eigenschaften ist entlang dieser Kristallrichtung verstärkt und die Oberfläche besitzt eine hexagonale Symmetrie, welche topologisch äquivalent zur Oberfläche von Graphen ist. Aufgrund der Abfolge geladener Gitterebenen entlang der [111]-Kristallachse baut sich an der Oberfläche eine hohe Energiedichte auf. Aufgrund dessen neigt die Oberfläche zu Rekonstruktionen und das Wachstum von (111) Perovskit-Dünnschichten mit einer flachen und makellosen Oberfläche ist daher eine gewisse Herausforderung. Ich identifizierte einen durch die Kompensation der hohen Oberflächenenergie induzierten allgemeinen Wachstumsprozess, der verschiedenen (111)-Perovskiten gemeinsam ist. Ich verglich die strukturellen und Transporteigenschaften verschiedener Metalloxide und Oxidsysteme zur

Benutzung als untere Elektrode in einem Tunnel-Bauelement. Mir gelang es, kristalline Schichten mit einer reduzierten Rauheit für alle Materialien der Studie herzustellen. Materialien wie RuO_2 (001) und $SrRuO_3$ (111) stellten sich als wegen der hohen Flüchtigkeit von Ru besonders empfindlich gegenüber den Depositionsparametern heraus. Die Porosität des für die Deposition verwendeten Targets begünstigt die Ablagerung großer Partikel welche diese Materialen trotz ihrer hohen Leitfähigkeit als Unterelektroden ausschließen. Nb-dotierte Substrate werden durch die Bildung großer Inseln auf der Oberfläche aufgrund von Defekten im Substrat und Nb-Segregation beeinträchtigt. Durch die Verwendung von $La_{0.7}Sr_{0.3}MnO_3$ (111) und des 2D-Elektronensystem an der Grenzfläche zwischen LaAlO3 und $SrTiO_3$ (111) als Unterelektrode und einem dünnen Film von $LaAlO_3$ als Tunnelbarriere wurden erfolgreich Tunnel-Bauelemente mit nichtlinearen Strom-Spannungs-Kennlinien in Übereinstimmung mit dem Brinkman-Dynes-Rowell-Modell hergestellt.

Introduction

The rapid development of modern technology requires a continuous improvement of the performance of electronic devices. This can only be pursued through a thorough understanding of the fundamental behavior of the materials employed to build the technology. The growth rate of the number of semiconductor devices on an integrated circuit predicted by Moore´s law has undergone a reduction in the last years[1] since, despite the use of novel techniques, fundamental limits related to the material and to the basic functioning of the devices are difficult to overcome.[2] For the post-Moore era, new materials have been introduced whose physical behavior is not completely described by the classical theories of solid state physics and manifests itself in exotic properties that can be exploited to build advanced electronic devices. A very common example is NiO, which is expected to be a conductor according to the classical band theory but which shows insulating antiferromagnetic behavior. NiO belongs to the large family of transition metal oxides.

Transition metal oxides are particularly interesting because of the wide range of properties that they can show. One can find compounds with metallic or insulating behavior, superconductors with a very high critical temperature, ferromagnets showing colossal magnetoresistance as well as antiferromagnets, ferroelectrics, ferrielectrics, ferroelastics and multiferroics [for a review see ref. 3]. The rich physical behavior of the transition metal oxides is mostly due to the unique environment in which the electric charges reside. The chemical bonds between the *d*-orbitals of the multivalent transition metals and the *p*-orbitals of the highly electronegative oxygen anions form energy bands with narrow widths and strong directionality. Thence, the coupling between the charge, spin and orbital degrees of freedom is particularly strong. These compounds can show different available electronic configurations, a large electron-electron and electron-lattice interaction, confined electronic systems, etc.

Numerous transition metal oxides belong to the group of “correlated materials” and a small variation in their atomic composition can lead to very different behaviors. A variation of the degrees of freedom can be induced externally by applying electric and magnetic fields, by modifying the ambient conditions such as temperature and pressure, by doping with a different material, etc. This way, a switch between two phases can be prompted, enriching the possible applications of transition metal oxides e.g. in the fields of optics and electronics. To facilitate the use of the devices built from this class of materials, it is important to integrate these materials with conventional semiconductors, which form the core of today´s electronics. In 2013, researchers at the IBM Zurich Laboratory reported an electro-optic device made out of a thin film of $BaTiO_3$ grown on a silicon substrate.[4] The integration of transition metal oxides in form of thin films in the existent semiconductor industry, together with the exciting physics that they show, opens a new avenue in technological advance.

The growth of transition metal oxides in the form of a thin film on a single crystal substrate gives the possibility to tailor the properties of the material by defining the crystal structure and direction, the uniaxial strain, the chemical composition and the film thickness. Pulsed laser deposition (PLD) is a suitable growth technique to produce crystalline oxide thin films, allowing for the control of the film stoichiometry, the film growth mode and the film thickness. The film growth takes place far from thermodynamic equilibrium, i.e. the structural and electronic properties of the film much depend on the kinetics of the deposition. With PLD, in addition to transferring the stoichiometry of the chemical compound from the target to the substrate, it is possible to modify the defect concentration in the film by adjusting the deposition conditions, for instance the substrate temperature, the gas pressure during growth or the laser fluence. For example, a metal-insulator transition has been induced in anatase TiO_2 thin films by modulating the growth rate, which in turn influences the amount of oxygen vacancies present in the film.[5]

The unique properties of vanadium dioxide (VO_2) make it one of the most intriguing transition metal oxides. VO_2 is a correlated material exhibiting a metal-insulator transition (MIT) near room temperature. The metal-insulator transition is driven by the strong correlation between the electrons in the *d*-orbital of vanadium and is accompanied by a structural modification which changes drastically the energy band diagram of the material. The detailed description of this transition has been the object of study for many researchers in the last fifty years and remains an open question.[6–8] Meanwhile, novel products and devices exploiting the transition in the optical and transport properties have been suggested, such as coatings for smart windows that reduce house energy consumption. The metal-insulator transition has been induced also via the application of an electric field in a transistor-like device using either an oxide layer or an electrolyte as a gate.[9–12] In the latter case one speaks of electric double layer transistors (EDLTs). EDLTs having VO_2 as a channel material have shown a unipolar field-effect transition with large on/off amplitude.[11] One of the explanations for the electric-field-induced transition considers that a Mott transition takes place at the surface of the thin film of VO_2 and expands throughout the whole film thickness.[11] In this case, one speaks of Mott field-effect transistors (Mott-FETs). The potential of such a device is outstanding since an intrinsic bulk reaction would be induced via a surface stimulation. This is drastically different from what happens in Si-MOSFET and can tackle the modern limits of electronic devices regarding feature size, switching speed and power consumption. A number of experiments performed on VO_2-based FETs, however, point to the formation of oxygen vacancies in the VO_2 channel as the source of the metallic behavior.[12] These results also indicate that the behavior is strongly dependent on the substrate on which the thin film of VO_2 is grown since the film properties and the film reaction to an applied electric field vary according to the substrate crystal structure and orientation.[13] Clarifying which phenomena are responsible for the electric-field-induced MIT (E-MIT), distinguishing between a surface and a bulk transition, is of fundamental importance to endorse a possible use of VO_2 in next-generation electronics.

The measurement of the spectral density of states (DOS) through tunneling transport is a very powerful tool to characterize in detail the electronic nature of a material. In recent studies, tunnel junctions have been built, for example, to measure the superconducting energy gap of $NbSe_2$[14] and of the 2D electron liquid at the interface between $LaAlO_3$ and $SrTiO_3$.[15] Despite the simplicity of the measurement, the production of a working tunneling junction is a challenging task, especially when transition metal oxides form the junction because of the large sensitivity of their properties to structural defects. The large potential of such a powerful tool with broad, possible applicability to characterize this varied class of material, however, motivates the investigation of the construction of all-oxide tunnel junctions, of which not many examples exist in the literature.

In this work I will investigate the PLD growth of different oxide layers to be used as electrode and as tunnel barriers for an all-oxide tunnel junction. I will concentrate on oxides with rutile structure along [001] direction and with perovskite structure along [111] direction since these systems are compatible with the growth of epitaxial crystalline VO_2 thin films and can contribute to elucidate the unresolved issues concerning this material. The growth and characterization of (111) perovskites, in particular, represents a hot topic because of the honeycomb lattice structure that is observed along this crystal orientation. This structure is topologically equivalent to the lattice of graphene. Topologically non-trivial states, such as Chern insulators, have been predicted for transition metal oxide perovskite oriented along the [111] direction, but have not been confirmed experimentally so far. I will show that the PLD growth of (111) perovskites has a general trend common to all the tested materials that is different from the growth process along [001] direction. I will compare the electronic properties of the materials adopted as bottom electrode and as tunnel barrier and test a possible device for tunnel transport measurements.

In parallel I will investigate the properties of VO_2 thin films grown on two different substrates, the rutile TiO_2 (001) and the perovskite $LaAlO_3$ (111), as well as the different performances of the EDLTs built out of the VO_2 thin films in the two cases. In particular, I will show that VO_2 on $LaAlO_3$ (111) grows in completely relaxed 3D grains aligned along three preferential directions, each grain undergoing a MIT with temperature. The thin films were patterned in EDLT configuration. The devices were working at room temperature, unlike the cases found in literature so far. The comparison between the performances of such a device and the ones made using different substrates gives important indication about the behavior of VO_2 during the E-MIT. Moreover, the fabrication of a VO_2-based field-effect device on a perovskite substrate favors the integration of this interesting material in the semiconductor industry.

Chapter 1

1. Theoretical background

Vanadium dioxide is a good example of the interesting properties that oxides can show. In this material the atomic structure as well as the electron distribution plays a fundamental role in the determination of its transport properties. In this chapter I will expose the reasons why vanadium dioxide attracted the attention of scientists in regard to the theory describing the material´s behavior and the technological applications. I will, then, explain the latest theory that is considered to describe the material and I will conclude with the description of the application of interest for this work, the electric double layer transistor. The deep understanding of these kinds of devices based on vanadium dioxide, in fact, could define the future of this material in oxide electronics.

1.1 Vanadium oxide

Vanadium(IV) oxide (VO_2) started to catch the interest of scientists after the discovery of its metal to insulator transition (MIT) in 1954.[16] This result was confirmed by Morin for single-crystal samples.[17] Morin measured the conductivity in dependence of the temperature for different oxides of vanadium and titanium (Fig. 1.1). VO_2 showed a MIT together with V_2O_3 and VO. The MIT in V_2O_3 and VO shows very large relative amplitude (above five orders of magnitude) and a small switching time.

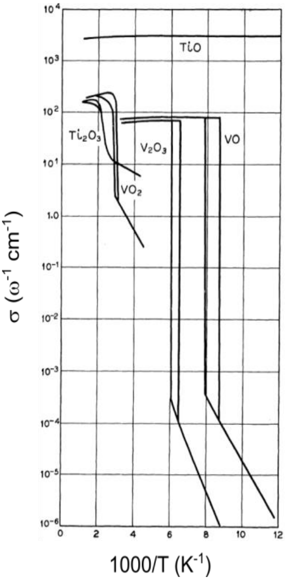

Figure 1.1 Conductivity as a function of reciprocal temperature for the lower oxides of titanium and vanadium. Adapted from ref. 17.

However the transition temperature T_c for single-crystalline VO_2 is above room temperature unlike the other two vanadates ($T_{c\ V_2O_3}$ = 159 K; $T_{c\ VO}$ = 120 K). This peculiar characteristic of VO_2 makes this material very interesting for optical and electronic devices requiring a switching behavior. After Morin´s discovery a dense literature about VO_2 has been produced. As time goes by the description of the MIT has been enriched with the findings of multiple structural phases and possible correlation-driven mechanisms taking place during the transition. This increased the interest about the basic physics behind the MIT in VO_2 in addition to the possible applications; VO_2, in fact, could shed some light on the behavior of highly correlated transition metal oxides. Despite the progress in the knowledge of VO_2, though, the picture is not yet fully complete keeping alive the interest about this material.

1.1.1 The metal-insulator transition in VO_2

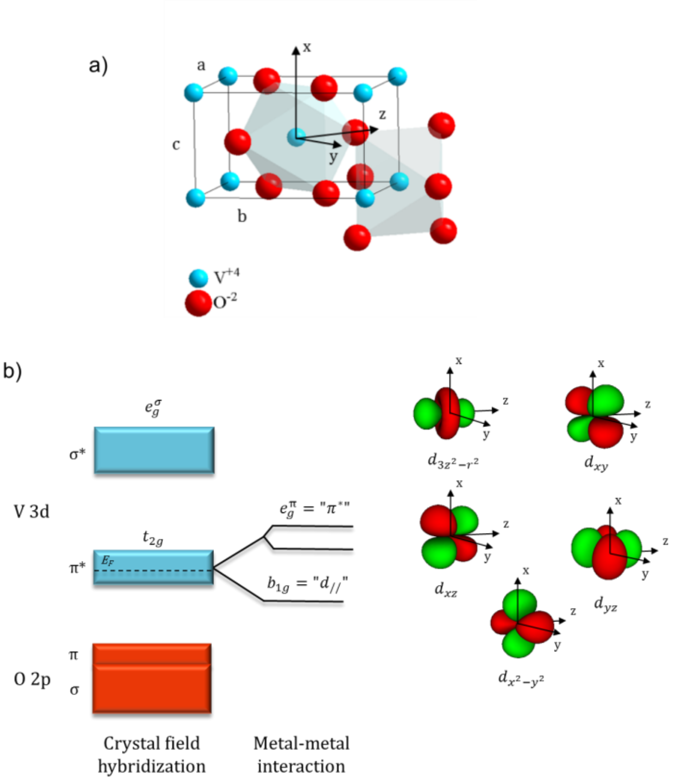

Figure 1.2 (a) Sketch of the rutile unit cell of VO_2 with two octahedra centered on neighboring vanadium ions. (b) Cartoon of the energy bands of VO_2 in rutile phase as described by Goodenough.[6] The degeneracy is partially lifted by the Crystal field and by the V-V interaction.

Single-crystalline VO_2 undergoes a first-order MIT at T_c ~ 340 K.[17] The properties of the transition for the bulk VO_2 depend on the quality of the crystal but, on average, the relative resistance jump from insulating to metallic phase can reach a value $\Delta R/R \approx 10^5$; the transition shows an hysteresis with a width $\Delta T \approx 10\,\mathrm{K}$ with the insulator-to-metal transition happening at higher temperature; the transition time was measured through different pump-and-probe experiments and was found to be $t_T \approx 100\,\mathrm{fs}$.[18] Together with the MIT, VO_2 undergoes a structural-phase transition (SPT) passing from tetragonal (P42/mnm) rutile structure at high temperature to monoclinic (P21/c) structure at low temperature. The rutile structure can be pictured like a body-centered tetragonal lattice formed by the vanadium ions with each ion surrounded by an oxygen octahedron (Fig. 1.2a). The symmetry is lower compared to the perovskite structure since the oxygen octahedron is not pointing in the [001] direction (*c* axis) and the octahedra relative to neighboring (001) chains of V ions are pointing in different directions. During the SPT, two types of distortions lead from the rutile to the monoclinic phase: an alternate pairing of the V atoms along the tetragonal *c* axis and a lateral zigzag-like displacement (Fig. 1.3). These displacements double the unit cell bringing to a lattice parameter $a_m = 2\,c_r$. The lattice constants for both structures are summarized in Table 1. Here we notice that, according to the common representation found in literature, the lattice parameter c_r in the rutile phase becomes the lattice parameter a_m in the monoclinic phase. In order to avoid confusion, we will refer always in this work to the lattice parameters of the rutile phase (for example, when mentioning the doubling along the *c* axis). For a more precise description of the two structures, the reader can refer to reference 7. The characteristics of the transition for thin films of VO_2 are similar to the ones measured for the bulk crystal and have been found to be stable after as many as 100 temperature cycles.[19] Nonetheless the transition properties are very sensitive to the substrate and the growth conditions used. They can, then, be tuned changing the stoichiometry and the structural characteristics of the thin film. For example the transition temperature decreases when the crystal is subject to tensile strain. This has been achieved growing thin films of VO_2 on a piezoelectric substrate[20] or doping the material with tungsten.[21]

Together with the crystal structure, the energy spectrum changes accordingly. Goodenough gave already in 1971 an almost complete picture of what happens during the transition using a molecular orbital description.[6] He started the description of the transition from the rutile phase. The crystal field hybridization between the oxygen *2p* and vanadium *3d* orbitals will lead to σ- and π-type overlap. This gives rise to states of σ and σ^* as well as π and π^* character (Fig. 1.2b). Since the *p-d* overlap is stronger for the former, these states experience the larger bonding-antibonding splitting. While the σ and π states will be filled and primarily of O *2p* character, the corresponding antibonding bands will be found at and above the Fermi energy. In the nearly perfect cubic octahedral surrounding of the vanadium atoms, the σ^* and π^* states are of e_g^σ and t_{2g} symmetry, respectively. In order to identify these orbitals we use the local coordinate system centered at each metal site but rotated 45° respect to the local *z* axis in order to have the *x* and *y* axis parallel and perpendicular to the rutile *c* axis, respectively. It may be, moreover, useful to notice that the octahedron orientation is different to the one in a perovskite structure. Then the orbital energy distribution will result slightly different. In this system the orbitals with higher energy are $d_{3z^2-r^2}$ and d_{xy} since they point directly to the oxygen atoms while the ones with lower energy are $d_{x^2-y^2}$, d_{xz} and d_{yz}. The orthorhombic distortions of the oxygen octahedral lift the degeneracies among the *d* orbitals. The exact position and width of the *d* bands is subject not only to the *p-d* hybridization but also strongly influenced by direct metal-metal interactions. In particular, in the rutile structure such interactions involve the $d_{x^2-y^2}$ orbitals, which experience strong overlap parallel to the rutile *c* axis. These orbitals are of b_{1g} symmetry but the band they form is usually designed as the $d_{//}$ band. The remaining t_{2g} orbitals are of e_g^π symmetry and usually subsumed under the name π^*. During the SPT driving to the monoclinic phase, the pairing of the V atoms causes a splitting of the $d_{//}$ band while the zigzag-like displacement provokes a shift upward of the π^* band (Fig. 1.3). The final result is the formation of a band gap $E_g \sim 0.6$ eV.[22]

Despite the difficulties related to Hall measurements of VO_2 thin films,[23] it has been found that the carrier density varies across the transition from a value $n_\mathrm{i} \approx 10^{19}\mathrm{cm}^{-3}$ in the insulating phase to a value $n_\mathrm{m} \approx 10^{23}\mathrm{cm}^{-3}$ in the metallic phase. The mobility does not change much during the transition staying around the value $\mu \approx 0.1\ \mathrm{cm}^2 / \mathrm{Vs}$. The dielectric constant varies accordingly from a value $\varepsilon_\mathrm{i} \approx 36$ to $\varepsilon_\mathrm{m} \approx 10000$.[24]

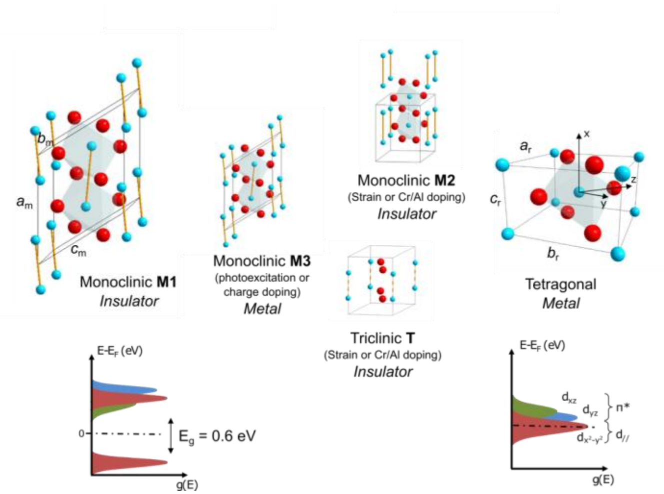

Figure 1.3 Representation of the different phases adopted by VO_2 in different conditions. The SPT with temperature brings from the monoclinic M1 phase at low temperatures to the tetragonal phase at high temperatures. For the former, the pairing of the V atoms and the zigzag-like displacement is shown. Other three intermediate phases can be isolated: the triclinic and moniclinic M2 through application of strain or chemical doping, the monoclinic M3 through photoexcitation or charge doping. The modification in the density of states g(E) due to the SPT is pictured. At low temperatures the π^* band shifts and the $d_{//}$ band splits forming an energy gap.

	a	b	c	α
Monoclinic M1 [25]	5.74 Å	4.52 Å	5.38 Å	122.6°
Tetragonal (rutile) [26]	4.56 Å	4.56 Å	2.85 Å	/

Table 1: Lattice parameters along the three main directions of the unit cell for VO_2 in the monoclinic M1 and tetragonal phase. α is the angle between the axis a and c of the monoclinic phase.

1.1.2 Application of VO_2 in optics and electronics

One of the most intriguing application exploiting the MIT in VO_2 is the thermochromic coating for the so-called "smart" windows. The latter are windows covered with a material that changes its optical property with temperature in order to reduce energy dispersion. In particular VO_2 switches from a phase having high transmittance in a big range, comprising visible and near-infrared range, at low temperatures to a phase having significant transmittance in the visible range and high reflectance in the near-infrared at relatively high temperatures. This would prevent the temperature in a room to increase excessively in summer and to decrease in winter, saving energy.[27,28] In addition, leading the transmitted infra-red light to lateral solar panels, energy can be generated.[29] Vanadium oxide is also been used as a recording medium for holographic double-exposure interferometry in the femtosecond time domain,[30] optical switches and fibers,[31] scan lasers,[32] bolometers,[33,34] nanomechanical resonators,[35] microactuators.[36] Together with applications profiting from the abrupt changes in the optical and mechanical properties happening during the transition, it is important in this thesis to talk shortly about possible applications in electronics exploiting the change in transport properties of VO_2 across the transition.

Oxide electronic devices are good candidates for the next generation devices circumventing the fundamental limits encountered in Si-based electronics. In particular, the main target of the electronics industry is to find materials that combine the advantages of nonvolatile memories such as flash memories and volatile memories such as static random access memories. For this purpose, a class of cheap materials which have easy scalability and rapid programming speed in addition to non-volatility and low power consumption must be developed. Oxide based devices can avoid traditional density limitations since they can be fabricated at relatively low temperatures and thus formed in 3D stack structures. Additionally, the intriguing physics driving the different phases that they can acquire can be used to build fast, non-volatile and low consuming devices. Threshold switching oxide devices, for example, show very near ideal behavior for non-ohmic devices, turning nearly completely off for bias below the threshold voltage V_{th} and having negligible resistance for bias greater than V_{th}. VO_2 has been used as a selector in such devices together with NiO used as non-volatile memory allowing fast programming speed of tens of nanoseconds.[37] Key advantages of using VO_2 for electronic applications are its metallic "On state" allowing higher drive currents than semiconductors, its very fast transition, its relatively low latent energy, its full volume transition implying good scalability and reliability and its potentially large metallic/semiconducting resistance ratio up to five orders of magnitude. Besides for nanoscale selectors,[38] VO_2 has been used to build memristors[39] and as a channel in two and three terminals FET. For two terminals devices, the predominant phenomena driving the transition ON/OFF is a local Joule heating.[9,40,41] For three terminals devices the effect should be exclusively electrostatic if the current in the VO_2 channel is relatively low.[10] In this case different processes can play a role, e.g. a charge doping due to atomic ionization or to chemical reactions and a Mott transition. The latter phenomena, on which the Mott-FETs are based, will be treated more accurately in the paragraph 1.2.2.

1.2 VO_2: a complex Mott insulator

Understanding what happens to the material during the transition and, in particular, what is the primary physical reason of the transition is of fundamental importance in order to control the transition with external stimuli different from temperature variations and use it for applications. The two main theories considered by the community to explain the MIT in VO_2 are the one that considers monoclinic VO_2 like a Peierls insulator and the one that considers it like a Mott insulator. In the first case the structural modification, in particular the pairing and the consequent doubling of the cell, would be the cause of the gap opening.[6,42] In the second case the correlation among the electrons confined in the narrow $d_{//}$ band after the shift of the π band would be the cause of the gap formation.[43] Very many papers have been written in order to try to solve this riddle. Theoretical calculations as well as experimental results have enriched the scenario with new intermediate phases and mixed behaviors. One of the few beliefs reached so far is that it is not possible to place VO_2 in only one of the two pictures since the behavior seems to be much more complicated. As a confirmation of this it is enough to say that neither the density functional theory (DFT) within the local-density approximation (LDA) nor theories considering the correlation among the electrons (like LDA+U) were able to describe completely the experimental findings related to the different phases of the material.[7,44,45]

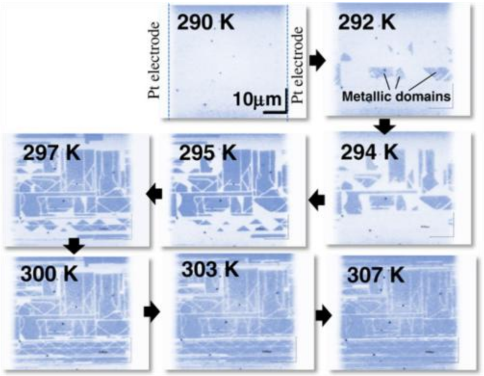

Figure 1.4 Optical microscope images of a VO_2 thin film during heating from 290 K to 307 K. The gradual formation of metallic domains is observed. Adapted

1.2.1 Experimental findings

In this paragraph we will report just some of the experimental results that have to be considered in order to have a complete view of the physics around the MIT in VO_2.

- Other two insulating low-temperature phases of VO_2 have been discovered. The two phases have a triclinic structure and a monoclinic structure slightly different from the monoclinic phase (M1) found in normal conditions at low temperature; for this reason they are denoted T and M2 and appear on doping or applying uniaxial pressure.[46–49] In the M2 phase the V chains along the *c* axis don´t show both the displacements present in the M1 phase. Alternatively, in one chain the V ions dimerize and in the other chain the V ions move following zigzag-type deviations. The T phase represents an intermediate step between M1 and M2 as those chains, which in the M2 phase dimerize, gradually start to tilt, whereas the zigzag chains start to dimerize. Despite the different structure, VO_2 in M2 and T phase is still insulating.

- The MIT induced by a temperature change proceeds through processes of nucleation and growth. The temperature at which a microscopic domain of a different phase nucleates depends on the strain to which the material is subjected. Bulk VO_2 is rather uniform and the transition is, therefore, almost abrupt; VO_2 thin films, instead present stress inhomogeneity. By increasing the temperature, then, the formation of microdomains is observed, for example, by optical microscope (Fig. 1.3). This behavior can be observed also in the measurement of the resistance against temperature if these microdomains are big enough to provoke micro-scaled transitions.[36]

- The oxygen ambient conditions during the growth of thin films of VO_2 affect the MIT. In particular, reducing oxygen partial pressures conditions result in the disappearance of the MIT.[52,53]

- The other rutile-structured transition metal dioxides (NbO_2, MoO_2, WO_2, etc.) show a similar double distortion of the rutile structure when the temperature changes but most of them stay metallic across the whole range of temperature. In MoO_2, for example, contrary to VO_2, the oxygen atoms follow the metal ion shifts during the transition (in VO_2 they stay almost at their original position). In MoO_2, then, there is no change in the metal-oxygen bonding strength after the effective shift of the anions respect to the oxygen and this seems to prevent the opening of the gap. MoO_2 has the electronic configuration $4d^2$ for the last occupied level and it shows metallic behavior at all temperatures. On the other hand, NbO_2 which has configuration $4d^1$ shows the MIT.[7]

- The MIT can be induced also through optical stimulation. With ultrafast pump and probe experiments it has been possible to study this transition in details. The main achievement of this kind of transition is the temporal decoupling of structural and electronic phase transition in VO_2.[54–56] In particular, the isolation of an additional intermediate phase M3, structurally equivalent to M1 but metallic, has been possible. The interpretation of the experimental results is the following: the photoexcitation of electrons results in a depletion of electrons in the bonding states which are critical for the V-V dimerization and, consequently, the insulating behavior of the monoclinic phase. An increase in laser fluence brings to a weakening and subsequent breaking of the V-V pairs, causing the collapse of the gap and the formation of the metallic phase. Electron-lattice coupling and thermalization eventually remove the zigzag arrangement of the V atoms bringing the crystal to rutile structural phase.[57] If the laser fluence is low enough so to overcome the critical density of electronic excitations but not the critical density of phonon excitations, only the reorganization of electron occupation of the orbitals along the 1D V chains is induced and the rutile phase is never reached.[8,58,59] For a better understanding of what will be treated in this thesis, it is important to separate the processes leading to the MIT induced by a light source from those leading to the MIT induced by a temperature change or by the application of an electrostatic field; nonetheless, from this measurement it is clear how sensitive VO_2 is to variations of the dynamically screened Coulomb interaction.

1.2.2 Peierls vs Mott insulators

Peierls demonstrated that a one-dimensional array of atoms having a partially filled conduction band cannot behave like a metal at $T = 0$. In fact, the system will go through a spontaneous modification of the periodicity of the structure in order to lower its total energy. In a 1D array of atoms having a half-filled band, for example, the distance among the atoms could change in such a way to create pairs of atoms with a double periodicity respect to the single atom array. This would then move the boundary of the Brillouin zone at the half of the energy band, opening a gap at the Fermi level and making the material insulating. The periodic modulation of the atomic positions is also known as charge-density wave. In three-dimension, however, the Fermi surface is usually a sphere and consequently it is almost impossible to have a deformation with spherical periodicity. Nonetheless, in materials presenting high anisotropy and quasi-1D band structures, a temperature driven Peierls transition could take place.

Another type of insulators is the Mott insulator. Contrary to the Peierls insulators, the Mott insulators cannot be understood only on the basis of the interaction of independent electrons with the electrostatic field of the ions in the crystal, but it is necessary to consider the electron-electron interaction. This kind of insulators started to be studied when compounds that were predicted to be metallic according to the band theory behaved indeed like insulators. In 1937, in particular, in order to find a reason for the insulating behavior of the transition metal oxide NiO having a half filled energy band at the Fermi level, Mott suggested that “it is quite possible that the electrostatic interaction between the electrons prevents them from moving at all”.[60] Hubbard introduced the on-site Coulomb interaction U among electrons in the description of a system composed by atoms having one electron per unit cell. According to the Hubbard model, the competition between the electron hopping process between nearest neighbors and the on-site Coulomb repulsion determines the insulating or the metallic character of such a system. Formally the Hubbard Hamiltonian can be written like

$$H = -t \sum_{\langle i,j\rangle,\sigma} (c^{\dagger}_{i\sigma} c_{j\sigma} + h.c.) + U \sum_{i} n_{i\uparrow} n_{i\downarrow} \qquad (1)$$

Here U is the intra-atomic Coulomb interaction $\langle e^2/r_{12}\rangle$ and t is the hopping integral that is proportional to the orbitals overlap integral and the kinetic energy of the carriers. The bracket ⟨i,j⟩ restricts the sum to nearest-neighbor pairs (i; j). The operator $n_{i\sigma} = c^{\dagger}_{i\sigma} c_{j\sigma}$ measures the occupancy of the site i with electrons of spin σ. Consequently $n_{i\uparrow} n_{i\downarrow}$ is the double occupancy, i.e. its expectation value corresponds to the density of double occupied sites. Inter-site Coulomb interactions are omitted due to the screening effects. Multibands effects are also neglected since the degeneracy is partially lifted by the crystal field for the systems under analysis.

Using the Hubbard model[61] it is possible to give a good description of the insulating phase, getting to the conclusion that an insulator to metal transition should take place when the condition $U \approx t$ is satisfied. This means that the system with half filling and narrow bands will behave as an insulator if the Coulomb repulsion between electrons sharing the same orbital is stronger than the kinetic energy, namely the probability that the electrons tunnel between atoms. This condition sets a critical charge density n_c that is needed to induce in the system in order to prompt the transition.

$$n_c^{1/3} a_H = 0.26 \tag{2}$$

Where a_H is the Bohr radius.

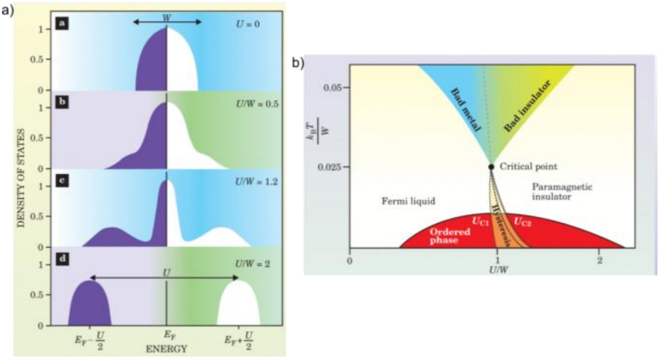

Figure 1.5 Density of states (a) and phase diagram (b) calculated in dynamical mean-field theory for a system at half filling and zero temperature represented in the Hubbard model.[62] *Changing the ratio between U and W in (a) it is possible to observe the transition from the metallic phase to the insulating phase, the extinction of the quasiparticle peak and the formation of the Hubbard bands. DMFT predicts a first-order transition line (dotted line in (b)) ending at a critical point above which a gradual crossover from metal to insulating phase takes place.*

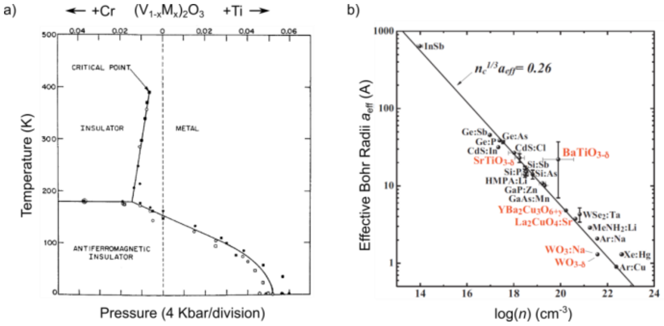

Figure 1.6 (a) Phase diagram for V_2O_3 as obtained in ref. 63. *The plot in (b) represents the critical density for the MIT in some materials with certain effective Bohr radius a_{eff}; it suggests a rather universal behavior of the Mott condition since many different kind of coumpounds seem to fit onto the line, from rare-gas solids to semiconductors to oxides. The mechanism behind the transitions, though, could be very different among them and not always requires strong correlation among the electrons (From the work of Lee et al.* [64,65]*).*

Starting from the atomic limit (t = 0), it is easy to visualize the energy spectrum at the Fermi level for a system of atoms with one electron per unit cell. The addition of one more electron to the system requires an energy U. The latter will then be placed in a level distant U from the ground state. If the electrons start to hop around ($t \neq 0$) the upper atomic level broadens into a tight binding band of width $W = 2zt$ (z is the number of nearest neighbors). The same happens if one adds a hole to the system. This brings to the situation sketched in Fig. 1.5 with two bands of states with same width W separated by a band gap $E_g = U - W$. These two subbands are called lower and upper Hubbard band. The transition to metal phase, then, can be induced either moving the Fermi level so to cross one of the bands (filling-control MIT) or reducing the bang gap (bandwidth-control MIT) until the condition $U_{c1} \approx W$ is satisfied. Despite the confirmation obtained experimentally, the Hubbard model does not give a fulfilling description of the metallic phase. In 1970 Brinkman and Rice, building on the work of Gutzwiller, proposed a different model starting from the metallic phase which is described as a renormalized Fermi liquid. In particular, the mass renormalization is indicated by the quasiparticle residue Z according to the relation $m^*/m = 1/Z$. As the interaction increases, Z decreases until a critical value U_{BR} for which $Z \propto (U_{BR} - U) \approx 0$ and $m^*/m \to \infty$. Correspondently the quasiparticle peak at the Fermi level tends towards a delta function. The condition for the metal to insulator transition in this case is $U_{\mathrm{c2}} \approx 1.68\,W$.[66] In this framework, the metal to insulator transition is driven by the localization of the Fermi-liquid quasiparticle. This approach is a consistent low-energy description of the strongly correlated metal, but does not account for the high-energy excitations forming the Hubbard bands, which should be present already in the metallic state. At low enough temperature an antiferromagnetic insulating phase is expected according to what predicted by Slater.[67] The doubling of the unit cell, in fact, due to a long-range antiferromagnetic order makes the band structure of the system that of a band insulator. The dynamical mean-field theory (DMFT) was able to unify these different theories modeling the full solid with an effective atom hybridized to an energy-dependent bath. DMFT solutions of a half-filled system at zero temperature and subject to intra-site Coulomb interaction predict the formation of both a quasi-particle peak (for smaller values of U/W) and of the Hubbard bands (for bigger values of U/W) with an intermediate phase in the energy range $U_{\mathrm{c1}} < W < U_{\mathrm{c2}}$. Figure 1.5 shows the transition in the Density of States (DOS) and the phase diagram obtained with DMFT.[62] The actual metal-insulator transition at finite temperature is first order, and takes place for values on the dotted line where the free energies of the two solutions at U_{c1} and U_{c2} cross. At very low temperature, the system has long-range order (magnetic or orbital); at high temperature, above the critical point, a simple crossover from metal to insulating phase takes place. Systems as diverse as vanadium oxide alloys, nickel selenium sulfide, and organic materials exhibit the same qualitative behavior. Figure 1.6a shows the experimental phase diagram of V_2O_3 as a function of doping with Cr or Ti and as a function of pressure.[63,68]

This model, and in particular the condition (2), has been proved valid for many different materials (Fig. 1.6b). Transition metal oxides are among these since, despite semiconductors, the band width of the *d* and *f* energy levels are of the same order as the energy gaps. These kinds of highly correlated materials, then, are very sensitive to any modification to the charge carrier density. The latter can be modified changing the lattice parameter via strain or pressure thus changing the overlap among the electronic orbitals (bandwidth-control) or via electrostatic carrier doping (filling-control). Unlike semiconductors, in these materials the density of states changes with doping concentration. This happens because the number of possible ways in which a single electron can be adjusted in the system depends on the number of electrons already present in the system. In this way, if one adds m holes to the N sites system with one electron per site, the upper Hubbard band (related to the doubly occupied states) would have a total DOS of $N - m$ while the lower DOS would change to $N + m$. This change in DOS is called spectral weight transfer and is a trademark of correlated systems.

Thanks to this high sensitivity to external stimuli, correlated materials give the chance to observe unexpected behaviors that can be profitable for application in many different fields. For example, a FET based on a correlated material has a different behavior respect to a semiconductor-based FET. In typical FET devices, the field effect originates from the control of the Fermi energy in the rigid band structure. By contrast, in a Mott insulator, doped carriers increase the screening of Coulomb interaction, resulting in reduction of the effective Coulomb repulsion energy. The energy dependence of the density of states is hence coordinated with the doping concentration so that the charge gap collapses as the critical density is reached. In a Si-MOSFET the insulating state is understood in terms of strong Anderson localization. Application of a gate voltage changes E_F but does not alter the energy dependence of the DOS (rigid band model). On the other hand, a sufficient shift of the chemical potential (band-filling) reduces the effective Coulomb repulsion energy in a Mott insulator; this modifies the profile of the DOS in such a way that the charge gap collapses.

1.2.3 Two-stage correlation-triggered transition in VO_2

As it has already been said, it is not possible to understand completely VO_2 using only one of the two models described in the previous paragraph. Furthermore, since the time scale of the important processes is extremely short, it results difficult experimentally to isolate the primary cause of the MIT in this material. The theory that is getting a foothold in the community is the one considering the MIT in VO_2 as a correlation-triggered transition. The correlation among the electrons seems to have an important role in the insulating state and only when this interaction is damped down by, for example, increasing the temperature, the SPT and consequently the collapse of the energy gap can take place. Gray *et al.*[69] managed to identify, through XAS measurements, an energy peak located at the bottom of the upper Hubbard band that disappears for temperatures slightly lower than the T_c at which the MIT and SPT take place. They interpret this peak as the fingerprint of the electronic correlation within the V-V dimers. In fact the peak is found only for the spectrum related to the vanadium chains along the *c* axis. This is a clear indication of the necessary role played by the electronic correlation in setting the insulating phase.

The idea that the transition in VO_2 occurs in two stages, one related to the damping of electron correlation and one related to the structural deformation, was already suggested, among others, by Pergament in 2003.[70] In particular he brought forward an analogy between the MIT in transition metal compounds and the transition taking place for superconductors (SC). In the SC phase, the characteristic scale length of the system is the coherence length that is directly related to the energy gap width Δ. At a critical temperature electron-electron Cooper pairs form, having a radius equal to the coherence length. For transition metal compounds one can introduce a correlation length characterizing the "electron-hole pairs" forming in the insulating phase as a result of the MIT. The term "electron-hole pairs" should be considered with a broad meaning comprising all the electron-ionized center couples. One can consider that the MIT for transition metal compounds takes place when the carrier concentration is high enough to ensure that the screened Coulomb potential leads to no bound state. This means that the Debye screening length L_D has to be the same as the correlation length ξ. Starting from the Mott criterion (2) and considering a gap width Δ for the Mott insulator equal, in first approximation, to the energy of ionization of a hydrogen-like impurity, Pergament obtained the following relation between the correlation length and the energy gap

$$\xi = 2\hbar v_F / (3\pi^2)^{1/3} \Delta \qquad (3)$$

where the Fermi velocity $v_F \sim (n_c)^{1/3}$ corresponds to the metal state because in the insulating phase there are no free charge carriers and v_F is not defined. The relation (3) is very similar to the same kind of relation for SC. In this way it is possible to give an approximate estimate of the length related to the different energy gaps taking part in the MIT of VO_2.

The analogy between MIT materials and SC, however, is not absolute; in fact, while for superconductors $\Delta \sim T_c$, for MIT materials $E_g \neq T_c$. For example in VO_2 the energy gap width is $E_g = 0.6$ eV and $k_BT_c = 0.03$ eV. This is the reason why Pergament talks about a two-stage transition, one related to an energy $\Delta_c = k_BT_c$ and another one related to the energy $\Delta_s = E_g$. In particular the first should be the correlation-induced contribution to the bigger subsequent energy change induced by the structural deformation. Using E_g of VO_2 in (3) one obtains $\xi_s \approx 1.62$ Å which is a reasonable value for the localization radius in VO_2 since the atomic radius of vanadium is $R = 1.34$ Å and the mean distance V-V is $d \approx 3$ Å. ξ_s gives a good description of the system in the insulating phase. Using k_BT_c in the same formula one obtains $\xi_c \approx 15.7$ Å which is interpreted as the correlation length that is needed to screen ($L_D < \xi_c$) in order to trigger the MIT.

1.3 VO_2-based Electric Double Layer Transistors

As described in the previous paragraphs, the controlled alteration of the electron system equilibrium and, in particular, of the charge density, could induce a MIT in a VO_2 crystal. The electrostatic charge doping is one of the possibilities to achieve this and is the basis of potential electronic devices based on VO_2. As it has already mentioned in paragraph 1.1.2, three-terminal devices using VO_2 as a channel has been already built and have demonstrated the possibility to induce a resistance change in the channel, although much lower than the change induced via a temperature change. Studies with typical deposited solid-gate dielectrics on VO_2 thin-films have been challenging because of gate leakage currents that can cause self-heating and affect the MIT, the limited annealing process windows for process devices, etc. Inhomogeneity and grain boundaries can complicate the matter. Ruzmetov *et al.*[10] measured that, applying +5 V gate bias through a SiO_2 dielectric layer, the channel conductance increases with time and the magnitude of the effect depends on the electrical and thermal measurement history. The relatively high carrier density observed via Hall measurements suggests that VO_2 has a very short screening length ($\lambda \approx 1$ nm[23]) that limits the electrostatic gating efficiency, confining the effect of the gate to an extremely thin channel layer.

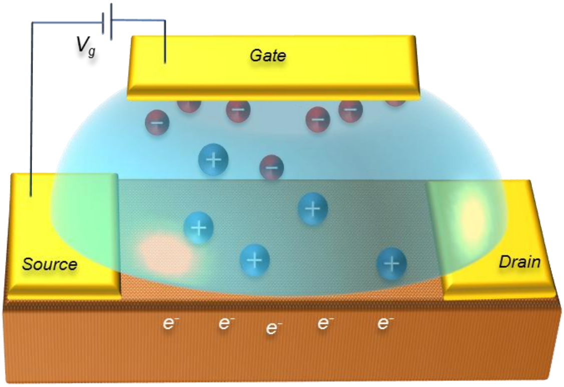

Figure 1.7 Schematic of an EDLT with top gate configuration. A drop of ionic liquid puts in communication the gate electrode with the channel. Source and drain contacts are used to characterize the transport properties of the channel. The accumulation of positive (in this case) ions on the surface of the channel induces the electrostatic accumulation of electrons at the surface of the channel.

1.3.1 EDLTs

In the last years, VO_2 has been used as a channel material in Electric Double Layer Transistors (EDLTs). These novel transistors have a similar geometry to the more common MOSFET, made of source, drain and gate contact; the main difference is that an ionic liquid (IL), a polymer electrolyte or an ion gel instead of a gate oxide is used to put in contact the gate contact and the channel (Fig. 1.7). The latter two are hybrids in that they are polymer ion combinations. We will focus for the rest of the thesis on ionic liquids. An IL is a salt in a liquid state that is mainly made of ions and shortly-lived ion pairs. It is, effectively, a solvent-free electrolyte. When an electric field is applied across the IL, the ions move until they form a double layer capacitor with the two electrodes at the borders. The advantage of using an IL is that, even if the IL has a relative permittivity of 1-10, the double layer capacitance is extremely high ($C \approx 20$ µF/cm^2) since the distance between the two faces of the capacitor is extremely small ($d \approx 1$ nm). Very large electric fields are created at the interface of the electric double layer (EDL) but, unlike conventional capacitors, the chemical stability of the IL's molecular bonds prevents breakthrough. In IL based EDLTs, then, it is possible to accumulate with a lower applied gate voltage a higher carrier density ($n \sim 10^{15}$ cm^{-2}) at the liquid/channel interface compared to the case of the MOSFET geometry (a 300 nm thick layer of SiO_2 has a capacitance of 10 nF/cm^2, so that a typical sheet carrier density would be only ~ 10^{13} cm^{-2}). Unlike the chemical doping, the electrostatic doping through IL allows to dope a material in a continuous and reversible way, without, in principle, altering the level of disorder and regardless of the kind of material forming the channel and its crystalline orientation. The carrier density modification is confined within the electrostatic screening length that can be of the order of few unit cells. It may be important, then, for the material in the channel to be very thin otherwise the unperturbed bulk properties could affect the thin layer at the surface like for the proximity effect in the superconductors. The charge transfer can be changed only when the ions of the ionic liquid are mobile. The phase of the ionic liquid changes with temperature; then, the transfer can take place only in a restricted temperature range above the solidification temperature. The change of ionic mobility with temperature has to be taken into account since it affects the time constants of the gating processes. The processes taking place at the interface between the IL and the channel material are not fully understood. First of all it may be difficult to ensure an impurity-free interface at the level possible for vapor-deposited gate insulators. Then the IL has a stabilization window for the gate voltages applied across the interface. Above the limits of this windows Faradaic reactions start to play an important role in the process. From the experiments it is clear that the dynamics strongly depend on the IL and the channel material used and that even using voltages inside this windows, unipolar effects, oxygen vacancies formation, etc. can take place. However, ILs are much more stable compared to electrolyte solutions of organic solvents and water. In particular they are non-volatile and nontoxic so to be considered as “green solvents”.[71] Their low molecular weights and high polarizabilities, then, makes them much more conductive than conventional electrolytes giving the possibility of fast operation speed on the order of up to MHz.[72] The first report on ionic-liquid EDL-FETs of organic semiconductors appeared in 2008[72] while for oxides it was used to induce or modify superconductivity in $SrTiO_3$, $KTaO_3$, $La_{2-x}Sr_xCuO_4$, $YBa_2Cu_3O_7$, La_2CuO_4 and InOx.[73] The possibility of patterning thin layers of IL favors the production of flexible transistors using ion gels on a plastic substrate.[74]

Various models have been proposed to describe the interface between a general electrolyte and a solid. The model fitting a particular system depends on the properties of the electrolyte. They are sketched in Fig. 1.8. The Helmholtz model[75] assumes the presence of an EDL formed by a single ion layer in solution, adsorbed on the solid surface, and a charged layer in the solid until a depth equal to the screening length. It can be formalized by a capacitor. The Gouy-Chapman model[76,77] considers the potential in the IL to decrease exponentially going far from the interface, letting the ions to diffuse. This model does not work for highly-charged EDLs. The Gouy-Chapman-Sterns model[78] combines the first two models. The latter works for dilute electrolytes. For molten salts the multilayer model[79,80] seems more suitable since it considers the polarization in the bulk IL due to the rigid disposition of the ions.

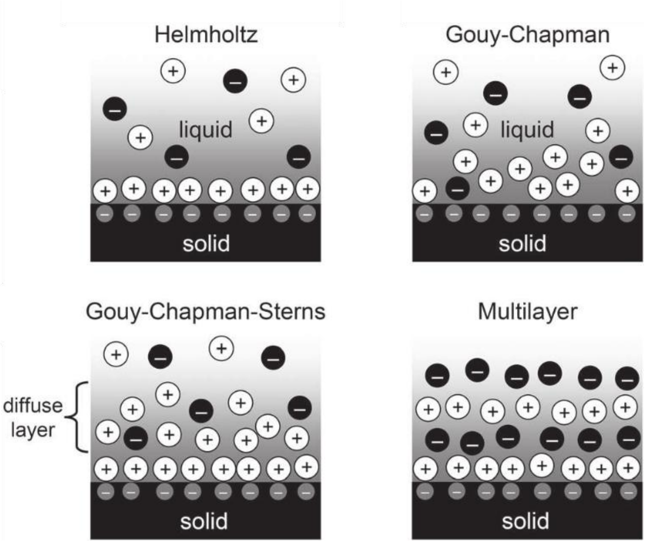

Figure 1.8 Sketch of the different models proposed to describe the interface electrolyte-solid in the work of Fujimoto et al.[81]

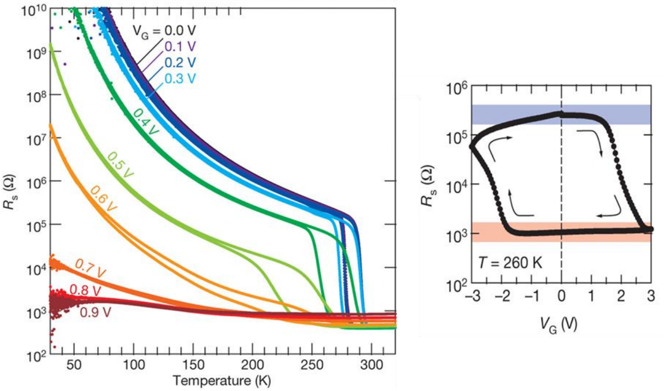

Figure 1.9 Measurements of the sheet resistance of a thin film of VO_2 *in EDLT configuration as a function of temperature for different* V_g *applied through the drop of the ionic liquid (a) and as a function of* V_g *at the fixed temperature T = 260 K (b).From the work of Nakano et al.* [11]

1.3.2 VO_2-based EDLT: an intriguing device

VO_2-based EDLTs were first studied by Yang and Zhou in 2012.[82,83] They observed a unipolar field-effect for positive bias (positive ions accumulated on the VO_2 surface) and a resistance change of $\Delta R/R \approx 20\%$ - 60% of the VO_2 channel for gate voltages $V_g = 2$ V. This process happens over a considerably long time (few hours). For negative voltages Faradaic currents are observed. Ji *et al.*[84] suggested that the small changes in resistance observed in the EDLT configuration are due to bulk electrochemical doping via hydrogen even if they find surprising the absence of an electrostatic gating effect at such high induced electric fields ($E = 10^9$ V/m at 1 nm from the interface).

After few months Nakano *et al.*[11] claimed that it was possible to induce electrostatically a bulk MIT in a thin film of VO_2 used as a channel for EDLTs. They grew a thin film of VO_2 on a substrate of TiO_2 and patterned it in a EDLT geometry with side gate. The IL used for gating the VO_2 is DEME-TFSI. Applying a gate voltage $V_g < 1$ V they were able to erase the insulating phase at low temperature. This is visible either from the measurement of the sheet resistance R_s with temperature for different V_g applied between the drop and the film or from the measurement of the R_s against V_g (Fig. 1.9). In the second case, when $V_g \approx 2$ V, a transition in the value of R_s of more than two orders of magnitude takes place. The electric-field-induced metallic state survives even when V_g is reset to zero, providing a non-volatile memory effect. The application of a negative V_g brings R_s to the initial value. They observe that the transition temperature T_c decreases with applied voltage and from Hall-effect measurements they observe that a much lower charge density is necessary to induce the transition compared to the chemical doping observed for $V_{1-x}W_xO_{2.}$[21] With these arguments they argue that "a collective lattice deformation along the *c*-axis direction and resultant delocalization of previously localized electrons in the bulk VO_2 film, leading to a 3D metallic ground state" takes place. Preliminary X-ray data support the electrostatically gated MIT being accompanied by a structural transition from a metallic tetragonal phase to an insulating monoclinic phase. The possibility of collective 3D behavior induced by a surface stimulus is an extremely attracting phenomenon that paves the way for interesting and novel application in electronics.

This interpretation, though, has been challenged by some following works that claimed that electrolytic gating leads not to electrostatically induced carriers but to the electric-field-induced creation of oxygen vacancies with oxygen migrating from the oxide film into the ionic liquid. Jeong *et al*.[12] performed the same experiment as Nakano *et al*. using two kind of substrates (TiO_2 and Al_2O_3) and different thicknesses. They varied the ambient condition and found the following results: after switching to the high-conductance state, the devices were stable with zero gate voltage for many days, even when the ionic liquid was removed completely (as verified by XPS measurements); films having the same crystal structure but grown on different substrates, then subject to different strains, showed the same behavior; the insulating phase could be recovered either by reverse gate voltages or by annealing in oxygen at $T \approx 200$ °C; XPS studies of the gated film found a reduction of the V oxidation state, suggesting the formation of oxygen vacancies; ^{18}O was incorporated within the VO_2 channel during reverse gating; the presence of oxygen in the chamber (P_{O2} = 150 Torr) prevented the transition even for V_g higher than the voltage at which the transition takes place in normal conditions (P_{O2} < 10^{-5} Torr). Structural analysis of the gated VO_2 thin film has followed in order to determine whether the electric-field-induced transition brings to the same metallic phase as the temperature-induced transition. HAXPES measurements[85] found for the gated VO_2 thin film a slightly modified monoclinic structure with an increased V-V distance, consistent with an oxygen reduction. This result was confirmed by in-situ synchrotron X-Ray diffraction and absorption experiments.[86] The V-V dimerization results to be reduced in the gated phase but not completely retained. Furthermore an expansion of the lattice along the out-of-plane direction takes place, contrary to the compression happening in the rutile phase. The structural changes are observed only in films in which channels formed from chains of edge-sharing VO_6 octahedra do not lie in the plane of the films. These are considered by the authors like the paths along which the oxygen migration takes place.

Chapter 2

2. Tunnel junctions for the characterization of the MIT in VO_2

The previous chapter concluded with the description of the controversial results about the electric-field-induced MIT in VO_2 used as a channel for an electric double layer transistor. Here I spotlight the importance of answering these open questions and I describe a possible experiment that would help to find the answers.

2.1 Time for VO_2-based next generation electronics?

Any device used to build a binary digital logic must show some properties such as non-linear transfer characteristic, power amplification, compatibility between input and output signal and feedback prevention. Nowadays, the building block of digital computation is the MOSFET with doped silicon as channel material. The performance improvements and the increase in integration densities reached in the last 40 years for the Si technology, however, are destined to slow because of some intrinsic limitations that are difficult to overcome. The limits regard mainly the miniaturization and the minimum power consumption of the devices. In particular, a feature size (the minimum length of the MOS transistor channel between the drain and the source) of few tens of nm and a gate oxide thickness of the same order have been reached today, but non-negligible off-currents and gate leakage currents make it difficult to reduce further these lengths. The energy necessary for a switching process is fundamentally limited by a thermodynamic limit present for any irreversible logic and due to the loss of information at every process and a quantum-mechanical limit on the minimum energy needed for a very fast switching process.[2] Another fundamental limit for Si-MOSFET is the subthreshold swing which indicates the gate voltage needed to change the current in the channel of one order of magnitude. It is related to the power needed for each switch. The subthreshold swing has a minimum value of 60 mV per decade for any transistor structure whose switching relies on the modulation of carriers injected from a material with thermally broadened Fermi function. The main sources of power consumption in real devices are the dissipation due to the load capacitance, the current flowing during the transition, the off-currents and the gate leakage currents. The minimum of the subthreshold swing limits the value of the threshold voltage triggering the switch and, consequently, the minimum power consumption.

Some of the limits described so far are strongly related to the working principles of the MOSFET and to the nature of the semiconductor itself. To push the technology further, a quest for new materials has started. In the last years, correlated oxide electronics have got ahead as a possible enhancement to semiconductor technology. This kind of material is known to show a large bouquet of behaviors when the charge density is varied.[87] Mott-Hubbard insulators belong to this class of materials and they attracted the attention of scientists because of the strong correlation among the electrons in the material that can induce collective phenomena, such as bulk metal-insulator transitions. In this case, in the insulating phase the electrons are concentrated around the ions because of the strong electron repulsion but a small variation of the charge density, via thermic, electric or magnetic stimulation, can induce an abrupt delocalization and a transition to a metallic phase. These materials represent good candidates for a binary logic. In the case of a Mott-FET, furthermore, the transition is related to an intrinsic process. This may create a larger number of free carriers compared to the Si-MOSFET case for lower gate voltage applied, allowing for larger signal amplification. Additionally, it may consent arbitrary scaling down of the channel dimensions. The fast and large amplification can allow for subthreshold swings below the fundamental limit for semiconductors. An example is represented by the Hyper-FET built by Shukla *et al.*[88] They used a channel of VO_2 in series to the channel of a common MOSFET in order to exploit the current amplification taking place across the MIT in VO_2 induced by the current flow. In this way, subthreshold swings well below the limit for simple MOSFETs could be reached. In such a two-terminal device, however, the collective nature of the MIT in VO_2 is not fully used since the transition is, most-likely, induced by local Joule heating due to the relatively large current flowing in the channel.

Electrostatic doping in three-terminal devices, on the contrary, is a way to induce the transition without varying the temperature and the internal disorder (as caused by chemical doping) of the material. We have already introduced the results obtained by Nakano *et al.*,[89] where a three terminals EDLT is used to induce a MIT in a thin film of VO_2. Nakano and his collaborators claim that the transition is electrostatic and that it applies to the whole film thickness. They imagine that a modification at the surface of the film rattles through it until the other side. This effect would be rather unique and would change drastically the output characteristics of a device.[90] Nonetheless, the use of an IL to trigger the transition adds variables related to the interaction liquid-solid. In particular, chemical reactions taking place at the interface could contribute to the observed phase transition in VO_2. In fact, the same ionic nature that makes correlated oxides so different to semiconductors, augments the possibility of defect formation. Many studies analyzing the surface of the thin film of VO_2 in EDLT after the phase transition have deduced an exchange of oxygen between the IL and the VO_2 along the 1D V-V chains.[12,85,86]

To understand if VO_2 can be a good candidate for the next generation of highly performing Mott-FETs, it becomes extremely important to distinguish between the processes that may take place when VO_2 is the channel material of an EDLT:

- bulk vs surface transition;
- collective Mott transition vs chemical processes.

A possible way to distinguish between the different processes is to measure the spectral DOS of VO_2 at the side of the thin film opposite to the interface liquid-solid. The spectral DOS is a measurement of the energy band profile of VO_2 after the transition. It would give the possibility to define the phase of the material at the bottom of the thin film, so to distinguish between a surface and a bulk modification and to determine the thickness dependence of the modification. It would also be possible to observe the formation of intra-gap states related to defect formation.

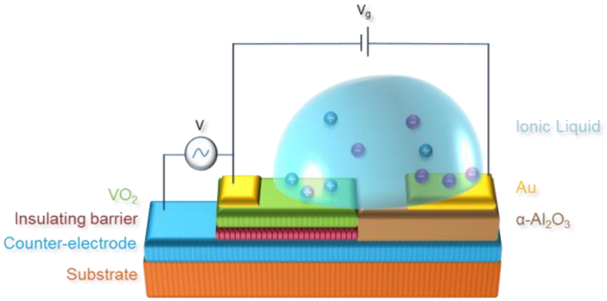

Figure 2.1 Sketch of the device designed to perform a measurement of the spectral DOS of VO_2 *after the electric-field-induced MIT.*

This could be achieved by building a tunnel junction having VO_2 as one of the electrodes. The measurement of the tunneling characteristic gives information about the convoluted DOSs relative to the two electrodes. If one of the electrodes has a constant DOS, the more elaborated spectral DOS of VO_2 can be obtained. Furthermore, if VO_2 is the last layer of the tunnel junction, its surface can be used as a channel for an EDLT. Figure 2.1 shows the sketch of the device suitable to perform such an experiment. An insulating barrier needs to be grown on a conducting substrate or on a counter-electrode grown beforehand. A thin film of VO_2 is then grown on the barrier. It is important that the parts of the multilayer are not damaged during the growth process in order to avoid the formation of defects that would make more difficult the determination of the DOS of VO_2. The heterostructure is patterned in such a way to have three independent contacts to the counter-electrode, to the thin film of VO_2 and to the drop of IL so to allow, at the same time, for tunneling transport measurements and for IL gating.

As described in the last chapter of this thesis, however, the fabrication of such a device is rather challenging and the patterning process may damage the extremely sensitive tunnel barrier, not letting the measurement of the DOS of VO_2. Nonetheless, the fabrication of transition metal oxide tunnel junctions represents a powerful and innovative tool to characterize this large class of functional materials. Additionally, the analysis of the behavior of VO_2 grown on alternative substrates to the ones found in the literature, favors the understanding of the phenomena taking place in the material during the E-MIT. The results of this investigation will be described in the next chapters.

Chapter 3

3. PLD growth of VO_2 thin films and (111) oxide heterostructures

In the previous chapter I have described the device that would provide a useful contribution for the discussion around the E-MIT in VO_2. In this chapter I will show the steps explored to grow the oxide heterostructure needed to build the device. I will first introduce the pulsed laser deposition, i.e. the technique that I used to grow oxide thin films, and then I will describe the results obtained for the growth and characterization of VO_2 on different substrates and for the growth of the bottom electrodes. In particular, this chapter consists of two main sections: in the paragraph 3.3.5 the peculiar 3D grain structure of a VO_2 thin film grown on $LaAlO_3$ (111) will be described in comparison with a thin film of VO_2 grown on a substrate of TiO_2; in the paragraph 3.4 the transport properties of possible electrodes for (111)-directed oxide devices will be compared.

3.1 Oxide materials for tunnel junctions

A tunnel junction consists of a thin insulating layer which separates two conducting materials. According to quantum mechanics, the electrons can pass through the insulating barrier, even if their initial energy is much lower than the first available energetic level in the barrier. In a general case, the two electrodes can differ but, in order to have tunneling, the resistance of the electrodes has to be negligible compared to the resistance of the barrier. Tunnel junctions can be used to characterize the energy band spectra of the electrodes since the tunneling current depends on the spectral DOS of the materials forming the junction (see the Appendix). Our intention is to measure the spectral DOS of VO_2, hence one of the electrodes of the junction is VO_2 which is an oxide showing metallic behavior only under certain conditions (high temperature, electric field gating, etc.). In the metallic phase, however, the resistance is larger than the resistance of a common metallic electrode. The tunnel barrier has to have a particularly high resistance at the working temperatures. It is also of fundamental importance that the barrier has a low percentage of defects, such as vacancies, pinholes and inhomogeneities, that can cause leakage currents through it, deteriorating the insulating character of the barrier. In our case, it will be enough to have a barrier resistance at least two orders of magnitude higher than the resistance of VO_2 in the metallic phase. The barrier is grown via pulsed laser deposition (PLD) on a conducting thin film or directly on a conducting substrate. Considering that the thin films grown via PLD have always a certain surface roughness, it is important to choose a group of material with a low lattice mismatch and with similar deposition conditions in order to grow the parts of the heterostructure in sequence and with the lowest possible amount of structural defects.

The first materials for the heterostructure electrode-barrier-electrode-substrate, that I explored, are VO_2 /TiO_2 /RuO_2 /TiO_2 (001). These are all binary oxides with rutile crystal structure and a very small mismatch. TiO_2 is a band insulator while RuO_2 has metallic character. However, as explained in paragraph 3.4.1, the best RuO_2 thin film that I was able to grow presented still a too large surface roughness to be used as an electrode for tunnel junctions.

The second sequence of materials that I thought could be used as a tunnel junction is VO_2 (010) /$LaAlO_3$ (111) /$SrRuO_3$ (111) /$SrTiO_3$ (111). Apart from VO_2, all the materials have a perovskite structure along [111] direction and a small mismatch. However, it is rather challenging to build a tunnel junction out of complex oxides since their properties are extremely sensitive to their structure and composition. Indeed, not many examples are found in literature of such a system.[91] For the system under study, the growth along [111] direction is complicated by the surface polarity of the materials. Nonetheless it would be of severe importance to demonstrate the availability of this kind of tunnel junction for the detailed analysis of correlated transition metal oxides, as in the case of VO_2. In the following paragraphs we will explain how the growth of each layer was performed showing, in particular, how the rutile VO_2 grows on the perovskite $LaAlO_3$ (111).

3.2 Pulsed laser deposition

Pulsed laser deposition (PLD) is a widely used technique for the growth of oxides, mostly because it allows for easy stoichiometric transfer, high flexibility and reproducibility. As in other physical vapor deposition techniques, a material in vapor phase condenses on the surface of a crystalline substrate forming a thin film. The way in which the vapor is formed and driven onto the substrate distinguishes the PLD from the other techniques. A highly energetic pulsed laser hits a solid target made of the desired elements in the correct stoichiometry. Usually UV excimer lasers with 10-100 ns long pulses are used. It is common practice to divide the processes taking place during the laser ablation into primary and secondary. The former consider the laser-target interaction with consequent formation of the vapor. The latter consider the laser-vapor interaction with modification of the vapor plasma. According to Chrisey and Hubler[92] the main mechanism of the primary process is the electronic sputtering which includes different forms of excitation or ionization of the target material. The result is that the system makes a transition from a tightly bound solid to a densely packed, repulsive gas where the particles have kinetic energies of a few eV, high directionality and varied composition. The secondary process consists mainly in the excitation of the particles forming the vapor, which can lead to particle collisions inside the plasma and with the target surface. The effect is similar to what happens after ion bombarding the target surface. Macroscopic particulate ejection can also arise in case of porous targets, since the localized laser-induced heating will cause very rapid expansion of any trapped gas pockets below the target surface and ejection of target material. The consequences of this effect will be shown later in this work.

Because of the pressure gradient, the plasma expands perpendicularly to the target surface. A reduced pressure gradient is also present in the in-plane direction and it affects the angular aperture of the plume in relation to the laser spot area on the target. In particular, the smaller the laser spot area, the larger the in-plane pressure gradient and the larger the angular aperture. The amount of material reaching the substrate depends on the laser spot on the target, in the case that the plume diameter at substrate position is larger than the substrate itself. During the expansion in the chamber, the plasma plume varies its shape, velocity, density and composition according to the background gas pressure in the chamber. Varying the deposition conditions such as laser fluence, laser spot area, gas type and/or pressure, target-to-substrate distance, substrate temperature, etc., the kinetic energy, the oxidation state and the aggregation of the species reaching the substrate (adatoms) can be varied.

The plume properties define the thin film growth and their relatively easy control makes PLD a particularly flexible technique. Furthermore, since the ablation time ($\tau_A \approx$ ns) is much shorter than the average diffusion time on the substrate surface ($\tau_D \approx$ μs), the two mechanisms can be easily distinguished, unlike molecular beam epitaxy (MBE) and sputtering deposition where the deposition is continuous. The nucleation and growth of the thin film is a non-equilibrium process and kinetics is important in the process. At first, the heterogeneous nucleation of the species in the plasma onto the substrate is driven by the need of minimizing the free energy of the vapor. In case of small or moderate supersaturation, meaning small nucleation rate, a simplified thermodynamic approach to the crystal growth is usually used. The morphology of the growing film is influenced by the competition among the free energies of the film surface (γ_F), the substrate surface (γ_S) and the interface film-substrate (γ_I). In particular, one can have: layer-by-layer growth (Frank-van der Merwe growth mode) if the total surface energy of the wetted substrate $\gamma_F + \gamma_I$ is lower than the surface energy of the bare substrate; island growth (Volmer-Weber growth mode) if the bonding between film and substrate is weak; layer-by-layer to island growth (Stranski-Kristanov growth mode) if the first layers of film form but then the growth proceeds with the formation of islands. In the case of PLD, the nucleation rate is rather large hence the diffusion of the adatoms on the substrate surface plays an important role. In this case, the thin film growth is influenced by a number of kinetic parameters, among which are the surface diffusion coefficient (D_S) of the adatoms, the sticking probability of an adatom arriving at the edge of a terrace of a vicinal substrate and the energy barrier for the adatoms to descend the edge to another terrace. These parameters depend exponentially on the substrate temperature and determine the relative influence on the growth of two main diffusion processes: the diffusion of atoms on a terrace (intralayer mass transport) and the diffusion of an atom to a different terrace (interlayer mass transport). According to the velocity of the two transport modes, the film can follow a step-flow growth mode, a layer-by-layer mode or an island growth mode. In this picture, the width and profile of the terraces influence the growth since the step edges are favorite nucleation sites. In heteroepitaxial growth the lattice parameter misfit and the difference in the thermal expansion coefficients between substrate and thin film can lead to formation of dislocations close or at the interface.

3.2.1 The PLD system

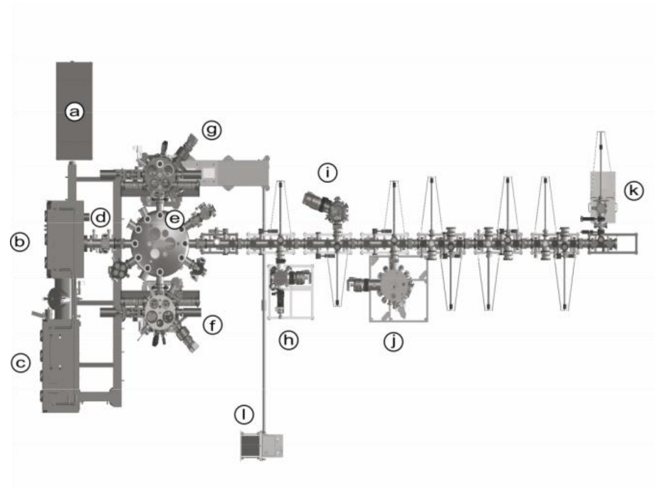

Figure 3.1 Sketch of the system for the growth and treatment of thin films: a) KrF laser, b-c) gloveboxes, d) loadlock chamber, e) transfer chamber, f) PLD1, g) PLD2, h) ion-milling machine, i) annealing chamber, j) e-beam evaporator, k) portable transfer chamber, l) CO_2 laser.

A big part of my work was devoted to the PLD growth of oxide thin films. For this reason, I will introduce the PLD system that I used. The PLD system consists of a PLD chamber provided with ultra-high vacuum pumps and RHEED system, a UV excimer laser (Coherent LPXpro, gas KrF, wavelength 248 nm, pulse duration 20 ns, energy stability 1%) and a laser beam path. A large part of the system was designed and produced in-house. This gave us the possibility to have a better control on the system so to optimize it. The PLD chamber is connected to other chambers for post-growth treatments via a transfer arm (Fig. 3.1). Keeping the sample under high-vacuum, then, it is possible to transfer it to an ion-milling chamber, an electron-beam evaporator, a sputtering chamber and an annealing chamber. We will be using these chambers for the device preparation as explained in chapter 4.

For the general operation of the pulsed laser deposition we refer to the text in reference 92. Here I present briefly some of the trademarks that belong to this system. The PLD chamber is connected to the external atmosphere through a chain of three chambers (a glove box filled with nitrogen, a load-lock chamber and a transfer chamber in ultra-high vacuum (UHV)) that guarantee an ultra-clean environment inside the chamber; the optical beam path has been designed so to have a spot profile on the target with uniform intensity for many different spot areas; precise substrate temperature control is achieved with two pyrometers measuring the temperature at the bottom and at the surface of the absorber on which the substrate is glued; the target ablation is driven by a software that allows to use all the functional area on the target and ensures that the plume is centered on the substrate for different target heights.

Some general preparation steps were followed for all the grown thin films. The target to be ablated was polished before each growth in order to ensure the same initial conditions for each deposition. The plume composition and direction, in fact, varies after multiple ablations in varied growth conditions. The treated substrates were glued with silver paste on a haynes block that works as an absorber for the infrared laser light used to heat the substrates with PID control until temperatures as high as 1000 °C. The silver paste ensures additionally good thermal contact between the absorber and the substrate.

3.2.2 Techniques for the characterization of thin films

Different techniques were used to characterize the substrate before the growth of the thin film and the thin film itself during and after the growth. For the intended experiments, we are mainly interested in their structural and transport properties. In the following we give some brief information about the techniques and devices used in this work.

Reflection high energy electron diffraction (RHEED): This technique is used to analyze *in-situ* the surface of a sample during the growth of a thin film. A highly energetic electron beam hits under a glancing angle the sample surface in the deposition chamber and is diffracted on a phosphorous screen. The RHEED pattern observed depends on the structure of the first surface layers of the material. In particular, it is possible to observe the substrate surface quality before the growth and to distinguish between the different thin film growth modes described in the previous paragraph. In case of ideal layer-by-layer growth, for example, the intensity of the RHEED spots forming the diffraction pattern oscillates between two values related to the conditions of maximum and minimum surface roughness. Each oscillation corresponds to the completion of a unit cell of thin film. For real samples, the maximum intensity decreases during growth because of the surface roughness building up with added layers. For a detailed description of the RHEED technique we refer to reference 93. I used a RHEED gun (Staib Instruments) with differential pumping so to follow the growth also at deposition oxygen pressures much higher than the pressure needed inside the gun ($P = 10^{-5}$ mbar).[94] The electron acceleration voltage used is 30 KV.

Atomic force microscopy (AFM): This technique is used to characterize the topography of a sample surface through the detection of the Van der Waals forces between a very small tip and the sample surface. This kind of scanning probe microscopy has a very high resolution (fraction of nanometers) since it does not suffer of optical diffraction limits. Furthermore it does not need particular environmental conditions in order to function. I used the atomic force microscope Cypher S by Asylum Research. The device has a particularly high stability and gives the possibility to get high speed images with atomic resolution.

X-ray diffraction (XRD): The atomic structure of a crystal can be characterized analyzing the diffraction pattern of an x-ray beam incident on the crystal surface. I used mainly the diffractometer Empyrean by

PANalytical. The incident beam has a wavelength of 0.154 nm (Cu K-α1 and Cu K-α2). I performed 2θ-ω scans, reflectivity scans and rocking curves in order to determine the thin film composition, the lattice parameter, the thickness and the level of homogeneity.

Scanning electron microscopy (SEM): It is another form of surface imaging that makes use of the interaction between an electron beam and the atoms of the sample. This interaction results in the reflection of high-energy electrons by elastic scattering, emission of secondary electrons by inelastic scattering and emission of electromagnetic radiation. Different materials as well as different incident angles will produce a different brightness of the detected signal. For this reason a surface image of the sample with three-dimensional appearance can be obtained. The SEM allows to image a relatively large area of the sample but the resolution is not enough to detect single atoms. Moreover, the sample has to have an electrically conductive surface and has to be kept under vacuum and dry during the measurement in order to avoid artifacts due to charging effects. I used a scanning electron microscope Merlin by Zeiss capable of electron acceleration voltages in the range [20 V, 30 KV] (For the following, $[x_1, x_2] \equiv x_1 \leq x \leq x_2$).

Scanning transmission electron microscopy (STEM): This microscope detects the electrons transmitted through a very thin sample that is hit by the electron beam. In this way, an image of the sample in cross section is obtained with atomic resolution. The machine used in this work is ARM-DCOR by Jeol. The machine is provided with an energy-dispersive X-ray (EDX) microscope to recognize the species constituting a small area of the material.

Ellipsometry: It is used to determine the optical properties of a thin film. Detecting the polarized electromagnetic radiation reflected on a film surface, one can measure the amplitude ratio Ψ and the phase difference Δ between reflected and incident beam. By modeling the system, then, it is possible to calculate the complex dielectric function ε. I used a Woollam VASE (variable angle spectroscopic ellipsometer) ellipsometer capable of measuring in the energy range [0.7 eV, 6 eV] and equipped with an ultra-high-vacuum cold-finger cryostat.

Physical property measurement system (PPMS): It consists of a nitrogen shielded helium dewar in which the sample is mounted. Transport properties such as resistivity, Hall constant, thermal conductivity, Seebeck coefficient, etc. can be measured while varying the temperature and the magnetic field. I used a PPMS by Quantum Design. During the measurement, the chamber is at a nitrogen pressure of 10 Torr. The temperature can be controlled in the range [1.9 K, 400 K] and a magnetic field up to ±9 T can be applied.

3.2.3 Substrates

Before growing the heterostructure for the tunnel junction, I needed to optimize the growth of each layer of the junction separately. Here I report the main properties of the substrates that were used for the growth of the thin films and their pre-growth treatments.

Titanium dioxide (TiO_2) has been widely used, especially in thin film form, for the conversion of solar energy,[95] as a gas sensor,[96] in integrated wave guides, for applications in medicine[97] and as coating for photocatalysis. TiO_2 films are used, for example, in self-cleaning windows for their photocatalytic oxidation of contaminants in air and of volatile organic compounds that are toxic to human life.[98] TiO_2 appears in five crystal structures but the naturally occurring polymorphs are rutile (tetragonal), anatase (tetragonal), brookite (orthorhombic) and TiO_2 (B) (monoclinic). Rutile is the most stable form of TiO_2 whereas anatase and brookite are metastable and transform to the rutile phase on heating.[99] In the rutile phase, TiO_2 has an indirect band gap of 3.0 eV[100] and a room-temperature dielectric constant above 100. For this reason it was proposed as high-κ gate insulator.[101] I used 5x5 mm^2 rutile (001) TiO_2 single crystals from Shinkosha as substrates. Even if the cut of a rutile crystal in (001) direction creates a non-polar, autocompensated surface, it does not represent a low-energy configuration.[102] Consequently the highly energetic surface tends to facet or reconstruct. This reconstruction prevents the observation of a single termination (one example is in Fig. 3.2). I annealed the TiO_2 substrates in 1000 °C for two hours in an oxygen flow of 250 ml/min in order to clean the surface.

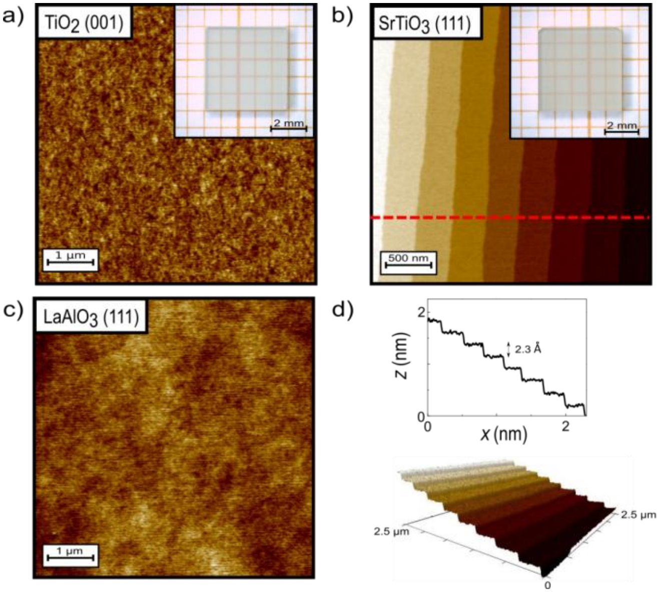

Figure 3.2 AFM topography (z = 1 nm) of the substrates used in this work. (001) TiO_2 *(a) and (111)* $LaAlO_3$ *(c) show flat surfaces (*RMS_{TiO2} *= 0.13 nm,* RMS_{LaAlO3} *= 0.11 nm). (111)* $SrTiO_3$ *(b) shows additionally a step-and-terrace structure. (d) Height profile along the red dashed line for* $SrTiO_3$ *(111) and 3D representation of the step-and-terrace structure. The height of the terraces is compatible with the nominal lattice parameter of (111)* $SrTiO_3$ *(Table 2).*

Strontium titanate ($SrTiO_3$) has been intensely investigated in the past years because of its interesting properties and because of its suitability to be used as a substrate for a large number of materials. It has, in fact, a small lattice mismatch and a chemical compatibility with many perovskite oxides and its surface termination can be controlled on atomic scale. $SrTiO_3$ has a cubic perovskite structure at room temperature (space group $Pm\bar{3}m$) and it undergoes an antiferrodistortive phase transition to a tetragonal structure (space group $I4/mcm$) at around 105 K. It is an incipient ferroelectric and remains paraelectric for $T \rightarrow 0$ K.[103] The dielectric constant increases with decreasing temperature going from 370 at 300 K up to 25000 at 4 K.[104,105] A "giant" piezoelectric response has been found for $SrTiO_3$ at very low temperatures.[106] Furthermore, by the application of stress it can be driven into a ferroelectric state at room temperature.[107] $SrTiO_3$ has an indirect band gap of 3.25 eV. This band insulator can be doped by introducing oxygen vacancies or atoms of La and Nb.[108] Superconductivity with critical temperature < 300 mK was observed for doped samples with charge carrier densities of 10^{19}-10^{21} cm^{-3}.[109–111]

Along the [001] direction, the single crystal can be pictured as a sequence of neutral planes SrO and TiO_2. It is possible to terminate a single crystal of $SrTiO_3$ with a TiO_2 plane using the recipe given in reference 112. The process consists in a series of chemical and annealing steps aiming at dissolving SrO from the surface and helping the remaining material to readjust in a flawless surface. After this treatment a step-and-terrace morphology is observed on the substrate surface. The vicinal angle under which the substrate is cut and the parameters of the treatment define the terrace width and form. One speaks of "meandering" if the edge of the terraces is not straight and of "bunching" if two or more terraces merge to form one higher terrace.

Along the [111] direction the crystal can be described as a sequence of the charged layers Ti^{4+} and SrO_3^{4-} . Unlike $SrTiO_3$ (001), $SrTiO_3$ (111) has a polar surface due to the surface dipole for either termination. Its divergent surface energy makes it difficult to obtain a well-defined surface without atomic reconstruction. However, using a method similar to the one employed for $SrTiO_3$ (001) it is possible to get a Ti^{4+} single termination.[113] A 5x5 cm^2 large (111) $SrTiO_3$ substrate by CrysTec was dipped in three successive ultrasonic baths of isopropanol, acetone and deionized water; it was then dipped in a buffered HF solution for 30 seconds and successively annealed in an oxygen flow of 250 ml/min at 1000 °C for two hours. Figure 3.2 shows the AFM topography of a $SrTiO_3$ substrate after the treatment. The step-and-terrace structure is observable and the height of the terraces equal to the height of the unit cell along [111] direction proves the single termination.

Lanthanum aluminate ($LaAlO_3$) has also been used as substrate because of its good lattice matching with many oxides.[114] It undergoes a structural phase transition between 400 °C and 500 °C[115] from cubic perovskite structure at high temperatures to rhombohedral $R\bar{3}c$ structure at room temperature. The low temperature structure differs from the cubic perovskite in an antiphase rotation of the AlO_6 octahedra. It can be described as pseudocubic with a lattice constant of 3.791 Å.[116] During the transition, twin domains appear to compensate the spontaneous strain. The twin domains are mainly along [100] and [110] directions and can be observed by an optical microscope since they result in a roof- and valley-like buckling of the surface. $LaAlO_3$ is a band insulator with a gap of 5.6 eV and it has a dielectric constant of 24 which makes it suitable for application in electronics, e.g. as a high-κ oxide.

(001)-oriented $LaAlO_3$ single crystals can be terminated just using an annealing process. They result with a AlO_2 single termination from room temperature up to ~ 150 °C, with a LaO single termination above 250 °C and with a mixed termination in the remaining temperature window.[115,117] This is considered to be due to the formation of oxygen vacancies at high temperature which would make the oxygen rich AlO_2 surface unstable. Along the [111] direction, $LaAlO_3$ consists of a sequence of Al^{4+} and LaO_3^{4-} planes. In the few papers reporting about the growth on $LaAlO_3$ (111), there is no mention about a pre-growth treatment of the substrate to obtain a single termination, apart from a pre-annealing in UHV to get a clean surface. We treated the substrates according to the recipe used for $SrTiO_3$ (111) but no step-and-terrace structure was visible but a rougher surface than for the as-received substrate. In order to clean the surface, however, the (111) $LaAlO_3$

substrates were pre-annealed at 800°C for 1 hour right before the thin film growth. Figure 3.2 shows an example of an annealed substrate.

	Material	**Structure**	**a (Å)**	**b (Å)**	**c (Å)**	**c_{111} (Å)**	**α**
Substrates	TiO_2[102]	rutile	4.58	= a	2.95	/	/
	$SrTiO_3$[118]	cubic	3.905	= a	= a	2.27	/
	$LaAlO_3$[116]	pseudocubic	3.79	= a	= a	2.19	/
Thin films	RuO_2[119]	rutile	4.49	= a	3.11	/	/
	$SrRuO_3$[120]	pseudocubic	3.93	= a	= a	2.27	/
	$La_{0.7}Sr_{0.3}MnO_3$[121]	pseudocubic	3.87	= a	= a	2.23	/
	VO_2[7]	rutile	4.56	= a	2.85	/	/
	VO_2[7]	monoclinic	5.74	4.52	5.38	/	122.6°

Table 2: Structure and lattice parameters of the bulk materials used in this work in form of single crystal substrate or thin film. c_{111} is the distance between planes along [111] direction and it has been calculated for the cubic structures. α is the angle between the axis a and c in the monoclinic phase of VO_2.

3.3 Substrate-dependent MIT properties of VO_2 thin films on TiO_2 (001) and $LaAlO_3$ (111)

The properties of a thin film of VO_2 depend strongly on the substrate adopted, in addition to the deposition conditions used. VO_2 grows in the (010)-directed monoclinic phase on the (0001)-plane and (1012)-plane of Al_2O_3, while it grows in the rutile phase on the $(10\bar{1}0)$-plane of Al_2O_3 and on TiO_2. VO_2 thin films deposited via PLD on (001) TiO_2 substrates have a reduced RMS roughness compared to the thin films grown on Al_2O_3 $(10\bar{1}0)$.[13,122] In some cases, VO_2 thin films grown on Al_2O_3 $(10\bar{1}0)$ consist of randomly directed, isolated grains.[123,124] The different film quality influences the transport properties and especially the way the thin film reacts to external stimuli such as electric fields, oxygen pressure, etc.[13] The films on TiO_2 (001), for example, are subjected to a compressive out-of-plane strain and the transition temperature of the MIT is ≈ 290 K. By contrast, the films on Al_2O_3 $(10\bar{1}0)$ are completely relaxed and show a transition temperature ≈ 340 K, close to the transition temperature for the bulk VO_2. The growth of VO_2 thin films on a substrate with perovskite structure such as $LaAlO_3$ may allow the use of the MIT in VO_2 for advanced electronic devices based on complex oxides. Despite the different crystal structure, VO_2 was successfully grown on $LaAlO_3$ (111).[125] It shows an in-plane three-fold symmetry and a MIT with temperature with a transition temperature ≈ 340 K. In the following paragraphs I will characterize in details the PLD growth of such a system stressing the dependence of the structure and the transport properties on the deposition conditions. The differences respect to the VO_2 films grown on TiO_2 will have effects in the electric-field-induced MIT, as will be shown in the next chapter.

3.3.4 Deposition of vanadium oxide

The family of the vanadium oxides is particularly large because of the many valence states of vanadium and because of the variety of possible ordered and disordered defect structures. Going from the vanadium oxide (VO) to vanadium pentoxide (V_2O_5) one passes through non-stoichiometric phases, Magnéli phases (V_nO_{2n-1})[126] and Wadsley phases (V_nO_{2n+1})[127] (Fig. 3.3). The Magnéli phases, for example, can be visualized to be composed of blocks of the parent rutile VO$_2$ lattice bounded by defect planes caused by the removal of every *n*th plane of anions. Each Magnéli phase undergoes a metal-insulator transition (except for V_7O_{13} which is metallic at all temperatures) but VO$_2$ has the T_c closest to room temperature (see Table 3).[126,128,129]

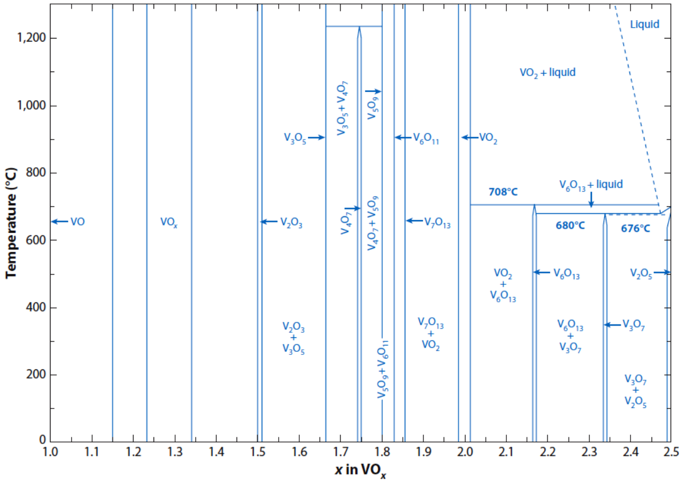

Figure 3.3 Phase diagram of the VO$_x$ system. The Magnéli phases are for $x < 2$, the Wadsley phases are for $x>2$.[130]

V_nO_m	V_2O_3	V_3O_5	V_4O_7	V_5O_9	V_6O_{11}	V_7O_{13}	V_8O_{15}	V_9O_{17}	VO_2	V_2O_5
T_c (K)	155	430	250	135	170	metallic	70	79	340	530

Table 3: Transition temperatures T_c of the metal-insulator transition for some of the vanadium oxides.[126] *In light blue the Magnéli phases are indicated. VO_2 has the closest T_c to room temperature.*

The existence of these competing oxide phases makes the growth of both bulk and thin films of VO_2 particularly challenging. Nevertheless, stoichiometric VO_2 has been deposited using several techniques such as reactive evaporation, several sputtering methods, metal-organic chemical vapor deposition (MOCVD), sol-gel deposition, pulsed laser deposition (PLD) and, recently, molecular beam epitaxy (MBE) and combinatorial deposition methods. The first deposition technique used for the deposition of VO_2 thin films appears to have been CVD in 1967[131] and this technique is still used nowadays for high quality thin films.[132] The sol-gel method has been widely used for depositing VO_2 films because of its low cost, suitability for large area deposition and the feasibility of metal doping. However, the RMS roughness of the thin films is rather large. When using sputtering techniques, the film uniformity and the scalability to larger substrates are the main advantages. PLD and MBE give the possibility to better control the valence state of vanadium through a precise control of the stoichiometry of the species reaching the substrate. The structural quality of the thin films grown by the latter two techniques is extremely high at the expense of a bigger, more complex and more expensive system. In general, the accuracy and versatility of PLD is convenient to study in details the physics of materials. The combinatorial approach, where a flux gradient across the sample is intentionally introduced during film growth to generate various growth conditions simultaneously at different sample locations, is also a possible tool to address the valence state control on a wafer-scale substrate.[133]

Ultrathin VO_2 thin films have been grown also by periodic annealing. This means that, after the deposition of half a monolayer of amorphous VO_2 at room temperature, an annealing at higher temperatures is performed in order to provide a high level of crystallinity.[134] The substrates used to grow VO_2 (001) are mainly the corundum Al_2O_3 cut along A-, C- and R- plane[135–139] and the rutile TiO_2 (001).[139-141] VO_2 (010) thin films have also been grown on spinel $MgAl_2O_4$, rocksalt MgO[143], wurtzite ZnO and perovskite $LaAlO_3$ and they also show the MIT with temperature.[125]

3.3.5 PLD growth of VO_2 thin films

I grew VO_2 thin films using the PLD system described in paragraph 3.2.1 on two different substrates: (001) TiO_2 and (111) $LaAlO_3$. For the application that these films are meant to have, a thin film will be considered of "good quality" when (*i*) the surface RMS roughness differs not too much from the substrate one, (*ii*) no additional phases other than VO_2 are observed in the XRD spectrum and (*iii*) the VO_2 thin film shows a rocking curve with a small full width at half maximum (FWHM), i.e. a large level of structural homogeneity. The analysis of the MIT is another tool to determine the quality of the thin film since a comparison to the MIT of the bulk VO_2 gives us information about the uniformity and the relaxation degree of the thin film. The quantities that characterize the MIT are: $\Delta R/R$, i.e. the relative resistance change between the two phases of the transition that represents the amplitude of the transition; T_c, i.e. the transition temperature; ΔT, i.e. the width of the transition hysteresis; dT, i.e. the FWHM of $d(\log R)/dT$ that represents the temperature interval that is needed to perform the switch. The mathematical definition of these quantities is explained in Fig. 3.4. The relative resistance change for the bulk VO_2 can reach five orders of magnitude but, for the thin film, it has not been measured above four orders of magnitude. The transition temperature is around 340 K for the bulk crystal[17] and depends on the strain for the thin film, namely on the substrate used for the growth. The transition width can reach values of 1 °C for the bulk[143] but it is in the range [5 °C, 10 °C] for the thin film. dT is a measure of the uniformity of the sample. If the thin film consists of many nuclei with different strain, the transition will be made of many micro-transitions at different transition temperatures. For this reason the transition will be broadened over a large range of temperatures and dT will be large. The thickness of the VO_2 thin films was obtained by the fitting of the XRD spectrum and the XRD reflectivity. As described in the previous paragraph, the annealing of a VO_2 thin film affects the thin film quality. The VO_2 thin films were annealed at the deposition conditions for 30 min after the growth.

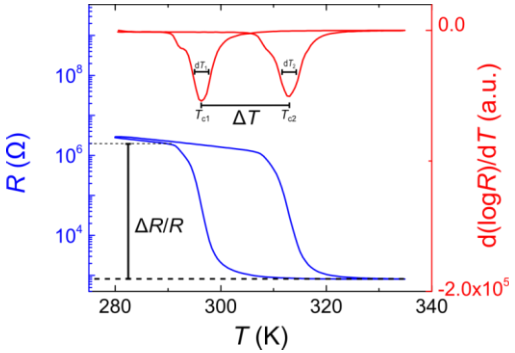

Figure 3.4 Resistance (blue) versus temperature of a 10 nm thick VO_2 film on (001) TiO_2 and respective derivative (red) of logR with respect to T. $\Delta R/R = (R_M - R_m)/R_m$ *, where R_M and R_m are the points where the two arms of the transition meet.* $\Delta T = T_{c1} - T_{c2}$ *, where T_{cn} is related to the peak of the Gaussian function fitting the nth peak of the derivative. T_c is the average between the two values. dT_{cn} is the FWHM of the Gaussian relative to the nth peak. dT is the average between the two values.*

VO_2 thin films on (001) TiO_2

I grew VO_2 thin films on a substrate of TiO_2 (001) using a sintered pellet of V_2O_5 from Toshima as a target. VO_2 and TiO_2 have a mismatch of 0.4% (see Table 2) and, at the growth temperature used in this work, they have the same rutile crystal structure. In order to optimize the growth, different deposition conditions were used. The oxygen pressure in the chamber was kept at 10^{-2} mbar, the substrate temperature varied in the range [350 °C, 450 °C], the laser fluence varied in the range [1.1 J/cm^2, 1.7 J/cm^2], two different laser spots on the target were used with areas 1.9 mm^2 and 5.3 mm^2 and the repetition rate was 2 Hz. The large variation of the deposition conditions aimed at getting a homogeneous sample with low surface roughness and, consequently, showing a MIT with properties similar to the ones for bulk VO_2.

From the analysis of the different samples grown, it is possible to observe that the properties of the MIT depend on the thickness of the thin film. Above a certain thickness, in fact, the film relaxes the strain and shows a degraded MIT compared to the MIT for bulk VO_2. Figure 3.5a shows the AFM topography of a 8 nm thick VO_2 film (identified as sample A) grown at the following conditions: substrate temperature = 400 °C, fluence = 1.7 J/cm^2, laser spot = 1.9 mm^2. The RMS roughness is 0.3 nm. In Fig. 3.5b the AFM of a 16 nm thick film of VO_2 (identified as sample B) is shown, grown at the same deposition conditions. The thickness for both the samples is determined through the fitting of the XRD spectra. The RMS for sample B is comparable to the one for sample A but now a surface buckling is observed. Micrograins of different areas and with sides parallel to the unit cell axes of TiO_2 form in the thin film. The effect is not due to the substrate since annealing TiO_2 (001) substrates under the conditions used for the VO_2 growth didn't lead to such modifications (similar but smaller structures were found for TiO_2 (001) substrates annealed at 1050 K[102]). The buckling is observable in the AFM image for the presence of straight ridges 0.4 nm high. The pattern appeared evident after etching the VO_2 film in a NaOH solution for 30 seconds, since the chemical etching takes place preferentially along defects. In Fig 3.5c and Fig. 3.5d the comparison between the XRD spectra and the characteristics of the resistance versus temperature $R(T)$ for the two thin films are showed. The resistance is measured with the PPMS using a 4-wire configuration. The XRD spectra show the difference in thickness between the two samples. The MIT for sample B is much less sharp than for sample A and spreads over until the bulk T_c of 340 K (the comparison between the parameters is shown in Table 4).

The “microbeams” have been already observed and deeply characterized in the recent work of Li *et al*. [145,146] for thin films of VO_2 on TiO_2 (001) with a thickness above 30 nm. Their origin is attributed to different strain relaxations taking place during growth that create buckling or even cracks along the main crystal directions. VO_2 thin films on TiO_2 (001) substrates, in fact, are subjected to in-plane tensile strain. According to the degree of relaxation, different microbeams have different transition temperatures tending towards the bulk T_c that represents the case of total relaxation. In particular, it was found that the material forming the buckling is completely relaxed and that narrower beams have a higher level of relaxation, hence higher local T_c. Furthermore, a gradual strain relaxation is present from the edge of the microbeam towards the inside. Despite the partial strain relaxation, these samples show a large inhomogeneity.

This description would explain why sample B shows a broader MIT since areas with different transition temperatures constitute the thin film. The transport properties of thick films of VO_2 on TiO_2 (001) confirm the observation of an inhomogeneous strained film. In addition, the samples shown in this work suggest that the effect depends on the film thickness and that the critical thickness is about 10 nm. Some of the samples grown showed intermediate properties between sample A and B. In the inset of Fig. 3.5d, the MIT of a 11 nm thick VO_2 film is shown. This sample shows no buckling at the surface; this fact suggests that the elastic energy due to strain is not enough to provoke a relaxation of the film. Nonetheless the film shows inhomogeneity only for a part of the temperature range, namely of the structural transition. In order to understand this behavior, one needs to notice that going from monoclinic to rutile phase (from low to high temperature), the thin film is subjected to additional in-plane tensile strain.[86] For thicknesses around 10 nm, then, the film shows uniformity because of the substrate influence until a further strain is applied, which makes the film heterogeneous but does not allow for complete relaxation.

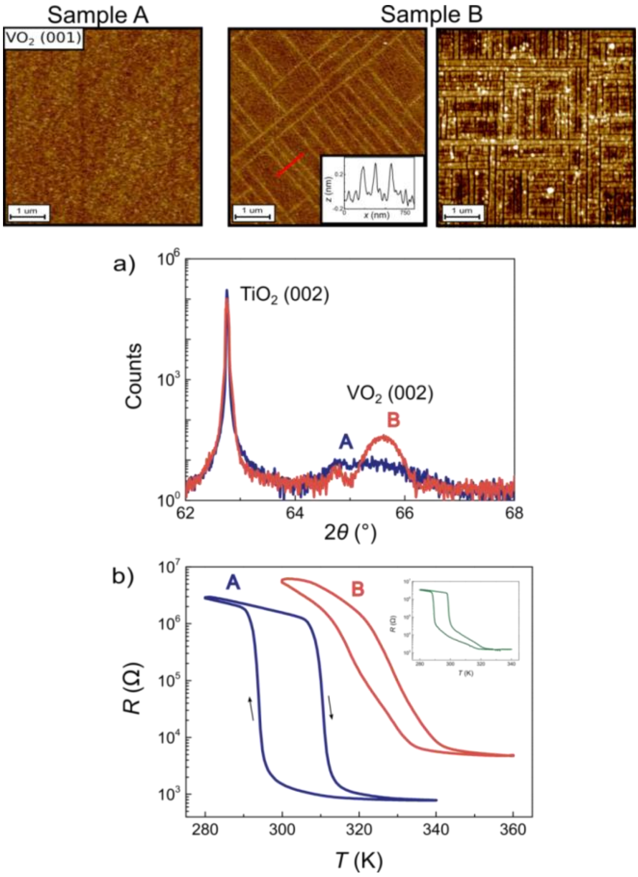

Figure 3.5 Characterization of thin films of VO_2 (001) grown on TiO_2 (001). At the top: AFM topography of sample A (z = 3 nm) and of sample B (z = 7 nm) as grown and after etching it for 30 sec in NaOH; the inset shows the height z along the red line. a) 2θ-ω XRD scan for samples A and B. b) Measurement of the resistance versus temperature for samples A and B performed with the PPMS in 4-wire configuration. In the inset, the R(T) characteristic of a different film with a thickness of 11 nm is shown.

	RMS (nm)	***d* (Å)**	**$\Delta R/R$**	**T_c (K)**	**ΔT (K)**	**dT (K)**
Sample A	0.28	2.857	$2.9*10^3$	303	16.9	3.1
Sample B	0.25	2.849	$1.1 *10^3$	325	8.6	20

Table 4 Main parameters obtained by the analysis of the measurements performed above. The RMS roughness is extracted by the AFM images; the out-of-plane lattice parameter d from the XRD spectra and the other values from the R(T) characteristics for the samples A and B.

VO_2 thin films on (111) $LaAlO_3$

As anticipated in paragraph 3.2.3, $LaAlO_3$ can be represented like a sequence of Al^{3+} and $(LaO_3)^{3-}$ planes along the [111] direction. The LaO_3 plane can be considered as a pseudo-close-packed oxygen plane since the oxygen atoms are separated just by few lanthanum atoms (Fig. 3.6b). On such a surface it is possible to grow VO_2 if one considers that the vanadium atoms will adjust on the oxygen atoms.[125] On the substrate surface, in particular, there are three equivalent close-packed directions separated by 60°. For this reason, 3D VO_2 grains form, aligned along these directions.

VO_2 thin films were grown via PLD on a (111) $LaAlO_3$ substrate at 10^{-2} mbar oxygen atmosphere. The laser spot size and the substrate temperature were varied in order to study the dependence of the film properties on deposition rate and kinetic energy of the species on the substrate surface. A sintered V_2O_5 target was ablated using a pulse frequency of 2 Hz and a laser fluence of 1.2 J/cm^2. Figure 3.6a shows the AFM topography image of a 30 nm thick VO_2 film. Vanadium atoms bond with the oxygen atoms forming the three pseudo-close-packed directions separated by 60° on the (111) surface of $LaAlO_3$ (Fig. 3.6b).[125] The cross-section profile shows that the grains have a height between 25 nm and 30 nm (Fig. 3.6c). The cross-section SEM image shows the rod-like shape of the grains (Fig. 3.6d). The geometry is due to strain relaxation in one of the in-plane directions taking place above a certain grain dimension. This critical grain size depends on the deposition conditions, as it will be shown further. Very little amount of material is present between the grains. The amount depends on the growth conditions used. The *in-situ* RHEED pattern showed an abrupt transition from 2D to 3D growth after 1 nm of deposited material. Using the AFM, one can have information about the surface area between the grains. In particular, Fig. 3.7 shows the phase signal recorded with the AFM in tapping mode. The phase shift in the oscillation of the cantilever gives information about adhesion and viscoelastic properties of the material under the tip, beyond topographic information. In the image shown here, one can observe a rather flat and uniform area between the grains apart from smaller islands of material present at the sides of the grain, which are the favorable spots for nucleation. We performed also cross-section STEM on a thin film of VO_2 on (111) $LaAlO_3$; the result is shown in Fig. 3.8. The grains are randomly distributed on the surface and have different shapes according to their direction respect to the cut direction. The height of the grains is about 30 nm. In the area between the grains, a flat surface is observed; the minor reconstructions present are most likely due to the surface polarity. Local EDX performed at the interface between substrate and grain as well as at the surface area between grains shows intermixing between La, Al and V atoms.

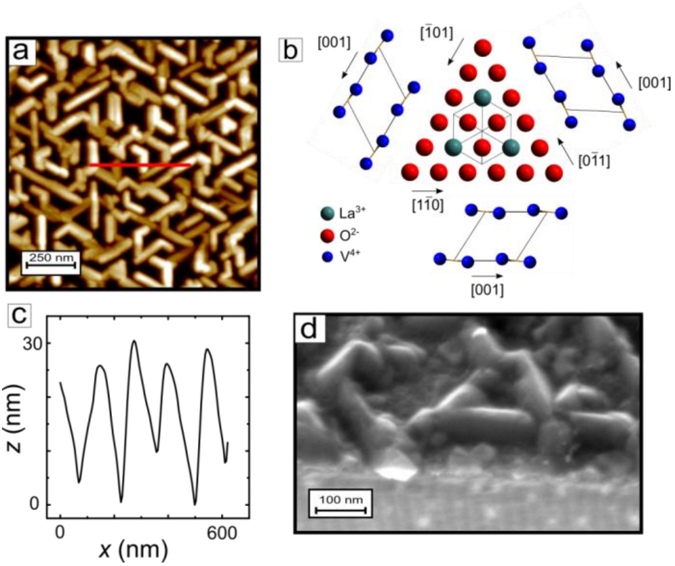

Figure 3.6 (a) Top-view AFM image (z = 20 nm) of a 30 nm thick VO_2 film grown on $LaAlO_3$ (111). The sketch in (b) shows the three possible alignment of monoclinic VO_2 (010) unit cell along the oxygen close-packed directions on the cubic $LaAlO_3$ (111) plane. (c) Measurement of the height z of the grains crossed by the red line in the AFM image. (d) Cross-section SEM image of the thin film.

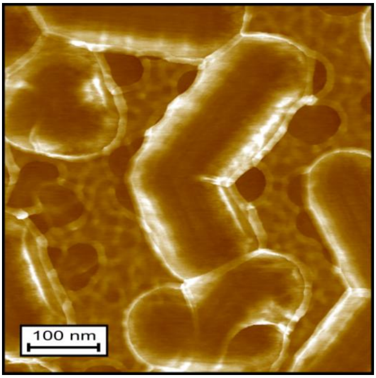

Figure 3.7 Phase signal of an AFM topography (z = 50°) in tapping mode of a grain of VO_2 on $LaAlO_3$ (111).The area between the grains consists of smaller islands at the sides of the grain and a flat surface elsewhere.

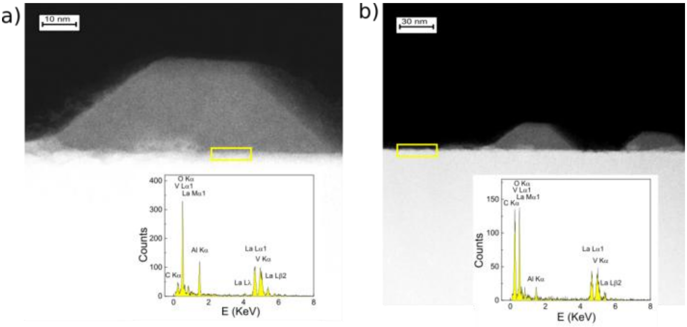

Figure 3.8 Cross-section dark field STEM images of a thin film of VO_2 on $LaAlO_3$ (111). The insets show the EDX spectra measured in the areas marked with the yellow rectangles. Both at the interface between grain and substrate (a) and in the area between grains (b), cation intermixing is observed.

This peculiar grain structure can be a useful tool to characterize the dependence of the PLD growth of VO_2 on the deposition parameters: the grains' formation depends critically on the substrate temperature and the laser spot size on the target. Top-view AFM images of VO_2 thin films on $LaAlO_3$ (111) substrates grown under different conditions are shown in Fig. 3.9. From *a* to *d* the substrate temperature is varied from 400 °C to 500 °C. From *d* to *f* the laser spot size hitting the target is varied from 4.2 mm^2 to 2.2 mm^2 by changing the mask before the fixed focusing lens in the laser beam path. A change of 25 °C of the substrate temperature drastically modifies the thin film morphology from irregular islands to aligned grains. A further increase in the temperature induces coalescence among grains leading to the formation of grains with comparable size but reduced density and slightly increased height (as it is evident from the common z scale in false colors). Increasing the laser spot size, the material ablated reaching the substrate increases. In our samples, a first increase in grain dimension is observed. Between the bigger grains, not-oriented islands are deposited. However, for larger spot sizes, smaller grains form with an extremely reduced amount of inter-grain islands. Counterintuitively, by increasing the deposition rate, one induces, in optimized conditions, a reduction of grain size.

Following the capillarity theory of heterogeneous nucleation of a condensed film on a substrate[147] one can describe the system macroscopically, looking for the state representing thermodynamic equilibrium; using this description, the nucleation results from the balance between the tendency to minimize the free energy of the supersaturated vapor, forming chemical bonds, and that to minimize the surface energies of the substrate, the film and their interface. Minimizing the critical free energy barrier and the critical grain size necessary to overcome for nucleation to be stable with respect to substrate temperature and deposition rate, one obtains that: an increase in deposition rate results in smaller islands; at higher substrate temperature, the critical grain size increases and the grain structure is expected to persist to a higher average coverage making the formation of a continuous film more difficult. For the range of parameters considered in this work we don´t observe an increase in lateral grain dimensions with temperature but the 3D structure results more defined at the highest temperature. At this temperature we do observe a reduction in grain size with increasing the deposition rate.

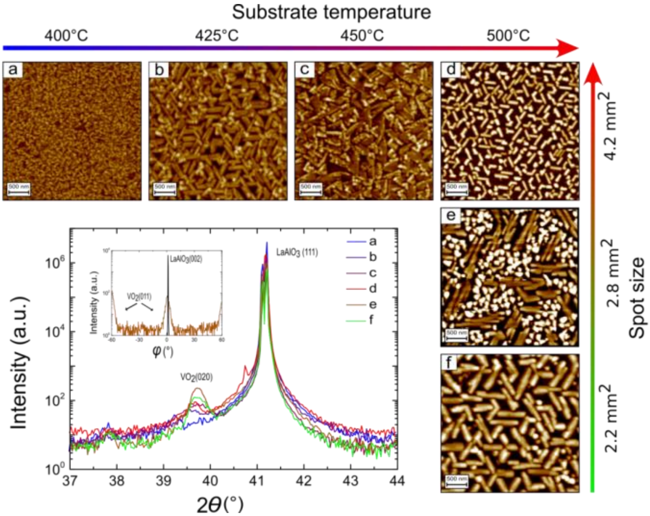

Figure 3.9 Top-view AFM images of VO_2 thin films grown via PLD at different substrate temperatures (a-d) and different laser spot size (d-f). The z scale in false color is 40 nm. The graph shows the 2θ-ω XRD scans for the samples relative to the AFM images. The inset shows the φ scan for two asymmetric directions of the substrate and the thin film relative to sample e.

The *2θ-ω* scans for the samples in the AFM images are shown in Fig. 3.9. The (020) VO_2 peak has a higher intensity for the samples with bigger grains whereas it is not visible for sample *a*. A *φ* scan of the asymmetric (011) reflection of VO_2 and of the (002) reflection of $LaAlO_3$ has been performed in the reduced range [-60°; 60°] for all the samples in order to check the in-plane grain directionality. The data show a six-fold symmetry indicating an alignment of the grains with the three equivalent substrate directions. Also in this case, a higher intensity is observed for the bigger grains.

Despite the higher fraction of crystalline and aligned material, the samples with bigger grains show insulating behavior in the measurement of the resistance *R* versus temperature *T*. As shown by Fig. 3.10, the only samples showing a MIT are samples *b* and *c*. This could be due to the lower grain density of the other samples which do not allow for electrical transport through percolation. The MIT can be characterized by the amplitude $\Delta R/R$ and the width ΔT already defined in ref. 132 and by the FWHM of d(log*R*)/d*T*. The MIT for sample *c* shows $\Delta R/R \approx 10^2$, $\Delta T \approx 10$ °C, FWHM ≈ 10 °C. The transition amplitude $\Delta R/R$ is one order of magnitude smaller compared to other examples found for PLD grown thin films of VO_2 on other substrates.[122,125,124] Nonetheless, using the growth control that we reached with the present study I was able to grow a sample with enough large and dense grains to show a MIT with improved characteristics. This sample is named *e´* since it has been grown with the same temperature and spot size as sample *e* but with higher laser fluence (fluence = 1.8 J/cm^2). Figure 5 shows the AFM topography of this sample and its *R*(*T*) in comparison with the one of sample *b*. The MIT characteristics for sample *e´* are $\Delta R/R \approx 10^3$, $\Delta T \approx 13$ °C, FWHM ≈ 4.5 °C. Grain size effects on the MIT in VO_2 have been analyzed for thin films grown on Al_2O_3, Si, SiO_2 and TiO_2 substrates.[148–152] In particular, the relation of the grain size to the width ΔT and FWHM of the transition can be of great interest for optical data storage application.[153] The models proposed so far to explain a heterogeneous martensitic transition predict an inverse proportionality between ΔT and grain size.[149,154] In those models, the free energies related to the metallic and semiconducting phase, the specific energy of the elastic strain accompanying the transition and the interface energy between the two phases are considered. The most likely nucleation site considered is the grain surface. Experimentally, however, the effect is mainly related to the presence of extrinsic defects in the grains that boost the transition acting as nucleation sites and that are not considered in the models. For the samples analyzed in this work, larger grains correspond to a larger width ΔT and a larger amplitude $\Delta R/R$. In particular, the value of the resistance in the metallic phase is lower. This could be due to a lower concentration of defects and to better crystallinity as found from the comparison between the XRD spectra.

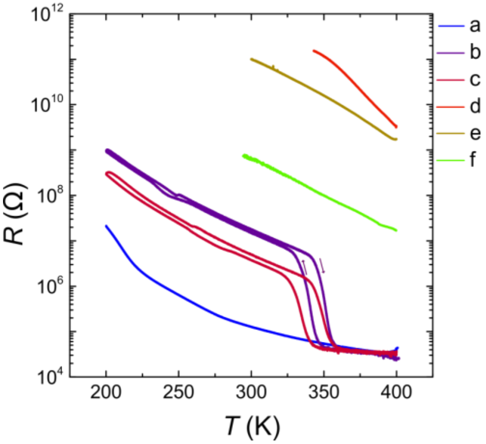

Figure 3.10 Results of the measurement of the resistance versus temperature for the samples introduced in Fig. 3.9, performed in 4-wire configuration inside a PPMS (rate = 1 K/min).

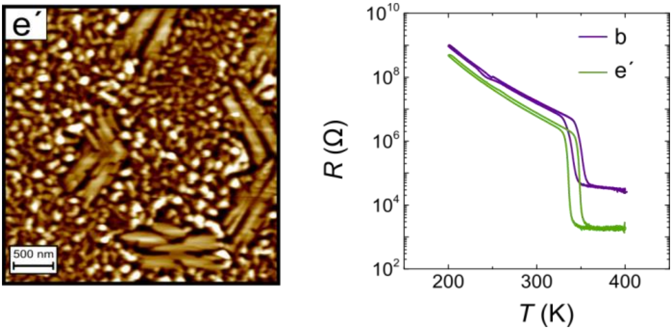

Figure 3.11 Left: AFM topography (z = 40 nm) of the sample e´. Right: Comparison between the measurements of the resistance versus temperature for samples b and e´.

We still need to find an answer to the question about the existence of a percolation threshold preventing the observation via global transport measurement of the MIT in a part of the samples consisting of aligned grains. Therefore we performed ellipsometry measurements on the samples so to determine the value of the complex dielectric function with temperature. The result is shown in Fig. 3.12. Figure 3.12a shows the real part of the dielectric function ε_1 and the real part of the optical conductivity σ_1 for sample *b* in the insulating monoclinic phase (T = 300 K) and conducting rutile phase (T = 370 K). The behavior is similar to the one found for VO_2 grown on $(\bar{1}012)$ Al_2O_3[155] with the peaks at the main optical transitions for VO_2 in the insulating phase at 1.4 eV and 3.5 eV. Fixing the energy at 1.25 eV, we measured the same quantities with varying temperature in a rate of ≈ 0.6 K/min for sample *b* showing the transport MIT and for sample *e* not showing the transport MIT. They both show a transition in the optical properties at about the same temperature as the transport MIT. The optical MIT was also found for the other samples that don´t show a transport MIT. The amplitude of the optical transition is directly proportional to the grain dimensions, confirming a higher level of uniformity and crystallinity for the samples with bigger grains.

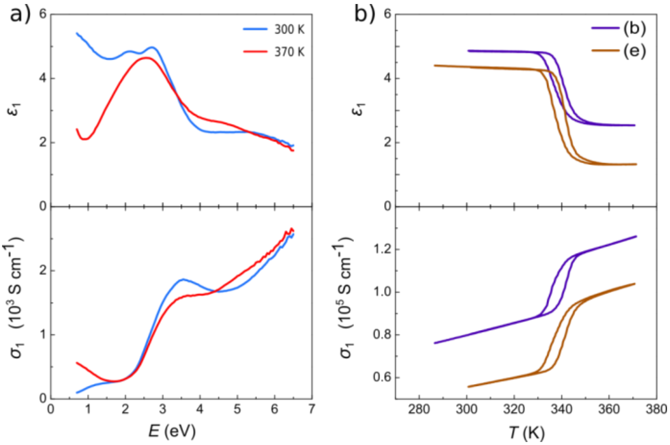

Figure 3.12 Results of the measurement of the real part of the dielectric function ε_1 and of the optical conductivity σ_1: (a) versus energy for sample b in the insulating (T = 300 K) and conducting (T = 370 K) phase; (b) versus temperature for samples b and e. The two quantities were determined from the ellipsometric parameters $\Psi(w)$ and $\Delta(w)$; the effect of the substrate has been subtracted.

3.4 PLD growth of oxide electrodes

A transition metal oxide differentiates from a semiconductor mostly for the strong coupling between charge, spin and orbital degrees of freedom present in the material which enriches the possible behaviors that this class of materials can show. VO_2 with its electronic and structural phase transition belongs to this class. In the previous paragraphs we could observe the effects of the large sensitivity of this material to the structural modifications. The growth of a transition metal oxide in form of a thin film, then, gives the possibility to tune its properties by doping, thickness and strain control. Using PLD, one can have control on the stoichiometry and the thickness of these materials in a reproducible way and can grow different layered materials consecutively in order to combine their properties. The phenomena that are potentially observable make the growth of transition metal oxide thin films a particular hot topic. However, because of their structural complexity and their sensitivity to variations in the deposition conditions, the growth of crystalline metal oxides may be challenging. In the following, I will discuss the PLD growth of different transition metal oxides with rutile (001) and perovskite (111) structure. They show metallic behavior across the thin film or at the interface between the thin film and the substrate. The comparison between their deposition conditions and their transport properties is an important tool to decide how to combine them into an all-oxide tunnel junction. This kind of heterostructures are not commonly found in literature for the difficulty related to their production but can represent an exciting system to characterize the behavior of these complex oxides.

3.4.1 RuO_2

RuO_2 has tetragonal structure and exhibits many interesting properties such as low room-temperature resistivity, very low oxygen ionic conductivity, good thermal stability and high chemical corrosion resistance. For these reasons it has been used for many applications such as in very large scale integrated circuits,[156] as a diffusion barrier between Al and Si[157,158] and as a buffer layer for high temperature superconducting $YBa_2Cu_3O_{7-x}$ films.[159] The in-plane misfit with TiO_2 is 2%. RuO_2 is a good candidate to be the bottom electrode for a rutile oxide heterostructure. However, even if RuO_2 is the most stable of Ru oxides, it is known for its high volatility in an oxidized environment. This makes the growth of very flat RuO_2 thin films particularly challenging. From previous studies we know that RuO_2 films are polycrystalline for substrate temperatures lower than 400 °C and higher than 700 °C and elemental Ru appears for temperatures higher than 800 °C.[160] Using a RuO_2 target by Toshima, I grew via PLD thin films of RuO_2 on (001) TiO_2 substrates changing the growth conditions in the following ranges: substrate temperature = [500 °C, 700 °C]; oxygen pressure = [10^{-3} mbar,

$2 \cdot 10^{-2}$ mbar]; laser fluence = [1 J/cm^2, 3 J/cm^2]; laser spot on the target = [1.9 mm^2, 7.5 mm^2]. As already anticipated, one of the main issues related to the growth of RuO_2 is its high volatility. The window of growth conditions in which the material sticks on the substrate surface and, at the same time, disposes in a flat and conducting film, is particularly restricted since these processes occur for different condition ranges. In particular, in order to have films as flat as possible one should grow at high substrate temperatures, i.e. $T_s > 600$ °C, and with a low deposition rate. The deposition rate depends on oxygen pressure, laser fluence and laser spot on the target. For RuO_2, however, an oxygen pressure above 10^{-3} mbar causes a non-uniform material growth because of re-evaporation. Figure 3.13a shows the image obtained with an optical microscope of a sample grown at 10^{-2} mbar and presenting a large non-uniformity. The material is concentrated in the center of the sample where the species in the plume hit the substrate with a larger energy. Nonetheless we were able to find conditions at which a better uniformity is obtained. Figure 3.13b-d shows the characterization of a RuO_2 thin film grown under the following conditions: substrate temperature = 600 °C; oxygen pressure = 10^{-3} mbar; laser fluence = 3 J/cm^2; laser spot on the target = 1.9 mm^2; repetition rate = 4 Hz; rate = 0.08 Å/shot. The optical microscope image and the AFM topography show a homogeneous surface. The XRD spectrum shows a crystalline thin film. The thickness defined through the reflectivity measurement shown in the inset is 50 nm. The RMS calculated from the AFM image is 1.7 nm. This value is affected by the presence of the big particles visible both in the AFM topography and in the image taken with the optical microscope. We were not able to avoid the deposition of these particles that are most likely coming from the segregation of macro-particles during the target ablation. The target of RuO_2, in fact, is particularly porous and this prevents us to obtain thin films with enough low roughness to be used as bottom electrodes in a tunnel junction.

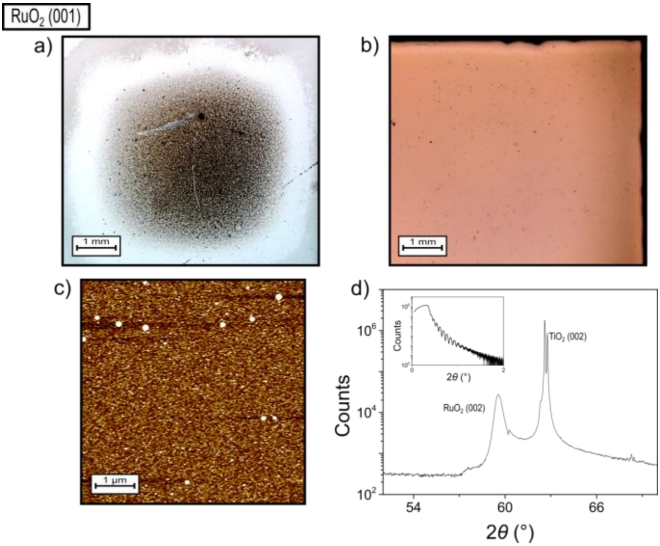

Figure 3.13 a) Photograph of a RuO_2 thin film grown in an oxygen pressure of 10^{-2} mbar. b) Photograph of a RuO_2 thin film grown at 10^{-3} mbar (deposition conditions in the text). The RMS roughness for this sample is 2.3 nm and the bigger particles have a height of 40 nm (the z scale in the AFM picture (c) is 10 nm). d) 2θ-ω XRD spectrum for the sample in (b). The double peak relative to the substrate is due to the presence of $K\alpha 1$ and $K\alpha 2$ in the incident beam. In the inset the reflectivity measurement is shown.

3.4.2 PLD growth of (111)-oriented perovskite oxide electrodes

The optical, electronic and magnetic properties of perovskite oxides depend closely on the oxygen octahedron modifications from the cubic structure. These effects are amplified at the interface between two different perovskites because of a possible discontinuity that the system has to face. For (111)-oriented interfaces, the structural and electronic coupling can be expected to be even stronger than for (001)-oriented interfaces since the oxygen octahedra at the interface share three corners instead of one. Furthermore, as already described in paragraph 3.2.3, (111) perovskites are polar. At the interface between two of these materials a polar discontinuity can take place, which may lead to new electronic and topological interfaces. Examples of the new phenomena that were observed in this kind of interfaces are an exchange bias in (111) $LaNiO_3$/$LaMnO_3$ superlattices[161] and a MIT in $La_{0.5}Ca_{0.5}MnO_3$ on (111) $SrTiO_3$[162] non-existent in similar (001) systems.

The surfaces of the thin films grown on a polar substrate like (111) $SrTiO_3$, however, are generally disordered.[161–167] This is mainly due to the surface polarity. The presence of a dipole perpendicular to the surface, in fact, causes the surface energy to diverge.[168] To prevent this, the material undergoes varied spontaneous reconstructions: change in the surface stoichiometry; redistribution of the electrons in the surface region; adsorption of atoms or molecules; faceting.[169] These mechanisms allow for a large number of surface reorganizations that depend on the particular process used to treat the substrate. So, even if single terminated (111) surfaces can be achieved, they will always reconstruct according to the ambient conditions preventing coherent growth of the first monolayers of the film material. Furthermore, if a polar material is deposited on top of the substrate, a polar discontinuity can occur at the interface, leading to electronic or structural modifications, such as intermixing of atoms between the two interfacial layers and electron transport at the interface if there are multivalent atoms.[170] However, if the material at the interface is sufficiently conducting at deposition conditions, the free charges can screen the electric displacement field and prevent reconstructions.[171]

In the following paragraphs I will describe the PLD growth of three different oxides on a (111)-oriented $SrTiO_3$ substrate. The goal is to grow an oxide bottom electrode for tunnel junctions. Interestingly we will notice that the growth process has some common traits for all these polar materials but the transport properties of the thin films can be very different.

$SrRuO_3$

Strontium ruthenate ($SrRuO_3$) is a perovskite compound with orthorhombic symmetry at room temperature. The RuO_6 octahedron defines a distorted pseudocubic perovskite cell with lattice parameter a = 3.93 Å (see Table 2). Around 550 °C the orthorhombic structure transforms into a tetragonal structure. The valence electrons reside in the Ru(4d) orbitals allowing for correlation effects in the transport properties of the material. $SrRuO_3$ exhibits bad metal behavior at high temperatures and Fermi-liquid behavior at low temperatures. It is paramagnetic at room temperature and ferromagnetic below the Curie temperature of about 150 K. This transition is observed also as a sharp change in resistivity around the Curie temperature. Because of its low resistivity at room temperature, the material has been extensively used as a thin film electrode for oxide heterostructures with good lattice-matched materials.[172–174] The thin film growth of $SrRuO_3$ has been performed via different techniques and it has been well characterized, becoming a model system for studying the relation between its structure and its magnetic and electronic properties. For a detailed review see reference 120. Regarding, in particular, the PLD growth of $SrRuO_3$ on (001) $SrTiO_3$, it was found that the conductivity increases with increasing deposition temperatures and oxygen pressure because of increased crystallinity and reduced number of defects such as vacancies and antiphase domain boundaries.[175–180] In optimized conditions (substrate temperature = 600 °C, oxygen pressure = 0.1 Torr), the growth evolves from 2D layer-by-layer to step-flow mode after the first few RHEED oscillations.[181]

The growth of $SrRuO_3$ thin films on (111)-oriented $SrTiO_3$ proceeds in a different way as compared to the growth on (001)-oriented substrates because of the polarity of the substrate and of the film. Because of the difficulty of the growth on (111)-oriented substrates, not many attempts are found in literature for the growth of $SrRuO_3$ on $SrTiO_3$ (111).[182–186] As observed by Chang *et al.*[187], under optimized growth conditions, a damping of the RHEED oscillations takes place after 3 unit cells because of the roughening of the surface due to the substrate/film polarity. If the adatom mobility is large enough to overcome the roughening, the damping is controlled and the layer-by-layer growth lasts for a longer number of oscillations. If, on the contrary, the mobility is small, the growth becomes 3D immediately after few oscillations; the 3D growth persists up to a certain thickness of the $SrRuO_3$ film that represents the critical thickness for the thin film to be conducting and screen the substrate polarity.[188] From this point on, the layer-by-layer growth is recovered and can last for a large number of oscillations. The two processes can take place exclusively according to the deposition conditions used.

I grew thin films of $SrRuO_3$ on (111) $SrTiO_3$ using a sintered $SrRuO_3$ target obtained from Lesker and I varied the deposition conditions in the following ranges to find the optimal conditions: substrate temperature = [600 °C, 800°C]; laser fluence = [1 J/cm^2, 2 J/cm^2]; laser spot on the target = [1.1 mm^2, 2.8 mm^2]. The oxygen pressure was kept at 10^{-1} mbar. Figure 3.14a shows the AFM topography of a 10 nm thick film grown at substrate temperature = 650 °C, fluence = 1.2 J/cm^2, laser spot = 2.2 mm^2, a laser frequency of 2 Hz and a rate of 0.038 Å/shot. The RMS roughness for this sample is 0.2 nm and the terrace structure of the substrate is still partially visible. The dips present on the terraces are at most two unit cells deep. Figure 3.14b shows the RHEED pattern before and after growth. The substrate pattern is taken at 10^{-4} mbar and shows clearly the specular and the lateral spots together with the Kikuchi lines. The film pattern is taken at 10^{-1} mbar. At this pressure, the scattering with the gas particles affects the electron trajectories. However, the specular and the lateral spots are clearly visible and are still disposed along a semicircle, indicating a 2D surface. The lateral spots show more pronounced streaks compared to the substrate spots. Furthermore intermediate streaks are visible. This is most likely due to the non-uniformity of the terraces. The presence of additional steps inside a terrace with a different periodicity increases the number and width of the reciprocal rods relative to a 2D surface. The intensity of the specular spot, signed by the red circle in Fig. 3.14, has been measured during the growth. The result is shown in Fig. 3.14c. One of the processes described by Chang *et al.* is observable here. A fast roughening of the surface is observed during the first 4 unit cells deposited (transition from 2D to 3D growth in the graph) and then a layer-by-layer 2D growth is obtained for the next 43 oscillations.

The reproducibility of the film quality was one of the issues faced during the optimization of the $SrRuO_3$ growth. The film topography depended on small changes in the growth conditions. In the case of $SrRuO_3$, the target was not polished before every growth since every polishing required a new optimization of the deposition conditions. This could be due to non-uniformity of the target. Additionally, the porosity of the target may favor the deposition of particulates on the substrate surface. The quality of the substrate surface also affects the film growth. For example, the presence of structural defects on the surface substrate may prevent the formation of a very flat thin film. Figure 3.14d shows the AFM topography of a 10 nm thick $SrRuO_3$ thin film grown in a different PLD chamber but at conditions similar to the one used for the sample in Fig. 3.14a. The film followed a layer-by-layer growth mode, as observed by the RHEED oscillations (not shown) and as it is evident from the AFM image where the terraces can be observed. The layers, however, develop around point defects and prevent the film to be flat.

I grew films with three different thicknesses in order to find the right balance between flat surface and low resistivity. The transport properties of $SrRuO_3$ depend on the film thickness. In particular two critical thicknesses have been found for the growth of $SrRuO_3$ on (001) $SrTiO_3$: a metal-insulator transition takes place around 2-3 unit cells ($\approx$ 1 nm considering the lattice parameter along (001) direction) while the Ru 4d-derived states around the Fermi level saturates at about 7-8 unit cells ($\approx$ 3 nm).[188] For (111)-oriented $SrRuO_3$ the situation is made slightly more complex because of the reconstruction induced by the polarization. Figure 3.14e shows the measurement of the sheet resistance R_s against the temperature T for three different thin film thicknesses. With reducing thickness, R_s increases. At smaller thickness the kink at 105 K is less visible and an upturn at low temperatures is present which probably is caused by charge localization.

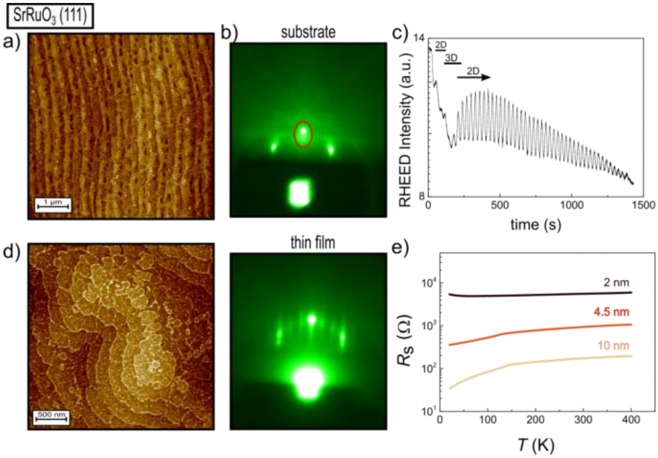

Figure 3.14 a) AFM topography (z = 2 nm) of a 10 nm thick (111) $SrRuO_3$ film on (111) $SrTiO_3$. b) RHEED pattern of the substrate taken at 10^{-4} mbar and of the film taken at 10^{-1} mbar after the growth. c) RHEED intensity of the specular spot (signed in red) during the growth. The sequence 2D-3D-2D in the growth process is indicated. d) AFM topography (z = 2 nm) of a $SrRuO_3$ thin film growing with layer-by-layer mode around structural defects of the substrate surface. e) Sheet resistance R_s versus temperature of $SrRuO_3$ thin films with different thicknesses.

$La_{0.7}Sr_{0.3}MnO_3$

Strontium-doped lanthanum manganite ($La_{0.7}Sr_{0.3}MnO_3$) has a slightly distorted perovskite structure (rhombohedral $R\bar{3}c$ structure) that can be represented as a pseudo-cubic structure with a lattice parameter $a \sim 3.873$ Å and an angle $\sim 90.26°$. Its electronic and magnetic properties are very different from the ones of the parent compound $LaMnO_3$. The hole-doping provokes a change in the oxidation state of a part of the manganese ions from Mn^{3+} to Mn^{4+}. The e_g level of the *3d* Mn orbitals are occupied with one electron in the case of Mn^{3+} and they are empty in the case of Mn^{4+}. The correlation among the electrons in the e_g level causes that $LaMnO_3$ is an antiferromagnetic insulator with dominant Jahn-Teller effects, while $La_{0.7}Sr_{0.3}MnO_3$ is a ferromagnetic half metal due to double-exchange interaction involving the Mn^{3+}-O-Mn^{4+} chain with a Curie temperature T_c ~ 350 K[189] (the largest among manganites). Magnetic fields reduce the resistivity of $La_{0.7}Sr_{0.3}MnO_3$ markedly, particularly around T_c (where the spin polarization can reach 100%), giving rise to colossal magneto-resistance. These properties, together with the half-metallicity, have favored the use of $La_{0.7}Sr_{0.3}MnO_3$ for magnetic tunnel junctions[190,191], Schottky devices[192,193] and magnetoelectric devices[194–196].

In this work we investigate the use of (111) oriented $La_{0.7}Sr_{0.3}MnO_3$ as a bottom electrode for oxide heterostructures because of its relatively small room temperature resistivity and its small mismatch with other perovskite oxides. The PLD growth conditions used for the fabrication of thin films of (001) $La_{0.7}Sr_{0.3}MnO_3$ on different substrates affect drastically the film quality and the film properties.[189] Since we are not taking advantage of the magnetic properties of $La_{0.7}Sr_{0.3}MnO_3$, we will focus our attention on the optimization of the film structural and transport properties. We grew thin films of $La_{0.7}Sr_{0.3}MnO_3$ on (111) $SrTiO_3$ substrate via PLD using a sintered target of $La_{0.7}Sr_{0.3}MnO_3$ by Lesker. We varied the deposition conditions in the following ranges in order to find the optimal ones: substrate temperature = [550 °C, 750 °C]; laser fluence = [1.5 J/cm^2, 2 J/cm^2]; oxygen pressure = [0.1 mbar, 0.3 mbar]; the laser spot on the target was 2.2 mm^2 and the repetition rate is 1 Hz. Figure 3.15a shows the AFM topography for a 10 nm thick film grown in the following conditions, chosen as optimal: substrate temperature = 750 °C; laser fluence = 2 J/cm^2; oxygen pressure = 0.1 mbar; rate = 0.074 Å/shot. The calculated RMS roughness is 0.1 nm and the step-and-terrace structure coming from the substrate is still visible. Figure 3.15b shows the RHEED specular spot intensity during the thin film growth. The growth of $La_{0.7}Sr_{0.3}MnO_3$ resembles the growth of $SrRuO_3$ on (111) $SrTiO_3$. After the few initial RHEED oscillations, the growth results 3D until the layer-by-layer growth is recovered with a large reprise of the spot intensity, followed by a damping due to film roughening.

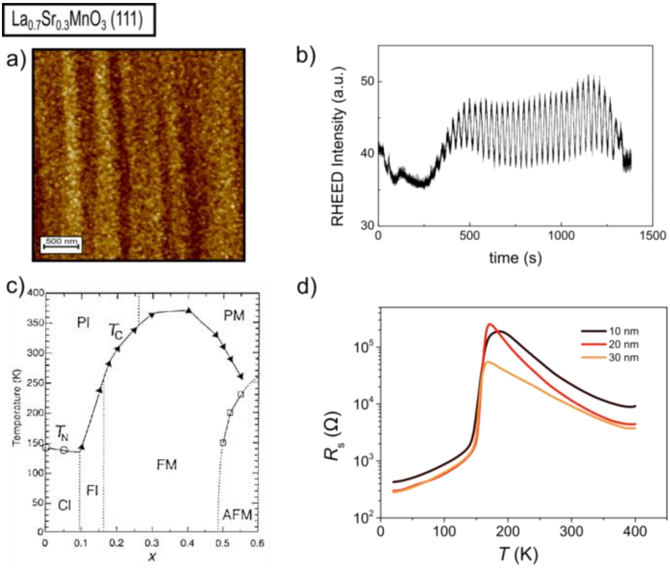

Figure 3.15 (a) AFM topography (z = 1 nm) of a 10 nm $La_{0.7}Sr_{0.3}MnO_3$ thick film grown via PLD at a substrate temperature of 750 °C and oxygen pressure of 0.1 mbar. In (b) the RHEED intensity of the specular spot during growth is shown. The layer-by-layer growth is recovered after the initial 3D growth and goes on for 35 unit cells. (c) Phase diagram of bulk $La_{1-x}Sr_xMnO_3$ after ref. 197. *A MIT with temperature is expected for a certain range of doping values. (d) Sheet resistance measured with Van der Pauw technique for three different thicknesses. The insulator to metal transition persists at least up to 30 nm.*

Hallsteinsen *et al.*[198] have observed the same growth sequence for $La_{0.7}Sr_{0.3}MnO_3$ as Chang *et al.*[199] for $SrRuO_3$. In particular they observed at first an evolution from 2D to 3D growth mode and then again a 2D growth mode for a certain thickness window beyond which the surface becomes rough. This happens for a temperature of 500 °C at which the adatom mobility is relatively low. They concluded that in order to have thicker samples with preserved step-and-terrace structure, not too high substrate temperatures have to be used. In their work, however, they don´t analyze the transport properties of the samples. According to our experience, 10 nm thick films with reduced roughness can be grown already at 550 °C but the roughness decreases if the substrate temperature is increased to 650 °C and 750 °C. The sample grown at 750 °C shows a high level of crystallinity, a lattice parameter comparable to the bulk value and a small resistivity at room temperature compared to the samples grown at lower temperatures.

The phase of the compound $La_{1-x}Sr_xMnO_3$ depends on the doping level x.[200] Figure 3.15c shows the phase diagram for the bulk material. A metal-insulator transition is expected with varying temperature for a particular range of doping levels. The transition temperature equals the Curie temperature and depends on the doping level. The model used to explain this behavior is the Double Exchange model but the contribution of disorder, creating a two-phase system, is considered in some cases to have a correct interpretation of the experimental results.[197] For thin films of $La_{0.7}Sr_{0.3}MnO_3$ the transition temperature depends on the strain to which the film is subjected and it was found that it decreases with decreasing film thickness for thin films along [001] direction.[114] The model suggested by Balevicius *et al.*[202] to explain this finding considers the existence in the film of a more strained phase and of a strain-relaxed phase with magnetic properties closer to the bulk system. The change in the relative ratios of these two phases with film thickness would determine the dependence of the transition temperature on the thickness. The existence of a critical film thickness below which the conducting behavior disappears is attributed to localization effects induced by interface electronic reconstructions, oxygen vacancies and/or A-site cation disorder.[203]

Many different values have been reported for the critical thickness of $La_{0.7}Sr_{0.3}MnO_3$ on (001) $SrTiO_3$, all the values being smaller than 5 nm.[204–206] For $La_{0.7}Sr_{0.3}MnO_3$ grown on (111) $SrTiO_3$ the behavior seems to be slightly different. I measured the sheet resistance of thin films with different thicknesses grown in the same conditions (substrate temperature = 750 °C). The result is shown in Fig. 3.15d. The insulator-to-metal transition takes still place for a 10 nm thick film and persists at least up to a thickness of 30 nm. The Curie temperature T_C is around 165 K and it does not change substantially with film thickness. The only value reported in literature for T_C for a thin film of $La_{0.7}Sr_{0.3}MnO_3$ (111) is 335 K.[207] This value is close to the values reported for $La_{0.7}Sr_{0.3}MnO_3$ (001) so it should not be drastically affected by the different crystal direction. The samples shown in this work, however, have a much lower transition temperature that does not change with film thickness. This indicates that the relaxed film has not the same properties of the bulk $La_{0.7}Sr_{0.3}MnO_3$. A smaller value of the Curie temperature is usually found for manganites with smaller bandwidth. This is the case for manganites with smaller average cation radius for which the Mn-O-Mn angle is smaller than 180° or for $La_{1-x}Sr_xMnO_3$ with doping levels smaller than 0.3.

For the 10 nm thick film, the value of the sheet resistance around room temperature is still relatively low. Considering the overall transport properties $La_{0.7}Sr_{0.3}MnO_3$ can, in principle, be used as bottom electrode for oxide tunnel junctions.

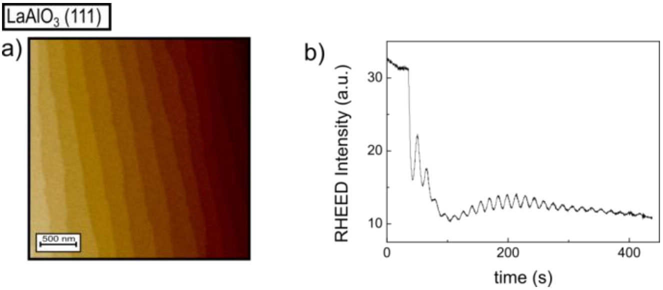

Figure 3.16 (a) AFM topography (z = 5 nm) of a 5 nm $LaAlO_3$ thick film. The step-and-terrace structure resembles the one from the substrate testifying the low surface roughness of the thin film. In (b) the RHEED intensity of the specular spot monitored during the growth is shown. The growth follows the 2D-3D-2D behavior already found for the growth of $SrRuO_3$ and $La_{0.7}Sr_{0.3}MnO_3$ on (111) $SrTiO_3$.

Interface $LaAlO_3$-$SrTiO_3$

In 2004 A. Ohtomo and H.Y. Hwang found that the interface between the two band insulators lanthanum aluminate ($LaAlO_3$) and $SrTiO_3$ (001) is conducting.[208] This discovery boosted the interest around complex oxide heterostructures and, since then, countless literature has been produced about the 2-dimensional electron liquid (2DEL) forming at this interface.[209] The resistivity of the 2DEL is relatively low but it is critically dependent on the thin film growth conditions and on the external potential applied across the material thickness.[210] Keeping this in mind, one could use the 2DEL as a bottom electrode for a tunnel junction. In this case, the thin film of $LaAlO_3$ is the tunnel barrier and only two layers must be grown to build the junction. For the purposes considered in this work, the $LaAlO_3$/$SrTiO_3$ system is (111)-oriented. Herranz *et al*.[211] analyzed the growth of thin films of $LaAlO_3$ on substrate directions different from (001) and for the (111) oriented substrate they found that the interface is also conducting above a certain critical thickness of 9 u.c. but above this thickness the conductance drops quickly to lower values with increasing film thickness. Since the $LaAlO_3$ thin film will work also as tunnel barrier, it has to be thick enough to allow tunneling. The out-of-plane lattice parameter along (111) direction is 0.219 nm. The critical thickness is, then, about 2 nm. However, in order to have an insulating barrier, we will consider first a thin film with a thickness of 5 nm. The optimized deposition conditions for the PLD growth of $LaAlO_3$ are: substrate temperature = 800 °C; oxygen pressure = 10^{-4} mbar; laser fluence = 1 J/cm^2; laser spot on the target = 2 mm^2; repetition rate = 1 Hz. The deposition rate measured from the RHEED oscillations is 0.15 Å/shot. The PLD growth on a substrate of $SrTiO_3$ (111) proceeds in similar fashion as for $SrRuO_3$ and $La_{0.7}Sr_{0.3}MnO_3$ on the same substrate, following the growth mode sequence 2D-3D-2D-3D. This is evident in Fig. 3.15d where the RHEED oscillations of the specular spot intensity during the growth of $LaAlO_3$ are shown. The AFM topography of the 5 nm thick film is shown in Fig. 3.15c. The surface reproduces the substrate surface with the step-and-terrace structure.

Transport properties of (111) oxide electrodes

Figure 3.17 shows the comparison between the sheet resistances of the three (111)-directed oxide electrodes analyzed in this work. Considering the task that the different layers have to perform in the tunnel junction, $LaAlO_3$ has a thickness of 5 nm while $SrRuO_3$ and $La_{0.7}Sr_{0.3}MnO_3$ have a thickness of 10 nm. For $SrRuO_3$ and $La_{0.7}Sr_{0.3}MnO_3$ a Van der Pauw configuration has been used to perform the measurement. For $LaAlO_3$ a 4-wire measurement has been performed using a Corbino ring as device, as described in the next chapter.

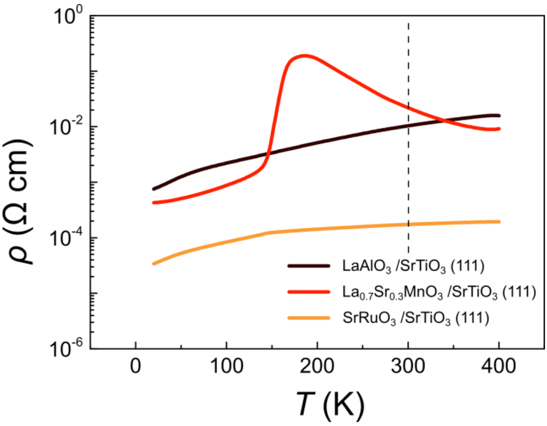

Figure 3.17 Resistivity against temperature for three different thin films grown on (111) $SrTiO_3$. In the case of $LaAlO_3$/$SrTiO_3$ the resistivity at the interface has been measured. $LaAlO_3$ has a thickness of 5 nm while $SrRuO_3$ and $La_{0.7}Sr_{0.3}MnO_3$ have a thickness of 10 nm. The dashed line marks room temperature in order to stress the comparison between the resistivities at the usual working temperature of the devices.

3.4.3 Conducting substrates

Instead of growing a conducting thin film as a bottom electrode, one could think to use directly a conducting substrate. This would remove a step from the growth of the tunnel junction, reducing the problems related to the roughness and non-uniformity of the tunnel barrier. On the other hand, a conducting substrate increases the probability of shorts between the gold contacts evaporated on the sample and the substrate itself in case the insulating thin layer deposited between them presents shorted channels. Differently, a conducting thin film on top of an insulating substrate can be appropriately patterned via etching, reducing, in principle, the probability of shorts. In order to have an oxide substrate enough conducting, doped crystals are in general used. The doping makes the substrate surface more unstable and prone to reconstructions. I will present, in the following, two possible substrates suitable for oxide tunnel junctions.

Nb-TiO_2

I used a 0.05 wt% Nb-doped TiO_2 single crystal as a substrate for the growth of the multilayer VO_2 /TiO_2 /Nb-TiO_2 (001). The substrate was cleaned in ultrasonic bath of acetone followed by one of isopropanol. The substrates are opaque and black, unlike the transparent non-doped TiO_2, and show a RMS roughness of 0.1 nm from the AFM topography (Fig. 3.18a). The resistivity of the single crystal is shown in Fig. 3.19 together with the resistivity of a substrate of Nb-doped $SrTiO_3$ (111) with a higher doping concentration (described below). To build the heterostructure, I first grew a 6 nm thick TiO_2 film at the following conditions: substrate temperature = 700 °C; oxygen pressure = 3 mbar; laser fluence = 1 J/cm^2; laser spot = 2.8 mm^2. For this step a sintered target of TiO_2 by Surface Net was used. The measured growth rate was 0.02 Å/shot. The second step was the growth of 18 nm thick VO_2 film at the following conditions: substrate temperature = 350 °C; oxygen pressure = 10^{-2} mbar; laser fluence = 1.1 J/cm^2; laser spot = 1.9 mm^2. The AFM image of the thin film of VO_2 shows a flat surface with the geometric microbeams found already for the growth of VO_2 on TiO_2 with similar thickness. Additionally, large islands with the shape of an hemisphere of different diameters and heights are present on the surface. An example is shown in Fig. 3.18b. The islands were not found for the bare substrate and after the growth of TiO_2 on Nb-TiO_2. We think that the islands are due to segregation of niobium to the surface. This is more likely at low oxygen pressures[212,213] and this is the reason why we don't observe them after the growth of TiO_2 performed at higher pressure. Following the method described in chapter 4, I built a device that allows to measure the resistance of the TiO_2 barrier in cross-section. The measurement showed a reduced resistance across the TiO_2 barrier compared to the examples found in literature for even thinner TiO_2 thin films grown on different substrates.[214] This is due, most likely, to the presence of shorts caused by the Nb segregation.

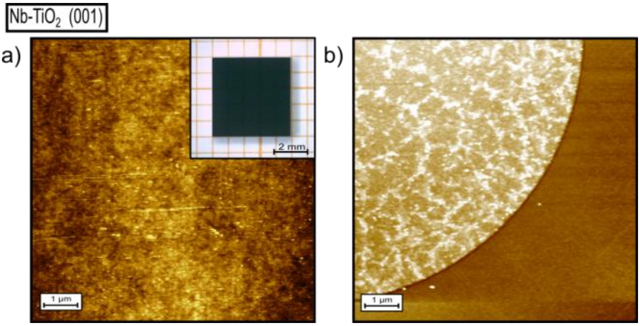

Figure 3.18 AFM topography of a Nb-doped TiO_2 (001) substrate in (a) (z = 1 nm) and of the surface of the multilayer VO_2 /TiO_2 /Nb-TiO_2 in (b) (z = 6 nm). The circular rougher area in (b) is a quarter of an hemispherical island with a height of at least 4 nm. In the flat area between the islands, the microbeams due to the film strain relaxation are present (not observable for the scale used in this image).

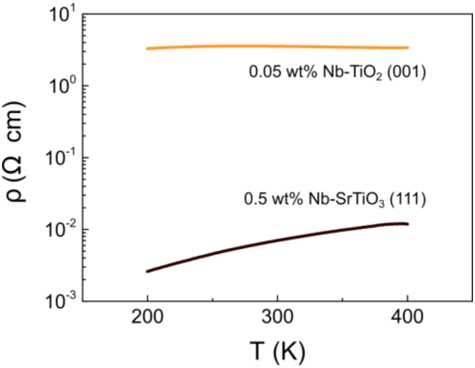

Figure 3.19 Resistivity versus temperature for the conducting substrates used in this work. The measurement was performed using the Van der Pauw technique.

Nb-$SrTiO_3$

One possibility to dope $SrTiO_3$ single crystals is to substitute Nb^{5+} for Ti^{4+}. Nb-$SrTiO_3$ shows a two-band superconductivity around 0.3 K[109,111] and it has been used to characterize Schottky barriers.[215,216] I used single crystal substrates of 0.5 wt% Nb-doped $SrTiO_3$ (111). At room temperature, the resistivity for this doping level is ~ 10^{-2} $\Omega\cdot$cm (Fig. 3.2). The heterostructure in this case will be formed by VO_2 /$LaAlO_3$ /Nb-$SrTiO_3$ (111).

Influenced by the sample preparation conditions, the surface of Nb-$SrTiO_3$ shows numerous different reconstructions.[217,218] For (111)-directed substrates, the polar surface makes the realization of a single terminated surface rather difficult. I used at first the same procedure employed to terminate $SrTiO_3$ (111). The results are shown in Fig. 3.20. After the first steps in acetone, isopropanol and deionized water, the substrates were dipped for 30 sec in Hf-buffered solution and then annealed for two hours at different temperatures. The same annealing temperature used for $SrTiO_3$ (001) was not successful in this case. It yielded a flat surface with profound dips with a height of ≈ 10 nm (Fig. 3.20a). A reduction in the annealing temperature of only 25 °C, however, changed completely the surface topography. The sample annealed at 975 °C shows a step-and-terrace structure with single Ti^{4+} termination. However, the terraces are not straight and pronounced bunching and meandering are present. This forms, in some points, islands that can reach a height of 4 nm. A decrease of the annealing temperature to 950 °C reduced the bunching bud did not prevent the formation of islands. The surface quality degrades if the annealing temperature is reduced further. The formation of layered islands is most likely related to the structural defects caused by the Nb doping that affects the terrace formation during the annealing. In particular it may favor the terrace growth along directions other than the miscut direction. This is evident in Fig. 3.20c that shows terraces along a direction at 30° angle from the miscut direction.

On one of the substrates annealed at 950 °C I grew 5 nm thick film of $LaAlO_3$ (T_s = 800 °C, P_{O2} = 10^{-4} mbar, fluence = 1 J/cm^2) followed by 30 nm of VO_2 under the optimized conditions for VO_2 on $LaAlO_3$ (111). The AFM topography of the VO_2 surface resembles very much the surface of a VO_2 thin film grown directly on a $LaAlO_3$ (111) substrate. The transport measurements performed on the final device, however, indicate that the barrier suffers from shorts and inhomogeneity. This is easy to understand since the height of the islands on the substrate is comparable to the thickness of the barrier itself.

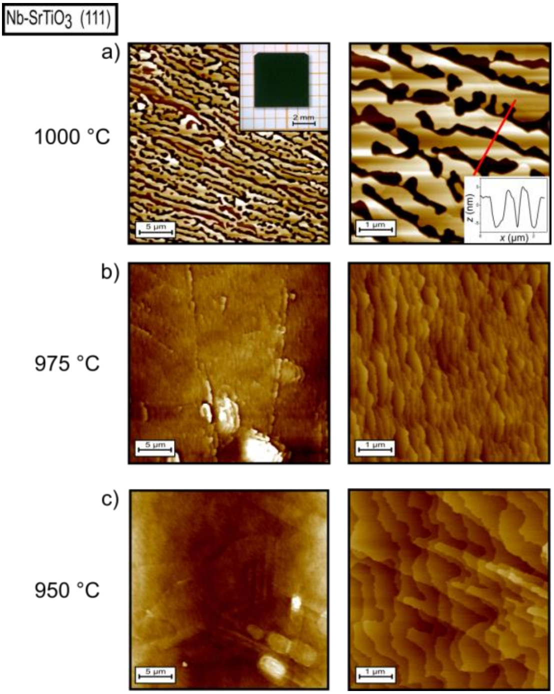

Figure 3.20 AFM topography of 0.5 wt% Nb-doped (111) $SrTiO_3$ substrates chemically treated according to the recipe described in the text and then annealed in oxygen flow at different temperatures (z_a = 10 nm, z_b = 4nm, z_c = 4 nm). A small change in temperature provokes a modification of the surface. Terraces are visible but meandering and bunching lead to the formation of layered islands.

3.5 Conclusions

The pulsed laser deposition of oxide thin films gives the possibility to grow many different compounds with the correct stoichiometry and in the crystalline phase. In this chapter we have observed how sensitive the properties of oxide films are to their crystal structure and how important is to be able to have control on it. The film properties are determined by the substrate characteristics as well as by the deposition conditions. In particular, the substrate crystal structure and orientation and the substrate surface termination have a critical impact on the film structure.

I have optimized the PLD growth of VO_2 thin films on two different substrates: TiO_2 (001) and $LaAlO_3$ (111). In the first case a thin film of rutile VO_2 (001) grows epitaxially and strained up to a thickness of about 10 nm. Above this thickness the film relaxes and creates microbeams presenting strain relaxation gradients that make the film inhomogeneous. The structural difference between the films with different thicknesses is observed also through the $R(T)$ characteristics of the MIT. Very thin films show an abrupt transition at a transition temperature $T_c \approx 300$ °C, lower than the T_c for bulk VO_2 crystal ($T_c \approx 340$ °C). Thicker films show a broad transition that spreads over the temperature range between 300 °C and 340 °C. When $LaAlO_3$ (111) is used as a substrate, monoclinic VO_2 (010) thin films are grown. The film consists of 3D grains aligned along three directions separated by 60°. The size and the density of the grains can be controlled using appropriate deposition conditions. The area between the grains consists of intermixed substrate/film material with low RMS roughness or of 3D islands, according to the deposition conditions. I have shown that the single grains undergo a MIT with temperature and that, below a certain grain density (percolation threshold), no global MIT can be measured. The grain size effects on the MIT have been analyzed. The transition width ΔT is directly proportional to the grain size for the samples considered. The effect is attributed to the reduced amount of structural defects for the larger grains, which provides a lessened number of nucleation points. The crystallography measurements, in fact, indicate an improved crystallinity for the larger grains.

The PLD growth of oxide materials for tunnel junctions has been explored. In particular, I investigated the growth of an heterostructure with (001) rutile structure and another with (111) perovskite structure. In the first case, a thin film of RuO_2 and a substrate of Nb-TiO_2 have been considered as bottom electrodes of the junction while thin films of TiO_2 have been considered as tunnel barrier. In the second case, $SrRuO_3$ and $La_{0.7}Sr_{0.3}MnO_3$ thin films, the 2DEL at the $LaAlO_3$/$SrTiO_3$ interface and a substrate of Nb-$SrTiO_3$ are considered as bottom electrodes, thin films of $LaAlO_3$ as tunnel barrier.

RuO_2 is a highly volatile oxide so it proved rather challenging to obtain a crystalline thin film with a low value of the RMS roughness. However, adjusting the substrate temperature and the oxygen pressure during growth, a thin film with a RMS of 1.7 nm was grown. Despite the reduced roughness, big particulates are deposited on the film surface. The target used for the deposition of RuO_2 has a porous frame. The heating and expansion during laser ablation of the air bubbles present in the target may cause the deposition of the particulates. A similar effect has been found on the film surface of $SrRuO_3$, whose target has, as well, a porous frame. This characteristic may affect negatively the performance of these materials used as bottom electrodes of tunnel junctions, despite the small resistivities that they show. In fact, surface islands higher than the barrier thickness can provoke shorts in the barrier itself. This issue has been found also when the conducting substrates are used as bottom electrodes. In fact, the exposure to high temperatures of Nb-doped $SrTiO_3$ and TiO_2 causes surface islands most likely related to the presence of Nb atoms in the crystals.

Unlike (001) rutile oxides, perovskite oxides along [111] direction are polar materials so the surfaces tend to reconstruct to compensate the polarity. I identified a growth pattern common to all the (111) perovskite oxides under study, induced by the substrate and film polarities. In all the three cases studied, the growth proceeds according to the sequence 2D-3D-2D. Observing the RHEED oscillations, it is noted that, after the first layers grown in 2D mode, the material is subjected to reconstruction induced by the polarity of both the substrate and the film. Following the 3D growth mode, a layer-by-layer growth mode is restored with a damping of the intensity of the oscillations due to increasing surface roughness. I observed that the transport properties as well as the surface quality of the thin films depend on the film thickness. In particular, $SrRuO_3$ (111) thin films show an increase in sheet resistance for thicknesses below 10 nm. $La_{0.7}Sr_{0.3}MnO_3$ (111) thin films show a MIT with temperature with a transition temperature around 165 K. This value is much lower than the expected Curie temperature (335 K) and does not increase with increasing thickness, as it happens for $La_{0.7}Sr_{0.3}MnO_3$ (001) thin films. This behavior could be due to a different doping level or to defects present in the material, which determine a different value of the Curie temperature, regardless of the film thickness. The thin films of $La_{0.7}Sr_{0.3}MnO_3$, however, show a very flat surface for a thickness of 10 nm and a relatively small room-temperature resistivity. The thin film of $LaAlO_3$ (111) with a thickness of 5 nm shows a very small RMS roughness and the step-and-terrace structure coming from the substrate is well reproduced. The resistivity at the $LaAlO_3$/$SrTiO_3$ interface is comparable to the one of a 10 nm thick film of $La_{0.7}Sr_{0.3}MnO_3$ at room temperature.

Chapter 4

4. Characterization of the E-MIT in VO_2 on $LaAlO_3$ (111)

In this chapter I will show that it is possible to induce an E-MIT in a thin film of VO_2 on $LaAlO_3$ (111). A thorough characterization of the EDLT will be performed and the main effects of the grain structure of the thin film on the performances of the transistor will be stressed. In the second part of the chapter I will describe the PLD growth of a tunnel barrier based on (111)-oriented perovskite oxides and the patterning geometries used to characterize it.

4.1 Techniques for patterning oxide-based devices

As described in paragraph 3.2.1, our labs contain many of the machines necessary to pattern the thin films in electronic devices and most of them are connected to the PLD chamber and between them via a transmission line in ultra-high vacuum. In this way, one avoids to expose the sample to external agents during the patterning steps. The properties of oxide films can change drastically when defects are implanted in the film. The patterning processes need to be controlled precisely not to damage the film after growth. Because of the relatively high temperatures used during the PLD growth of crystalline oxide layers, the possibility of *in-situ* patterning is reduced. In fact, the application of an external material such as organic photoresist and metallic hard masks on the substrate surface during growth can provoke the reduction of the quality of the oxide layers because of the introduction of contaminations and hard-baked material. For the devices described in this work, the patterning process is mainly performed after the growth of the thin films. It is recommended to have the least number of steps in the patterning process and the least aggressive techniques to the materials in use. In fact, the bigger the number of steps and the bigger the possibility of failure, the more difficult is the “debugging” process.

In the following, I will describe briefly the techniques used for the patterning of the oxide layers used in this work.

Optical photolithography: it is used to project a pattern onto a substrate so to have only some areas of the substrate exposed to external agents. This is achieved by covering the substrate with an organic fluid, called “photoresist”, that is sensitive to UV light. Controlling the photoresist thickness, the photoresist heating steps, the exposure time and the dissolving time in a basic solution, it is possible to define, through an optical mask, areas of the surface which are covered or not by the photoresist. This technique is useful to design objects which are of the order of tens of nanometers. For lower dimensions, undercut effects start to be relevant and prevent defined structures to form. I use the mask aligner MJB4 by Süss MicroTec and the positive photoresist AZ 1512HS by MicroChemicals.

Ion milling: with this technique it is possible to remove atoms from a substrate surface via collision processes (dry etching). The molecules of an inert gas (usually Ar) are ionized and accelerated towards the substrate surface. The process takes place under vacuum (10^{-4} mbar) so to allow a sufficiently large mean free path of the ions. During the process the substrate is cooled via a water cooling system. The etching rates may vary according to the acceleration voltage. I use a machine with an acceleration voltage of 600 V. At these conditions, the etching rate for crystalline oxides is around 2 nm/min. One of the disadvantages of ion milling, however, is that it may damage the substrate surface and implant ions that would make the surface charged if the milling time is relatively long.

Chemical etching: chemical solutions can react with oxide films and dissolve them with a controllable etching rate dependent on the solution concentration (wet etching). However, if the etching is used to pattern a substrate according to a precise geometry, the etchant has to react with the oxide but not with the photoresist that forms the geometry. Since the photoresist used in this work is dissolved in basic solutions, only acid solutions can be used for the wet etching of the multilayer. I tested Cr-etchant (aqueous solution of $(NH_4)_2[Ce(NO_3)_6]$ and $HClO_4$) and 35% H_2O_2 solution. The Cr-etchant etches VO_2 with a rate of 0.3 nm/sec. It also etches $SrRuO_3$ with a much higher rate. In a 1:5 water dilution of Cr-etchant, $SrRuO_3$ (111) shows a rate larger than 6 nm/sec. The substrate of $SrTiO_3$ (111) is unaffected by the etchant and stays insulating after the etching. Because of the large difference of etching rates, however, it is difficult to obtain a selective etching of VO_2 when the multilayer VO_2 /$LaAlO_3$ /$SrRuO_3$ /$SrTiO_3$ (111) is immersed in Cr-etchant solution. The $LaAlO_3$ barrier, in fact, is not thick enough to prevent the $SrRuO_3$ layer from dissolving before VO_2. On the contrary, using a solution of H_2O_2 it is possible to etch only VO_2 with a rate of 0.5 nm/sec. Differently to what happens with dry etching, however, the step edge that forms with wet etching is not abrupt and this could represent an issue for very small devices. For this reason, in this work I will mainly use dry etching, unless otherwise stated.

Electron beam evaporation: it is a physical vapor deposition technique used to coat a substrate with a thin layer of material and with a very small growth rate. An electron beam emitted by a hot cathode is accelerated and directed towards the target material using electric and magnetic fields. Most of the energy transferred to the target material transforms in thermic energy which causes the evaporation or sublimation of the material which is contained into a ceramic crucible. The evaporated material moves to the whole chamber in line of sight. To provide a large mean free path, the process takes place in a base pressure of 10^{-8} mbar. I use this technique to evaporate metals (mainly Au and Ti) to deposit the contact pads on the devices after a step of optical photolithography to define the geometry. I used a machine by MBE Komponenten. The acceleration voltage is 8 KV and the current is of the order of 100 mA and varies according to the material and the required deposition rate. The deposition rate used is around 1.5 Å/sec. In order to avoid shading effects, the substrate rotates during deposition. Au films may not stick on oxide surfaces. This is the reason why I deposit a thin layer of Ti under it. The Ti layer needs to be covered by a different metal so to avoid surface oxidation. Another important parameter to define is the metal film thickness since, above a certain thickness, the metals used may form flakes that cause difficulties when bonding the contact pads.

4.2 Fabrication of the devices

I adopted three different device geometries for three kinds of measurements. (*i*) VO_2 thin films have been patterned in EDLT configuration to characterize the behavior of the material grown on different substrates (*Thin film geometry*). (*ii*) The $LaAlO_3$ tunnel barrier has been characterized for the sequence Au/ $LaAlO_3$/ $SrRuO_3$/ $SrTiO_3$ that does not comprise VO_2 as top electrode in order to simplify the structure. The device geometry is called *Corbino geometry* and is made of a smaller number of steps compared to the patterning of the complete heterostructure. (*iii*) The multilayer has been patterned in a geometry that allows for electrolyte gating at the surface together with cross-section tunnel transport measurements (*Multilayer geometry*).

The *thin film geometry* was used for the characterization of the EDLT based on a thin film of VO_2 grown on a TiO_2 (001) or $LaAlO_3$ (111) substrate. The thin film of VO_2 was patterned first in a Hall bar geometry (Fig. 4.1) using photolithography and ion milling. The area that has been ion milled is filled with amorphous Al_2O_3 so to provide an insulating layer on which to deposit the contacts. The ion milling, in fact, may charge the etched area and cause a short between the side-gate contact and the VO_2 channel. A big gold gate pad is deposited next to the channel at such a distance to ensure a resistance between gate and channel higher than the resistance of the drop of IL to be put on top of the area. In this way, the potential applied between gate and channel will drop mainly across the IL. In order to avoid the saturation of the ionic diffusion during the gating, the ratio between the areas of the gate and the channel has to be decided according to the ratio between the radii of the ions forming the IL and the electric configuration used. For some of the electrolytes tested (e.g. PEGMA-BEMA) the volume ratio of the molecules forming the IL can reach a value of four. In the configuration used, the larger ions accumulate on the gate pad. The gate pad has to have an area of at least four times the channel area to let all the ions relative to a certain voltage collect on the channel surface. The contact lines to the channel are directed to the external borders of the sample so to be sure that the bonding wires are not in contact with the IL. After the evaporation of the contacts, a thin layer of resist is patterned and hard-baked to protect the whole surface from contacting the IL except for VO_2 and side gate. The high resistance of the photoresist ensures that the gate current will flow only in the circuit gate-IL-VO_2. The measurements were performed both in side-gate and top-gate configuration. In top-gate configuration the side pad is not contacted but a small gold foil is put on the drop of IL. Additionally, a glass ring is glued on the sample to contain the drop and let the bonding to the pads outside of it. This configuration has the advantage of a better control of the IL volume which should not change during the measurement. Furthermore in top-gate configuration there is no contribution to the current from the substrate as in the case of the side-gate configuration, making it easier, for example, to measure the IL resistance. Figure 4.1 shows pictures of a sample of VO_2 patterned in side-gate (a-b) and top gate (c, d) configuration.

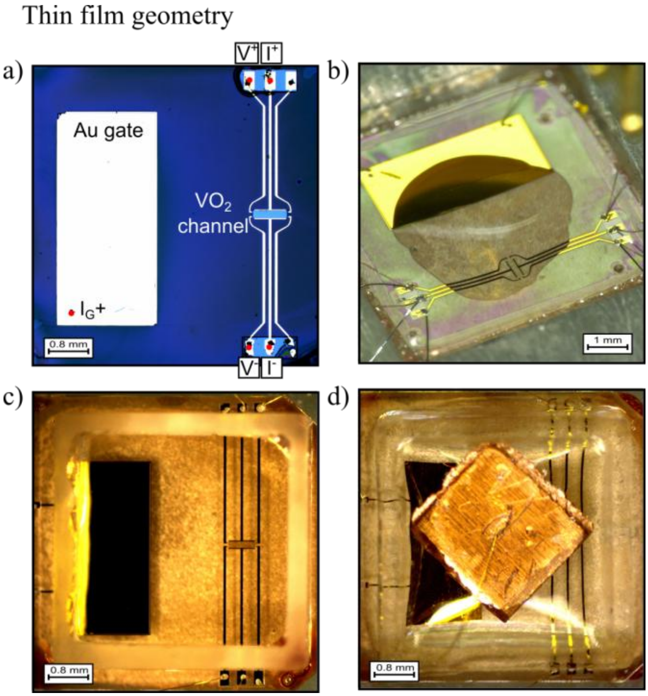

Figure 4.1 Optical images of devices used for the characterization of the EDLT in side-gate (a-b) and top-gate (c-d) configuration. The channel dimensions are 470 μm x 110 μm. In (b) the drop of IL DEME-TFSI has been put on the sample and in (d) a Cu pad (for testing reasons) has been put on the drop that is held in place by a glass ring.

The geometry shown in Fig. 4.2a (*Corbino geometry*) has been used for the characterization of the $LaAlO_3/SrTiO_3$ interface and for the measurement of the barrier resistance in the simplified structure Au /$LaAlO_3$ /$SrRuO_3$ /$SrTiO_3$ (111). The geometry is similar to that of a Corbino ring: the most internal ring and the most external ring have two contacts each to the interface or to the bottom electrode; those areas are etched with ion milling to the interface and then filled with titanium. The intermediate ring is made of a gold layer contacting the surface. Using this geometry, the resistance of the bottom electrode can be measured in 4-wire configuration and the barrier resistance can be measured across a relatively large area of 1.5 mm^2.

The design of the device for the multilayer (*Multilayer geometry*) has to combine the two designs described previously since it has to allow the gating of the VO_2 channel and, at the same time, the measurement of the tunnel resistance. Figure 4.2b shows a photograph of the final device and Fig. 4.3 a sketch of the steps used in its production. The heterostructure goes through two steps of ion milling and amorphous Al_2O_3 evaporation. The etching allows defining squares of different sizes for the different layers. The Al_2O_3 layer is used as an insulator. Between two steps, optical photolithography is performed to define the geometries. For the final device, four contacts are connected to the VO_2 film on top of the multilayer and two contacts are connected to the bottom electrode. In order to avoid shorts between the contacts to the VO_2 layer and the bottom electrode, an amorphous layer of Al_2O_3 is deposited before the contact evaporation. This is a critical patterning step since shorts in the Al_2O_3 layer due to the presence of particulates and/or holes or at the step between different layers, can prevent tunneling from taking place. Another critical step is the second etching process used to remove the first two layers of the structure and reach the bottom electrode. It is important to control exactly the etching rate so to not reduce too much the thickness of the bottom electrode. Below a certain thickness, in fact, the resistance of $SrRuO_3$ increases. The last patterning step consists of covering the device with a thin layer of photoresist patterned in such a way to leave uncovered only the VO_2 square and the side gate. This way, only these two parts of the device will be in contact with the drop of IL. The photoresist is hard-backed at 120 °C for two minutes to stabilize it against possible chemical reactions with the IL. Heating the photoresist at higher temperatures can create cracks that would nullify the insulation. On a 5 mm x 5 mm large sample it was possible to fabricate six devices of different areas (the length of the side of the VO_2 square goes from 50 μm to 430 μm) together with a side gate at a distance of 1.3 mm from the devices. Figure 4.2d shows the same geometry reproduced on a 10 mm x 10 mm substrate. A large number of devices increases the probability of finding a working one. However, the difficulties met for the devices on a small substrate were amplified for the case of the bigger substrate. For example, the temperature homogeneity during growth for such a big substrate is a serious issue which leads to degraded thin films.

I had the possibility to execute personally all the steps of the device production. In this way it was easier to locate and correct the flaws in the process.

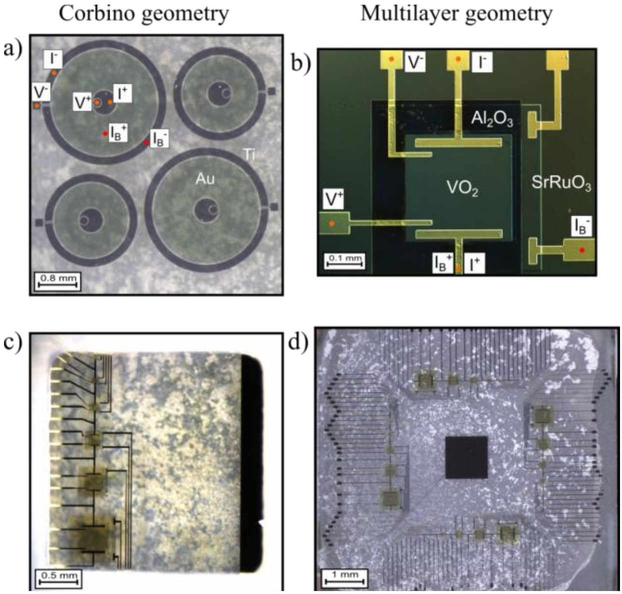

Figure 4.2 Optical images of the devices used to characterize the $LaAlO_3$ *barrier (a) and the multilayer (b). In (a) the Ti ring reaches the bottom electrode while the Au ring is on the top surface. (c) Image of a sample with an area of 5x5* mm^2 *patterned with six devices of different areas and a side gate; a glass ring is glued on top. (d) Image of a sample with an area of 10x10* mm^2 *patterned into 24 devices.*

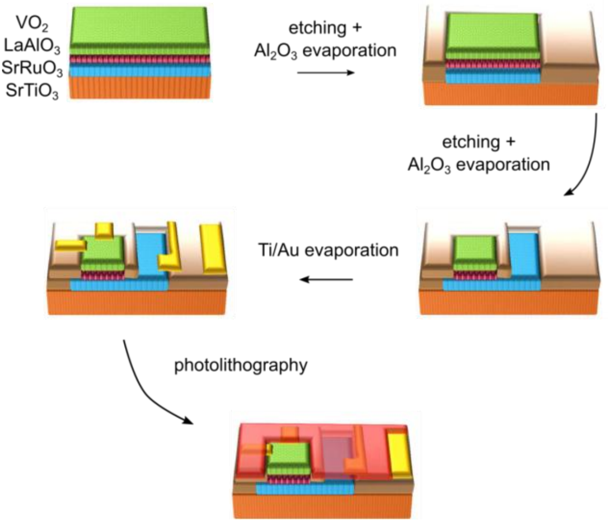

Figure 4.3 Patterning process for the multilayer geometry. Before each step an optical photolithography is performed to define the geometry. The first two steps consist of ion milling (dry etching) and PLD deposition of amorphous Al_2O_3 *at room temperature. The Ti/Au evaporation creates the side gate and the contacts to the* VO_2 *area and the* $SrRuO_3$ *area. The photoresist deposited in the last step is hard-backed at 120 °C for two minutes and it is patterned in such a way to leave the* VO_2 *square and the side gate uncovered.*

4.3 Study of EDLTs based on thin films of VO_2 on $LaAlO_3$ (111)

In this paragraph I will present the characterization of the EDLT based on 30 nm thick films of VO_2 grown on $LaAlO_3$ (111) patterned according to the *thin film geometry*. I have obtained similar results using thin films of VO_2 grown on TiO_2 (001). The differences between the thin films have already been shown in the previous chapter. Here the consequences of these differences on the performance of the EDLT will be emphasized.

Characterization of the IL

The IL used in this work is DEME-TFSI (N,N-diethyl-N-(2-methoxyethyl)-N-methylammonium bis(trifluoromethylsulphonyl-imide). It is a mixture of the two polymers $DEME^+$ and $TFSI^-$. At room temperature the IL has a conductivity of 3.5 $mS\cdot cm^{-1}$ and decreases quickly with temperature.[219] At 240 K it condenses into a rubber-like state and the conductivity reaches a plateau. In this phase, most of the chemical reactions with the electrode surface are suppressed.[220] At 182 K the IL undergoes a glass transition and the conductivity goes to zero. DEME-TFSI is stable in the range [-3 V; 3 V] at room temperature. Beyond this range, redox reactions may take place at the IL/electrode interface.[219] The stability window widens at lower temperatures. The IL was dehydrated before usage. It was heated at 200 °C overnight inside a glovebox filled with nitrogen. The amount of water after the treatment was determined to be below the minimum measurable value with Karl-Fischer titration.

Preliminary measurements were performed to characterize the system Au/IL/VO_2. Understanding the behavior of the double interface forming the EDLT is important to interpret the performance of the transistor. I used a LCR meter (Keysight E4980A) to measure the complex impedance of the system versus frequency and gate voltage. In these measurements, the gate pad and the source contact of the VO_2 channel are connected to the device.

The equivalent circuit for such a system can be simplified to the one shown in Fig. 4.4a. It consists of the RC circuit related to the bulk IL in series with the RC circuit related to the EDL forming at the interface IL/VO_2 in series with the resistance of the VO_2 channel. The contribution of the interface Au/IL can be neglected considering that the area of this interface is much larger than the area of the EDL at the IL/VO_2 interface. The resistances of the bulk IL and of the VO_2 channel are, in general, at least two orders of magnitude smaller than the resistance of the EDL. The external voltage will mostly drop on the electric double layer. The bulk IL has smaller capacitance than the EDL, and therefore also smaller time constant. This is observable in the measurement of the phase angle θ of the complex impedance versus frequency. Since a pure capacitive behavior of an RC circuit always induces a response with a phase angle close to -90°, the phase oscillations in θ indicate different frequency domains, relative to different capacitances. In particular, the one at high frequencies is related to the bulk IL, while the one at lower frequencies is related to the EDL. At frequencies larger than 1 MHz, the impedance component related to the external circuit becomes significant. In my measurements I used frequencies $< 10^2$ Hz. The capacitive contributions to the impedance will be neglected. The EDL in the system under study has a resistance of $\sim 10^7$-10^8 Ω and a capacitance of ~ 20 μF/cm^2 at the frequencies used in this work. From the measurement of the capacitance and of the charging and discharging characteristics of the EDL, it was possible to calculate the charge accumulated on the electrode surfaces (for a detailed description of the setup used, refer to the thesis of G. Pfanzelt[221]). Figure 4.4b shows the result obtained. The charge is limited by the VO_2 channel that is the electrode with smaller area. From the value of the charge at different gate voltages it is possible to calculate the electric field present inside the VO_2 channel until a depth equal to the Thomas-Fermi screening length. One can estimate the value of the critical electric field E_c necessary to ionize electrons in VO_2 through field-induced Poole-Frenkel effect: $E_c \sim 10^7$ V/m.[222] It has been observed in two-terminal devices that when the electric field in VO_2 reaches this order of magnitude, an electrostatic MIT is induced.[9] However, the resistance change is much smaller than the one obtained through EDLTs. For the system under study, this value of the electric field is reached for gate voltages below 2 V. This value is in the stability range of the IL so no irreversible chemical reactions should be induced at the interface. This qualitative analysis is useful to foresee the response of the device under study.

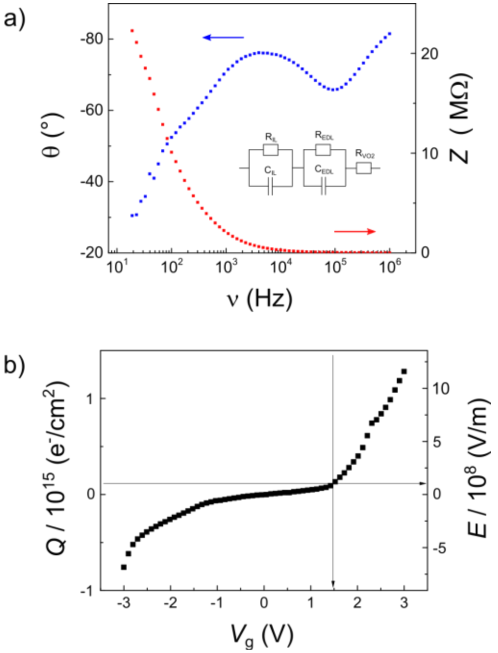

Figure 4.4 Characterization of the system Au/IL/VO_2 relative to the device with thin film geometry.(a) Measurement of the phase angle θ and absolute value Z of the complex impedance of the system. The inset shows the simplified equivalent circuit. The interface Au/IL is neglected. (b) Measurement of the charge Q accumulated on the electrode surface and relative electric field E induced in the VO_2 channel for different gate voltages V_g.

Characterization of the EDLT

For the characterization of the EDLT the setup shown in Fig. 4.5 was used. A Lock-In amplifier (Zurich Instruments, HF2LI) is connected to the channel of the device so to perform a AC 4-wire measurement of the channel resistance R_{ch}. The second channel of the Lock-In measures the voltage drop across the load resistance R_{L} so to know the current flowing in the circuit. With a Source-Meter Unit (Keithley 2612A) a DC voltage can be applied between the gate and the source contact of the channel through the drop of IL. The device is put inside a PPMS whereby the temperature can be controlled. Inside the PPMS there is a nitrogen atmosphere at 10 Torr. I wrote a LabView program capable of performing I-V sweeps while reading the temperature from the PPMS and the values measured by the two devices.

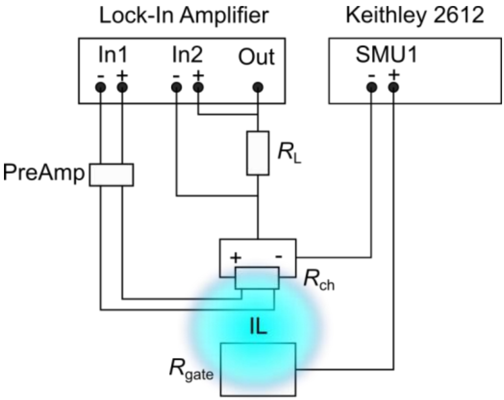

Figure 4.5 Measurement setup: with the Lock-In amplifier an AC current is applied to the VO_2 channel and a voltage is measured; with a source-meter unit a DC voltage is applied between gate and channel, across the drop of IL.

In the following, the results obtained for the device built out of a VO_2 thin film on $LaAlO_3$ (111) subjected to different conditions are described.

Gate induced metallic state

Figure 4.6 shows the measurement of the resistance of the VO_2 channel at sweeping temperature and for different gate voltages applied across the drop of IL. This measurement has been performed in side-gate configuration, with a drop volume of 8 μL. I applied an AC output voltage with an amplitude of 1 V and a frequency of 20 Hz to the series of resistances ($R_L + R_{ch}$), with R_L = 100 KΩ, and a varying DC gate voltage V_g between gate and source during a temperature sweep with a rate of 1 K/min. Before putting the drop of IL, a MIT is observed at the transition temperature comparable to the one reported in this work for the thin film of $VO_2/LaAlO_3$ (111). With increasing gate voltages applied across the drop, the resistance in the insulating phase decreases until no MIT is observable at a gate voltage of 1.5 V. The resistance of the metallic phase just above the MIT increases with increasing gate voltage. This effect has been observed also for VO_2/TiO_2 (001) and has been attributed to the formation of oxygen vacancies at the surface of the thin film.[122] The critical voltage V_c at which the insulating phase disappears is different according to the substrate used. According to my experience and the results found in literature, it is possible to switch thin films of VO_2 on TiO_2 (001) with a voltage $V_c \leq 1$ V while thin films of VO_2 on $LaAlO_3$ (111) and VO_2 on Al_2O_3 $(10\bar{1}0)$ need $V_c \geq 1.5$ V. This behavior is not reproduced, however, when the gate voltage is swept at constant temperature. In this case, as it will be seen in the next paragraph, the transition voltage does not differ systematically according to the substrate used.

Switching loops

Figure 4.7a shows the measurement of the resistance as a function of gate voltage at constant temperature. This measurement was repeated at 300 K and 240 K. The gate voltage was swept in the range [-3 V, 3 V] with a rate of 2 mV/s. The resistance undergoes through a transition to a lower value at a certain transition voltage V_t. At 300 K the transition has not recovered when a reversed bias is applied while it has mostly recovered at 240 K. However, at lower temperature, V_t increases and the transition amplitude is reduced. A reason for these effects could be that at lower temperatures the ionic conductivity of the IL is reduced and starting from 240 K most of the chemical reactions that may take place at the interface IL/VO_2 are suppressed. Figure 4.7b shows the measurement of the leakage current through the drop performed on the same sample in top-gate configuration and for the gate voltage range [-4 V, 4 V]. In this configuration, unlike in side-gate configuration, the current flowing from gate to channel does not comprise the current flowing through the substrate. Only the leakage current through the drop is measured. At 300 K the leakage current increases for voltages above 3 V and below -2 V. This increase could be a sign of Faradaic reactions taking place at the interface between IL and VO_2 channel.[83] At 240 K the leakage current does not change significantly in the range considered. The transition voltage at 300 K is, however, below the value where the leakage current starts to increase. Furthermore, at this gate voltage, the electric field necessary for ionization in VO_2 and, consequently, for the electrostatic MIT should have been reached.

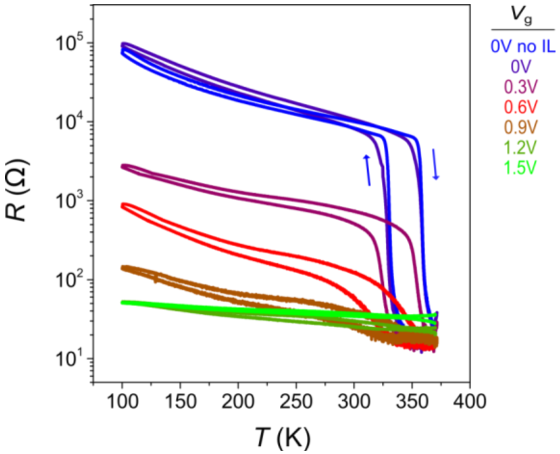

Figure 4.6 Measurement of the resistance of the VO_2 channel versus temperature for different gate voltages V_g applied between gate (V_g^+) and source (V_g^-) contact across the drop of IL. An AC current with a frequency of 20 Hz flows through the VO_2 channel while the temperature sweeps at a rate of 1 K/min.

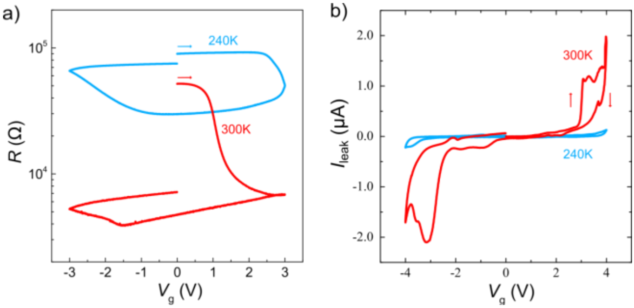

Figure 4.7 (a) Measurement of the resistance of the VO_2 channel versus gate voltage at two temperatures. (b) Leakage currents through the drop of IL versus gate voltages at two different temperatures. The measurement was done in top-gate configuration. The sweep rate is 2 mV/s.

Multiple cycles

I performed the voltage sweep on the same sample multiple times consecutively at a temperature of 270 K. After each sweep the resistance recovers to a value lower than the initial one, causing the reduction of the transition amplitude. After 3 cycles, however, no further reduction of the maximum resistance value is observed and the amplitude of the transition stays constant. This indicates that for any picture adopted to describe the E-MIT, the process is not symmetric respect to the gate voltage only for the first few cycles (for example because of irreversible chemical reactions, coercive electric field, etc.). Afterwards an equilibrium is reached between the two parts of the transition (for positive and negative gate voltages).

Stability of the gate induced metallic state

In order to characterize the electric-field-induced metallic state in VO_2 thin films, it is interesting to measure the channel resistance after gating and after the removal of the drop of IL to see whether the metallic state persists. This has been done by some groups and it has been found that it depends on the substrate on which the thin film is grown.[13,86] In particular, the insulating state is not recovered after the removal of the drop for thin films of VO_2 on Al_2O_3 (0001) and Al_2O_3 $(10\bar{1}0)$ while it is completely recovered for VO_2 on TiO_2 (001).[13,122] In the latter case, the MIT with temperature observed before gating is reproduced after gating and drop removal. Figure 4.8 shows the measurement of the resistance with temperature of a channel of VO_2 on $LaAlO_3$ (111) before the application of the drop of IL (pristine), during the application of a gate voltage of 1.5 V across the drop (gated) and after the removal of the drop in acetone and isopropanol sonication (washed). The insulating state is not recovered. Nakano *et al.*[13] attribute the absence of recovery to the fact that the film of VO_2 grown on Al_2O_3, compared to the one grown on TiO_2, has a larger surface roughness and a higher transition temperature, which could favor chemical reactions at the interface with the IL. VO_2 grown on $LaAlO_3$ (111) has a particular large surface roughness and the transition temperature is close to the one of VO_2 grown on Al_2O_3 since the film is totally relaxed. The mechanism driving the gate-induced transition could also be similar in the case of VO_2 on Al_2O_3 and on $LaAlO_3$ (111).

Surface orientation dependence of the E-MIT

It has been suggested that the E-MIT observed in VO_2 is due to the formation of oxygen vacancies triggered by the large electric field applied at the surface. The removal of a significant amount of oxygen atoms would provoke a lattice expansion along the rutile *c* direction. Along this direction, chains of edge-sharing VO_6 octahedra are present and can allow for the expansion and contraction of the VO_2 lattice during IL gating. This explanation agrees with the observation made by Jeong *et al*.[86] that no gating response is present for thin films of VO_2 grown on different crystal directions of TiO_2 for which the *c* axis lies in plane. The clamping of the VO_2 lattice to that of the TiO_2, in fact, would prevent the modification of the octahedra.

According to the results shown in this work, however, it is possible to gate thin films of VO_2, with transition characteristics similar to the ones found in literature, even for the lattice direction (010) for which the *c* axis lies in-plane.

Double transition

For some of the thin films of VO_2 on $LaAlO_3$ (111) investigated, two MITs with different transition temperatures were observed when the IL was applied. Figure 4.9 shows the measurement of the resistance with temperature for different gate voltages applied across the drop. At around 240 K a second MIT is observed. At this temperature the IL undergoes a transition to a rubber-like phase. The change in viscosity of the IL may modify the strain applied on the VO_2 surface and, consequently, move the transition temperature. To comprehend how much the strain affects the transition temperature, one can consider the comparison between a VO_2 film grown on Al_2O_3 $(10\bar{1}0)$ and on TiO_2 (001); in this case, a change in out-of-plane lattice parameter of 1% causes a change in transition temperature of ≈ 50 K.[12] Considering the topography of a film of VO_2 on $LaAlO_3$ (111), the effective surface area is particularly large so the effect could be not negligible. A double transition was observed also for VO_2 on Al_2O_3 $(10\bar{1}0)$.[122] In that case, the second transition takes place at around 190 K and it is attributed to the presence of a V_2O_3 phase inside the film caused by the film oxygen reduction. V_2O_3, in fact, shows a MIT with transition temperature around that value. It is, however, worth noticing that no other phase of vanadium oxide has a transition temperature around 240 K and that 190 K is also the temperature at which the IL freezes. Furthermore, the thin film of VO_2 grown on Al_2O_3 has a large surface roughness and consists of grains of a few nanometers of height.

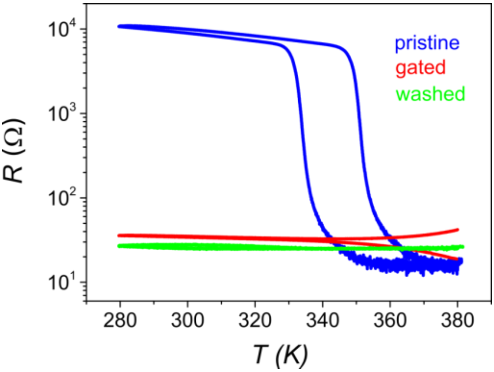

Figure 4.8 Measurement of the resistance versus temperature for the VO_2 channel in three states: (pristine) No gate voltage is applied; (gated) A constant gate voltage of 1.5 V is applied during the measurement; (washed) The IL has been removed putting the sample in a sonicated bath of acetone and isopropanol, consecutively, and then the resistance has been measured.

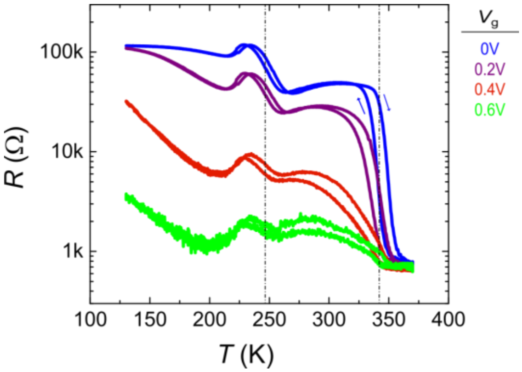

Figure 4.9 Resistance versus temperature at different gate voltages for a VO_2 channel. V_g^+ is applied to the gate while V_g^- is applied to the source contact of the VO_2 channel. For this sample, a double transition is observed at two different transition temperatures (marked by the dashed lines).

4.4 Approaching the construction of oxide-based tunnel junctions

So far I analyzed the different parts constituting the tunnel junction separately. I went through the optimization of the PLD growth of different oxide thin film layers and the analysis of the EDLT that should be built on top of the tunnel junction. I also described the patterning process outlined to obtain the final device. When putting the different parts together, one has to pay attention that the whole process is not damaging the parts already present in the device. At first, the knowledge collected during the PLD growth of the different layers has to be unified to perform the growth of the heterostructure. If the deposition conditions for the different layers are too different from each other, the growth of a layer could affect the previous one. This happens in the case of $SrRuO_3$ and $LaAlO_3$. The former has to grow at relatively high oxygen pressure (10^{-1} mbar) to avoid the formation of oxygen vacancies while the latter grows optimally at low pressure (10^{-4} mbar) and high temperature (800 °C). Changing the deposition conditions so drastically after the growth of the thin film of $SrRuO_3$, creates dips on the film surface most likely coming from the evaporation of RuO_2, that is a highly volatile compound. However, $LaAlO_3$ can grow in form of thin films of acceptable quality in a wide range of pressures and temperatures. After an optimization process, the growth conditions that were chosen for the sequence VO_2 /$LaAlO_3$ /$SrRuO_3$ /$SrTiO_3$ (111) are summarized in Table 5.

The topography measured by AFM of the surfaces of the different layers of the heterostructure show that (*i*) the step-and-terrace structure of the substrate is maintained for the first two layers, (*ii*) dips with a depth of a few unit cells are present on the surface of a part of the $SrRuO_3$ thin films, (*iii*) the structure of VO_2 made of aligned grains is reproduced when the material is grown on top of the other two layers of the heterostructure. I performed a 4-wire measurement of the resistance of the multilayer with varying temperature, by gluing four contact wires on the top layer of the heterostructure. The result is shown in Fig. 4.10. Since the area between the contacts is rather large, the probability of shorts from the VO_2 top layer to the bottom electrode is quite large. For this reason the measured resistance is the sum of the resistances of the three layers in parallel. The value of the resistance is small and the main contribution is given by the resistance of $SrRuO_3$. The kink characteristic of this material is observed at 150 K. The MIT characteristic of VO_2 is still observable even if the relative change in resistance is smaller compared to the case of the single thin film. The VO_2 thin film on top of the multilayer, then, preserves the electronic properties that are observable for the thin film grown on a $LaAlO_3$ (111) substrate. For this reason, the behavior observed for the EDLT should also be reproducible for the multilayer.

	Substrate temperature (°C)	**Pressure (mbar)**	**Fluence (J/cm^2)**	**Laser frequency (Hz)**	**Laser spot area (mm^2)**	**Film thickness (nm)**
$SrRuO_3$ (111)	650	0.1	1.2	2	2.0	10
$LaAlO_3$ (111)	650	10^{-4}	1	1	2.0	5
VO_2 (010)	425	10^{-2}	1.2	2	4.2	30

Table 5 Deposition conditions used for the PLD growth of the three layers of the heterostructure consecutively on a substrate of $SrTiO_3$ (111).

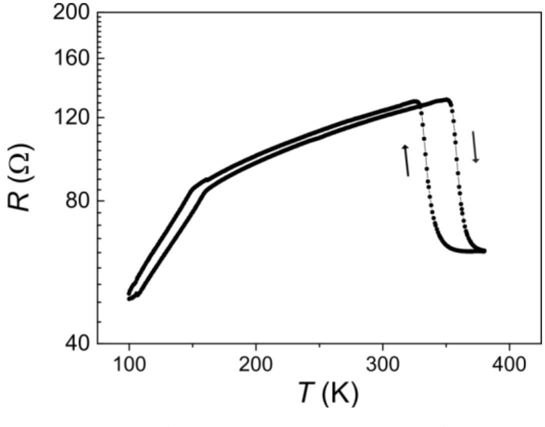

Figure 4.10 Measurement of the resistance versus temperature of the heterostructure VO_2 /$LaAlO_3$ /$SrRuO_3$ /$SrTiO_3$ (111). Four Ag contacts have been glued on the surface of VO_2 at a distance of ~ 3 mm. The sweeping rate is 1 K/min.

The next step is the characterization of the tunnel barrier. In particular, it is important to identify possible leakage defects and the value of the barrier thickness suitable for the tunneling transport. The heterostructure made of $LaAlO_3$ /$SrRuO_3$ /$SrTiO_3$ (111) was patterned in a *Corbino geometry*. In this geometry, the resistance of the electrode together with the resistance of the barrier can be measured at different temperatures. The result is shown in Fig. 4.11. The electrode resistance is measured in 4-wire configuration while the barrier resistance is measured in 2-wire configuration over an area of 0.13 mm^2. The barrier resistance is at least two orders of magnitude larger than the resistances of the bottom electrode and of the VO_2 layer in the metallic phase induced by IL gating. However, this behavior was obtained only for one sample and was not reproducible for the complete heterostructure when the *multilayer geometry* was adopted, even for the smallest device with an area of 0.003 mm^2. One of the main issues was related to the reproducibility of the quality of the $SrRuO_3$ thin films. As already described in the previous chapter, the PLD growth of this material on a substrate with [111] crystal orientation is extremely sensitive to small changes in the deposition conditions. Furthermore, the porosity of the target increases the probability of depositing particulates on the substrate which create shorts in the thin barrier grown on top. For this reason other bottom electrodes were tested, such as $La_{0.7}Sr_{0.3}MnO_3$.

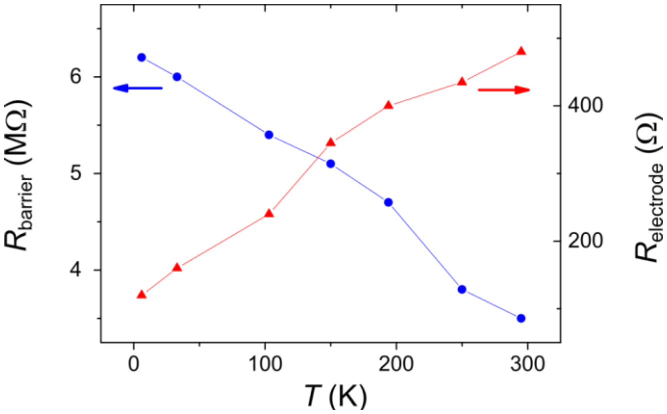

Figure 4.11 Measurement of the resistance versus temperature for the heterostructure $LaAlO_3$ /$SrRuO_3$ /$SrTiO_3$ (111) patterned in Corbino geometry. The resistance of the $SrRuO_3$ bottom electrode (red) is measured in 4-wire configuration, the resistance of the $LaAlO_3$ barrier (blue) in 2-wire configuration.

Besides the consecutive PLD growth of the different layers, the patterning process used in the *multilayer geometry* may damage the heterostructure and cause shorts that prevent any tunnel transport measurement. For this reason, a different geometry was adopted so that no post-growth treatment had to be used in order to measure the tunnel resistance of $LaAlO_3$. A sketch of the device is shown in Fig. 4.12. A platinum hard mask has been used to pattern the bottom electrode, the insulating barrier and the gold contacts. The material used as bottom electrode is $La_{0.7}Sr_{0.3}MnO_3$. Using the growth conditions described in chapter 3, a 10 nm thick film of $La_{0.7}Sr_{0.3}MnO_3$ was grown on a substrate of $SrTiO_3$ (111), followed by a thin film of $LaAlO_3$ of different thicknesses. Also in this case, the step-and-terrace structure of the substrate is maintained for the other two layers.

Figure 4.13 shows the I-V characteristics measured from the top gold contact to the bottom gold contact, for different nominal thicknesses of the barrier. The thickness of $LaAlO_3$ is calculated based on the number of laser shots and the growth rate as measured using the first RHEED oscillations. The non-Ohmic behavior indicates that a barrier to the electron transport from bottom and top electrode is present but the thickness extrapolated from the data through Brinkman-Dynes-Rowell (BDR) fitting[223] does not agree with the nominal thickness (see Appendix). This could be a consequence of the inhomogeneity of the barrier related to the presence of structural defects. However, the insulating behavior of the barrier was not reproduced when the complete multilayer grown in the same deposition conditions was patterned according to the *multilayer geometry*. The patterning process is the reason of the shorts between the top VO_2 layer and the bottom electrode. The design needs to be improved so to reduce further the number of steps needed to build the final device and to introduce less aggressive patterning techniques.

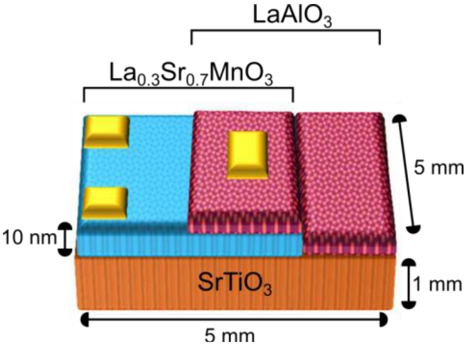

Figure 4.12 Sketch of the device used to measure the tunnel resistance of $LaAlO_3$. This geometry has been obtained using a platinum hard mask mounted on the 5 mm x 5 mm substrate during the PLD growth of the different layers. This way, no post-growth patterning process was performed. The thickness of the $LaAlO_3$ layer was varied. Gold wires were glued on the gold pads present on top of the thin films.

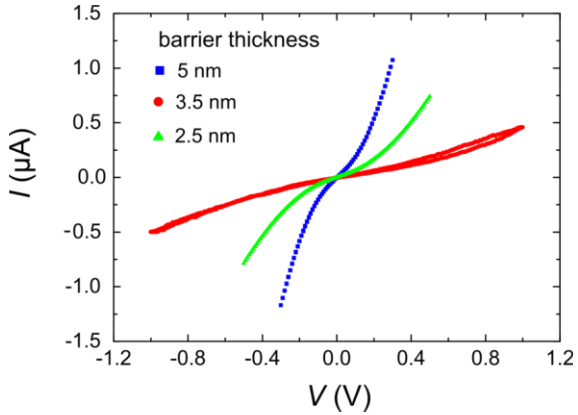

Figure 4.13 I-V characteristics of the tunnel junction Au /$LaAlO_3$ / $La_{0.7}Sr_{0.3}MnO_3$ /$SrTiO_3$ patterned according to the geometry shown in Fig 4.12 and for different nominal thicknesses of the $LaAlO_3$ barrier. The nominal thickness is calculated through the number of laser shots and the growth rate defined by the RHEED oscillations. The measurement has been performed in ambient conditions using a source-measure unit (Keithley 2612).

4.5 Conclusions

The peculiar structure of VO_2 on a $LaAlO_3$ (111) substrate has direct consequences on the MIT induced with temperature. In particular, the transition temperature is similar to the one in bulk VO_2 because the film is relaxed and the transition properties change according to the grain size. In this chapter I have determined the characteristics of the electric-field-induced MIT in such a thin film of VO_2. I have shown that it is possible to gate a thin film of monoclinic (010) VO_2 on $LaAlO_3$ (111) patterned in an EDLT configuration and using DEME-TFSI as IL. The fact that the transition temperature of the MIT is above room temperature gives the opportunity to induce the E-MIT at room temperature, unlike the cases shown in literature so far where the gating takes place always at a temperature ≈ 270 K. Furthermore, the thin films analyzed are very different from the thin films grown on TiO_2 (001) which are strained (below a certain thickness), in (001) rutile phase and with a very low surface RMS. The comparison between the behaviors of the devices built out of these two kinds of film provides useful information for the understanding of the phenomena. In particular, we have observed that the films grown on $LaAlO_3$ need a higher critical voltage to erase the insulating phase in the temperature sweeps. The critical voltages are similar to the ones used for the E-MIT of VO_2 on Al_2O_3 ($10\bar{1}0$) where the (001) rutile VO_2 film is completely relaxed and with a large surface RMS. Another similarity between the films on the two substrates, unlike the case of VO_2 on TiO_2, is the stability of the gate-induced metallic state after the removal of the drop. If the film is relaxed, it is needed to reach higher temperatures to observe the MIT during the temperature sweeps. Additionally, an inhomogeneous surface with a larger amount of defects can require larger voltages to induce the E-MIT. Larger voltages applied at higher temperatures may favor the induction of chemical reactions at the film/IL interface and the formation of oxygen vacancies at the film surface. In the case of VO_2 thin films on TiO_2 (001), instead, the insulating phase is recovered after drop removal. In this case, the scenario of a Mott transition induced by the electrostatic charge accumulation may still be considered to explain the E-MIT.

When the gate voltage is swept at constant temperature, a transition is observed at a certain voltage V_t. This value does not coincide with the critical voltage V_c necessary to cancel the insulating phase during the temperature sweep. Furthermore the value of V_t changes drastically when the sweeps are performed at different constant temperatures because it is related to the conductivity of the IL. Indeed, the two values are related to two different directions of the MIT. An important difference between temperature sweeps and voltage sweeps, in fact, is that in the first case the gate voltage is applied at high temperatures, i.e. when the film is in the metallic phase; in the second case the gate voltage is applied when the film is in the insulating phase. Furthermore, in the temperature sweeps, it takes some time before the transition temperature is reached, so the polarization of the charging of the EDL is completed before the system tends to undergo the MIT. In the voltage sweeps, even if a very small sweeping rate is used, the EDL is not completely polarized for each gate voltage. However, the resistance switch is induced regardless of the direction of the transition. Additionally, with this work, I showed that it is possible to induce a E-MIT starting from a thin film of VO_2 in the monoclinic phase and not only in the rutile phase, as it is found in the literature so far.

Another important difference with respect to the other cases reported in literature regards the crystal direction. Thin films of VO_2 on $LaAlO_3$ (111) have (010) crystal direction. According to the notation used in the previous chapters, the *c* axis of the rutile phase corresponds to the *a* axis of the monoclinic phase. Along this direction, one-dimensional chains of edge-sharing VO_6 octahedra are present. In the (010) crystal direction of the monoclinic phase, the *a* axis lies in-plane. I showed that the E-MIT can be induced also for directions where this axis lies in-plane, contrary to what stated by Jeong *et al*.[86] They attribute the cause of the transition to the removal of oxygen atoms from these chains with consequent expansion along the [001] rutile direction. They explain in this way the experimental observation that no transition is induced for VO_2 grown on TiO_2 with the *c* axis in-plane. However, this hypothesis can still be valid if one considers the grain structure of the VO_2 film on $LaAlO_3$ (111). The IL, in fact, is in contact with the film along the three crystal directions and the VO_2 lattice is not clamped to the substrate lattice unlike VO_2 on TiO_2.

The observation of a double transition in the temperature sweeps of some of the samples analyzed is another effect of the grain structure of the film. The interaction between the IL and the surface of the film may lead to a variation of the strain to which the film is subjected when the IL undergoes a phase transition. This would explain the presence of two transition temperatures during the temperature sweeps. In particular, since the additional transition takes place at lower temperature, the phase transition to rubber phase of the IL would provoke an out-of-plane compressive strain on the film of VO_2.

4. Characterization of the E-MIT in VO_2 on $LaAlO_3$ (111)

In the previous chapter I have described the PLD growth conditions for different oxide thin films, in particular for (111) perovskites. A tunnel junction can be fabricated by growing consecutively the different layers considered as bottom electrode or as tunnel barrier. The growth conditions of the heterostructure, however, may differ from those of the singular layers and have to be defined in such a way that the growth of a new layer does not damage the underlying layers. In this chapter I have reported the optimized conditions used to grow the multilayer consisting of barrier /bottom electrode /$SrTiO_3$ (111). The difficulties related to the growth of such a system stem from the sensitivity of the properties of a perovskite to the presence of defects in the structure and in the composition. Additionally, the polarity of the surface termination along [111] direction makes the surface of each layer unstable and susceptible to reconstructions. The lattice parameter along [111] direction is smaller than the one along [001] direction. To reach a certain thickness, a larger number of unit cells is necessary in the first case and this increases the surface roughness of the thin film. However, I succeeded to grow a multilayer with a very small surface RMS using $LaAlO_3$ as barrier and $SrRuO_3$ or $La_{0.7}Sr_{0.3}MnO_3$ as possible electrodes. The step-and-terrace structure of the substrate is in part reproduced for the last layer. Furthermore, the cross-sectional resistance of the barrier has a resistance at least two orders of magnitude larger than the resistance of the electrode. This shows that the as-grown barrier does not present a large amount of leakage sources. Through the fitting of the tunneling characteristics it was possible to define the effective barrier thicknesses and those values were not coherent with the nominal thicknesses calculated through the number of laser pulses shot on the target during the PLD deposition. This incoherence could be caused by an inhomogeneous barrier. The good quality of the $SrRuO_3$ electrode was not easily reproducible because of the large sensitivity of the growth of this material to the deposition conditions. On the contrary, the properties of the $La_{0.7}Sr_{0.3}MnO_3$ electrode are more stable after multiple growths.

Conclusions

In this thesis, the pulsed laser deposition (PLD) of several transition metal oxides with rutile and perovskite crystal structure on different substrates has been studied. The sensitivity of this class of materials to the growth conditions and to external stimuli has been employed to investigate their behavior in functional electronic devices.

The first result of this work is that the properties of VO_2 thin films grown with PLD depend strongly on the substrate. VO_2 thin films on rutile (001) TiO_2 have strained (001) rutile structure up to a thickness of 10 nm beyond which the film relaxes the strain and microbeams with nonhomogeneous crystal structure form. VO_2 thin films on perovskite (111) $LaAlO_3$ consist of 3D grains with totally relaxed (010) monoclinic structure aligned along three directions separated by 60°. I showed that it is possible to define the grain size, the grain density and the topography of the area between the grains by adjusting the growth deposition conditions. The area between the grains consists either of intermixed film/substrate material with small RMS roughness or of not-aligned 3D islands. The single grains undergo a metal-insulator transition (MIT) with temperature. If the grain density is below the percolation threshold, no global MIT is observed. The characteristics of the MIT depend on the grain properties. In particular, larger grains show better crystallinity and larger width of the MIT. The control of the width of the MIT is crucial for optical devices. Depending on the intended application (e.g. optical memory devices or optical limiters) the width of the MIT must be different (15-20 °C or 3-5 °C, respectively).

Electric double layer transistors (EDLTs) were fabricated using thin films of monoclinic (010) VO_2 on $LaAlO_3$ (111) as a channel. I used DEME-TFSI as ionic liquid (IL) and I built the EDLT with both side-gate and top-gate configuration. The VO_2 films used to build the devices have different properties compared to those found in the literature, where substrates of TiO_2 (001) and Al_2O_3 $(10\bar{1}0)$ were used.[11,12] Unlike the thin films grown on these other two substrates, the VO_2 films fabricated in this work are in the monoclinic phase, grow along the [010] direction and show a peculiar grain structure. These characteristics affect the performance of the EDLT. In particular, the comparison between the behaviors of the thin films grown on different substrates and patterned in EDLT configuration, gives information about the phenomena taking place during the electric-field-induced MIT (E-MIT).

I showed that it is possible to induce a E-MIT in the VO_2 channel at room temperature contrary to what shown in the literature so far. This happens because the transition temperature of the MIT is larger for the relaxed film than for the strained film grown on TiO_2. At room temperature, then, the film is already in the insulating phase and the E-MIT can be induced. At this temperature, however, the leakage current through the drop of IL starts to be significant for smaller gate voltages than in the case where the MIT is induced at 240 K since, at higher temperature, the conductivity of the IL is larger. An increase of the leakage current is an indication of Faradaic reactions taking place at the IL/film interface. The gate voltage inducing the E-MIT at room temperature, however, is smaller than the voltage at which the leakage current starts to increase, so that irreversible reactions at the interface should be prevented.

There are two possible scenarios in the literature describing the observed E-MIT for VO_2 on TiO_2 (001) and Al_2O_3 $(10\bar{1}0)$: an electrostatic Mott transition[11] or electrochemical reactions[86]. In the latter the transition would follow the extraction of oxygen atoms and the consequent expansion of the unit cell along the *c* axis of the rutile structure. This theory is supported by the finding that no E-MIT is observed when the rutile *c* axis lies in-plane, impeding the lattice expansion. The *c* axis of the rutile phase corresponds to the *a* axis of the monoclinic phase. This axis is in-plane for the case of the monoclinic (010) VO_2 thin films shown in this work. This work showed, however, that it is possible to induce the E-MIT. The theory suggesting the formation of oxygen vacancies is also supported by the finding that the insulating state is not recovered once the IL is removed from the device. Note, however, that this has been observed for thin films grown on Al_2O_3 $(10\bar{1}0)$ but not for thin films grown on TiO_2 (001). The scenario that better explains the experimental observations during the E-MIT, then, would depend on the substrate, namely on the properties of the VO_2 thin film. For VO_2 on $LaAlO_3$ (111), we observe that the insulating state is not recovered after removal of the IL. We believe that the formation of oxygen vacancies can be an explanation of the induced metallic state in the samples tested in this work with a behavior similar to that reported for thin films grown on Al_2O_3 $(10\bar{1}0)$. Even if the starting crystal structure is different, the thin films grown on the two substrates are both completely relaxed and show a larger surface RMS compared to the case of films grown on TiO_2 (001). The transition temperatures for the two cases are comparable and the probability of structural defects is larger. These common properties may facilitate the formation of oxygen vacancies when an electric field is applied at the surface. Oxygen vacancies can form even if the monoclinic *a* axis lies in-plane since the grain structure allows for expansion and compression of the film, which is less clamped to the substrate than in the case of the homogeneous VO_2 thin films grown on TiO_2 (001). Unlike VO_2 on TiO_2 (001), then, for which the metallic state may still be induced by electrostatic charge accumulation and consequent Mott transition, the thin films of VO_2 on $LaAlO_3$ (111) tested in this work show indications of oxygen vacancy formation induced by IL gating.

The grain structure of the VO_2 films on $LaAlO_3$ studied in this work influences the interaction between the thin film and the IL because the surface-to-volume ratio for a film made of grains is much larger than for a homogeneous film. The film-to-IL contact area is large and the effect of their interaction is amplified. This could explain the observation of a double transition in the MIT induced with temperature. In particular, a second transition is observed at ≈ 240 K, which is the temperature at which DEME-TFSI transforms to a rubber-phase with increased density. The strain induced at the thin film surface by this denser phase of the IL may justify a reduction of the transition temperature. Given this result, one could think of surface induced strain as an alternative way to tune the transition temperature of the MIT in VO_2.

In parallel to the growth and characterization of VO_2 thin films, I studied the growth of oxide multilayers with a view at the fabrication of functional all-oxide tunnel junctions. The direct measurement of their spectral density of states (DOS) can provide important insight into the physical properties of transition metal oxides. The growth of a tunnel junction is a delicate process since a small amount of structural defects can reduce the effectiveness of the tunneling transport. The control of the quality of the films constituting the junction is essential. PLD is a rather flexible technique which allows for the control of the film stoichiometry, film thickness and film oxygen defect content. Simultaneously, it allows for the growth of thin films with extremely small surface RMS roughness which is a fundamental characteristic when building heterostructures for tunnel junctions. The flexibility is given by the possibility of varying independently different parameters. At the same time, this makes the optimization of the growth process particularly demanding. In this work I optimized the PLD growth of different oxide layers applicable as electrode or barrier layer for a tunnel junction. In particular, I investigated materials having rutile (001) and perovskite (111) structure with views to integrating them in an all-oxide tunnel junction having VO_2 in the electric-field-induced metallic phase as one of the electrodes.

The quality of the film depends on the substrate surface quality and on the growth conditions. The properties of the target used for the growth and the interaction of the elements forming the ablation plume with the background gas also affect the film quality. We observed, for example, that the growth of RuO_2 thin films is extremely sensitive to the oxygen pressure in the chamber for a given substrate temperature, due to the large volatility of Ru. The porosity of the target can lead to the deposition of big particulates on the substrate, as it is in the case of RuO_2 and $SrRuO_3$ film growth. We showed that these effects can be a problem for the growth of a tunnel junction. During the growth of the heterostructure, in fact, the different layers are grown consecutively and at different growth conditions. The presence of dips and particulates on the surface of the bottom electrode prevent the formation of a defect-free barrier, introducing current shorts.

The PLD growth along the [111] direction of the perovskites tested in this work follows a trend common to the different materials. The growth is influenced by the polarity of the layers forming the perovskite structure along this direction. The crystal surface tends to reconstruct because of the polar sequence of the layers forming the crystal which leads to a large surface energy. For this reason, the film starts growing in layer-by-layer mode but the reconstructions roughen the surface until the surface energy is reduced and the film growth can proceed in layer-by-layer mode. The growth-mode sequence can be observed through the *in-situ* measurement of the RHEED intensity. In this work, the same 2D-3D-2D sequence has been observed for the growth of $SrRuO_3$ (111), $LaAlO_3$ (111) and $La_{0.7}Sr_{0.3}MnO_3$ (111).

I optimized the growth of the heterostructures by investigating different materials as bottom electrodes and as tunnel barrier, including RuO_2, TiO_2, $SrRuO_3$, $La_{0.7}Sr_{0.3}MnO_3$ and $LaAlO_3$. Finally, the sequence of materials for the barrier /electrode /substrate heterostructure allowing for the construction of a tunnel junction with reproducible behavior and non-linear I-V characteristic of the tunneling barrier turned out to be: $LaAlO_3$ /$La_{0.7}Sr_{0.3}MnO_3$ /$SrTiO_3$ (111). The $La_{0.7}Sr_{0.3}MnO_3$ films with a thickness of 10 nm had a small RMS roughness and small room-temperature resistivity. The 5 nm thick $LaAlO_3$ layer showed a large barrier resistance. The I-V characteristics can be well fitted by the BDR model, setting the grounds for future analysis of the DOS of the second electrode.

Further investigations need to be performed in order to build a device allowing for the measurement of the DOS of VO_2 after the E-MIT. For this purpose, the patterning of the heterostructure has to be optimized so that the different layers are not damaged during the patterning steps.

In conclusion, this work has demonstrated working field-effect devices at room temperature using thin films of VO_2 on $LaAlO_3$ (111). Our results contribute to clarify the mechanisms taking place during the electric-field-induced MIT in VO_2. In parallel, we demonstrated the feasibility of all-oxide PLD-grown transition metal oxide heterostructures. Our investigations underline the essential role of growth conditions on the performance of these heterostructures. A comprehensive understanding of the factors governing the PLD growth of transition metal oxides and a thorough control over them are necessary to successfully combine different materials into working devices. An important step in this regard, with functional barrier /electrode /substrate heterostructures, was given in this work, paving the way for future efforts towards all-oxide tunnel junction devices.

Appendix

Models for tunneling transport

In a metal-insulator-metal (MIM) junction at the equilibrium, the flow of the electrons through the junction is obstructed by the energetic barrier introduced by the insulating layer. If the insulating film is enough thin, however, the electrons can tunnel through the barrier. When a potential difference V is applied across the junction (with the first electrode M1 being at high potential), the tunneling current density J depends on the tunneling transmission coefficient $\mathrm{T}(E)$, the density of states $\mathrm{D}_2(E)$ and $\mathrm{D}_1\left(E\text{-}eV\right)$ for M2 and M1 and the Fermi-Dirac distributions $f(E)$ and $f(E\text{-}eV)$ of the electrons in M2 and M1, respectively. The measured current density is given by the difference between the current densities flowing in the two directions of the junction and can be expressed by the formula

$$J = J_{2\rightarrow 1} - J_{1\rightarrow 2} = \int_{-\infty}^{+\infty} \mathrm{T}(E)\ \mathrm{D}_2(E)\ \mathrm{D}_1(E\text{-}eV)\ [\,f(E) - f(E\text{-}eV)\,]\ \mathrm{d}E \tag{4}$$

The transmission coefficient depends on the shape of the barrier potential and can be calculated using the Wentzel-Kramers-Brillouin (WKB) approximation. Following Simmons´ model,[224] one considers a junction consisting of metals having the same value of the Fermi level E_F and identical interfaces to the insulator (symmetric junction). Neglecting the effects of temperature and of the image force and considering an average value for the barrier height $\bar{\phi} = \frac{1}{\Delta x}\int_{x_1}^{x_2} \phi(x)\mathrm{d}x$, one obtains the following expression for the transmission coefficient

$$\mathrm{T}(E) \approx \exp\left[-\mathrm{A}\left(\bar{\phi} - E\right)^{1/2}\right] \tag{2}$$

Where E is the energy of the electrons with respect to the Fermi level and $\mathrm{A} = \left(\frac{4\pi\beta t}{h}\right)(2m)^{1/2}$, with t being the barrier thickness, β a correction factor, h the Planck´s constant and m the effective electron mass.

The introduction of this formula in (4) leads, for low applied voltages V, to the following dependence of the current density on the voltage[224]

$$J(V) = \alpha V + \gamma V^3 + \ldots \tag{3}$$

Where (with $\beta = 1$)

$$\alpha = \frac{(2m)^{1/2}}{t}\left(\frac{e}{h}\right)^2 \bar{\phi}^{1/2} \exp\left(-\,\mathrm{A}\,\bar{\phi}^{1/2}\right) \tag{4}$$

$$\frac{\gamma}{\alpha} = \frac{(\mathrm{A}e)^2}{96\bar{\phi}} - \frac{\mathrm{A}e^2}{32\bar{\phi}^{3/2}} \tag{5}$$

The conductance $G(V)$ obtained by (3) is represented by a parabola symmetric about $V = 0$. For an asymmetric barrier the minimum of the parabola is shifted from 0. The effect of the image force is of rounding off the corners of the potential barrier, slightly reducing its thickness.[225] One can also consider the effect of interfacial roughness by calculating the current densities $j(t_n)$ for a distribution of barrier thicknesses t_n and summing these as parallel conduction channels. The *n*th channel is weighted by a coefficient $c(t_n)$ that is obtained from a Gaussian distribution of thicknesses centered at mean thickness $\bar{t}$ with the standard deviation σ defining the roughness. The main effect is an increase in the aperture of the parabola with increased roughness.[226]

Brinkman, Dynes and Rowell (BDR model)[223] considered a trapezoidal junction profile characterized by a position dependence of the barrier height and two different barrier heights ϕ_1 and ϕ_2 for M1 and M2, respectively. The barrier potential has the form $\phi(x,V) = \phi_1 + (x/t)\left(\phi_2 - eV - \phi_1\right)$. Neglecting the effect of the image force and of the temperature, a dependence of the conductance on the voltage similar to the one found in the Simmons´ model is obtained with the difference of a linear term dependent on the quantity $\Delta\phi = \phi_2 - \phi_1$.

$$\frac{G(V)}{G(0)} = 1 - \left(\frac{A_0\Delta\phi}{16\bar{\phi}^{3/2}}\right) eV + \left(\frac{9}{128}\frac{A_0^2}{\bar{\phi}}\right)(eV)^2 \tag{6}$$

Where $A_0 = 4(2m)^{1/2}t/3\hbar$, $G(0) = \left(3.16\times10^{10}\,\bar{\phi}^{1/2}/t\right)\exp\left(-1.025\,\bar{\phi}^{1/2}t\right)$ and $\bar{\phi}$ is the mean barrier height. The variation of $\Delta\phi$ causes a shift of the minimum of the parabola while a variation of $\bar{\phi}$ affects the aperture of the parabola.

For large gate voltages ($V \gg \Delta\phi$), the barrier can be represented like a triangular barrier of maximum height ϕ. In this case, the current density follows the formula (Fowler-Nordheim equation)[227]

$$J = AF^2\, e^{\left(-\frac{B}{F}\right)} \tag{7}$$

Where $A = \frac{e^2}{8\pi h\phi}$, $B = -\frac{4}{3}\sqrt{\frac{8\pi^2 m}{h^2}}\frac{(q\phi)^{3/2}}{e}$ and $F = \frac{V}{t}$ is the effective electric field.

According to the system under study, the measurement of the tunneling current with gate voltage can be fitted by one of the models described, defining the barrier height and the barrier thickness as fitting parameters.

Bibliography

1. Waters, R. As Intel co-founder´s law slows, a rethinking of the chip is needed. *Financ. Times* (2015).

2. Waser, R. *Nanoelectronics and Information Technology*. (Wiley-VCH, 2012).

3. C. N. R. Rao. Transition metal oxides. *Annu. Rev. Phys. Chern.* **40,** 291–326 (1989).

4. Abel, S. *et al.* A strong electro-optically active lead-free ferroelectric integrated on silicon. *Nat. Commun.* **4,** 1671 (2013).

5. Tachikawa, T. *et al.* Metal-to-insulator transition in anatase TiO2 thin films induced by growth rate modulation. *Appl. Phys. Lett.* **101,** 22104 (2012).

6. Goodenough, J. B. The two components of the crystallographic transition in VO2. *J. Solid State Chem.* **3,** 490–500 (1971).

7. Eyert, V. The metal-insulator transitions of VO2: A band theoretical approach. *Ann. Phys.* **11,** 650–702 (2002).

8. Morrison, V. R. *et al.* A photoinduced metal-like phase of monoclinic VO2 revealed by ultrafast electron diffraction. *Science (80-.).* **346,** 445 (2014).

9. Ko, C. & Ramanathan, S. Observation of electric field-assisted phase transition in thin film vanadium oxide in a metal-oxide-semiconductor device geometry. *Appl. Phys. Lett.* **93,** 1–4 (2008).

10. Ruzmetov, D., Gopalakrishnan, G., Ko, C., Narayanamurti, V. & Ramanathan, S. Three-terminal field effect devices utilizing thin film vanadium oxide as the channel layer. *J. Appl. Phys.* **107,** (2010).

11. Nakano, M. *et al.* Collective bulk carrier delocalization driven by electrostatic surface charge accumulation. *Nature* **487,** 459–462 (2012).

12. Jeong, J. *et al.* Suppression of Metal-Insulator Transition in VO2 by Elecrtic Field-Induced Oxygen Vacancy Formation. *Science (80-.).* **339,** 1402–1405 (2013).

13. Nakano, M. *et al.* Distinct Substrate Effect on the Reversibility of the Metal-Insulator Transitions in Electrolyte-Gated VO2 Thin Films. *Adv. Electron. Mater.* **1,** 1500093 (2015).

14. Morris, R. C. & Coleman, R. V. Tunneling measurement of the superconducting energy gap in NbSe2. *Phys. Lett. A* **43,** 11–12 (1973).

15. Richter, C. *et al.* Interface superconductor with gap behaviour like a high-temperature superconductor. *Nature* **502,** 528–31 (2013).

16. Jaffray, J. & Dumas, D. No Title. *J Rech Cent. Natl Rech Sci Lab Bellevue* **5,** 360 (1954).

17. Morin, F. J. Oxides which show a metal-to-insulator transition at the neel temperature. *Phys. Rev. Lett.* **3,** 34–36 (1959).

18. Cavalleri, a., Dekorsy, T., Chong, H. H. W., Kieffer, J. C. & Schoenlein, R. W. Evidence for a structurally-driven insulator-to-metal transition in VO2: A view from the ultrafast timescale. *Phys. Rev. B - Condens. Matter Mater. Phys.* **70,** 1–4 (2004).

19. Ko, C. & Ramanathan, S. Stability of electrical switching properties in vanadium dioxide thin films under multiple thermal cycles across the phase transition boundary. *J. Appl. Phys.* **104,** 086105 (2008).

20. Zhi, B. *et al.* Electric-Field-Modulated Nonvolatile Resistance Switching in VO2/PMN-PT(111) Heterostructures. *ACS Appl. Mater. Interfaces* **6,** 4603–8 (2014).

21. Shibuya, K., Kawasaki, M. & Tokura, Y. Metal-insulator transition in epitaxial V(1−x)WxO2 (0≤x≤0.33) thin films. *Appl. Phys. Lett.* **96,** 022102 (2010).

22. Shin, S. *et al.* Vacuum-ultraviolet reflectance and photoemission study of the metal-insulator phase transitions in VO2, V6O13, and V2O3. *Phys. Rev. B* **41,** 4993–5009 (1990).

23. Ruzmetov, D., Heiman, D., Claflin, B. B., Narayanamurti, V. & Ramanathan, S. Hall carrier density and magnetoresistance measurements in thin-film vanadium dioxide across the metal-insulator transition. *Phys. Rev. B - Condens. Matter Mater. Phys.* **79,** 10–13 (2009).

24. Yang, Z., Ko, C., Balakrishnan, V., Gopalakrishnan, G. & Ramanathan, S. Dielectric and carrier transport properties of vanadium dioxide thin films across the phase transition utilizing gated capacitor devices. *Phys. Rev. B - Condens. Matter Mater. Phys.* **82,** 1–8 (2010).

25. Andersson, G., Parck, C., Ulfvarson, U., Stenhagen, E. & Thorell, B. Studies on Vanadium Oxides. II. The Crystal Structure of Vanadium Dioxide. *Acta Chem. Scand.* **10,** 623–628 (1956).

26. McWhan, D. B., Marezio, M., Remeika, J. P. & Dernier, P. D. X-ray diffraction study of metallic VO2. *Phys. Rev. B* **10,** 490–495 (1974).

27. Granqvist, C. G. Spectrally Selective Coatings for Energy Efficiency and Solar Applications. *Phys. Scr.* **32,** 401 (1985).

28. Lopez, R., Boatner, L. a., Haynes, T. E., Haglund, R. F. & Feldman, L. C. Switchable reflectivity on silicon from a composite VO2-SiO2 protecting layer. *Appl. Phys. Lett.* **85,** 1410–1412 (2004).

29. Zhou, J. *et al.* VO2 thermochromic smart window for energy savings and generation. *Sci. Rep.* **3,** 3029 (2013).

30. Bugayev, a a & Gupta, M. C. Femtosecond holographic interferometry for studies of semiconductor ablation using vanadium dioxide film. *Opt. Lett.* **28,** 1463–1465 (2003).

31. Soltani, M., Chaker, M., Haddad, E., Kruzelecky, R. V. & Nikanpour, D. Optical switching of vanadium dioxide thin films deposited by reactive pulsed laser deposition. *J. Vac. Sci. Technol. A Vacuum, Surfaces, Film.* **22,** 859 (2004).

32. Chivian, J. S., Case, W. E. & Rester, D. H. A 10.6 um Scan Laser with Programmable VO2 mirror. *IEEE Joiurnal Quantum Electron.* **QE-15,** 1326–1328 (1979).

33. Chen, C. & Zhou, Z. Optical phonons assisted infrared absorption in VO2 based bolometer. *Appl. Phys. Lett.* **91,** 011107 (2007).

34. De Almeida, L. A. L. *et al.* Modeling and performance of vanadium–oxide transition edge microbolometers. *Appl. Phys. Lett.* **85,** 3605 (2004).

35. Holsteen, A., Kim, I. S. & Lauhon, L. J. Extraordinary dynamic mechanical response of vanadium dioxide nanowires around the insulator to metal phase transition. *Nano Lett.* **14,** 1898–1902 (2014).

36. Liu, K. *et al.* Giant-amplitude, high-work density microactuators with phase transition activated nanolayer bimorphs. *Nano Lett.* **12,** 6302–6308 (2012).

37. Lee, M. J. *et al.* Two series oxide resistors applicable to high speed and high density nonvolatile memory. *Adv. Mater.* **19,** 3919–3923 (2007).

38. Son, M. *et al.* Excellent selector characteristics of nanoscale VO2 for high-density bipolar ReRAM applications. *IEEE Electron Device Lett.* **32,** 1579–1581 (2011).

39. Driscoll, T., Kim, H. T., Chae, B. G., Di Ventra, M. & Basov, D. N. Phase-transition driven memristive system. *Appl. Phys. Lett.* **95,** (2009).

40. Wu, B. *et al.* Electric-field-driven phase transition in vanadium dioxide. *Phys. Rev. B* **84,** 241410 (2011).

41. Chae, B. G., Kim, H. T., Youn, D. H. & Kang, K. Y. Abrupt metal-insulator transition observed in VO2 thin films induced by a switching voltage pulse. *Phys. B Condens. Matter* **369,** 76–80 (2005).

42. Wentzcovitch, R. M., Schulz, W. W. & Allen, P. B. VO2: Peierls or Mott-Hubbard? A View from Band Theory. *Phys. Rev. Lett.* **72,** 3389 (1994).

43. Zylbersztejn, a & Mott, N. F. Metal-insulator transition in vanadium dioxide. *Phys. Rev. B* **11,** 4383– (1975).

44. Liebsch, A., Ishida, H. & Bihlmayer, G. Coulomb correlations and orbital polarization in the metal-insulator transition of VO2. *Phys. Rev. B - Condens. Matter Mater. Phys.* **71,** 1–5 (2005).

45. Yuan, X., Zhang, Y., Abtew, T. A., Zhang, P. & Zhang, W. VO2: Orbital competition, magnetism, and phase stability. *Phys. Rev. B - Condens. Matter Mater. Phys.* **86,** 1–7 (2012).

46. Marezio, M., McWhan, D. B., Remeika, J. P. & Dernier, P. D. Structural aspects of the metal-insulator transitions in Cr-doped VO2. *Phys. Rev. B* **5,** 2541–2551 (1972).

47. Ghedira, M., Vincent, H., Marezio, M. & Launay, J. C. Structural aspects of the metal-insulator transitions in V0.985Al0.015O2. *J. Solid State Chem.* **22,** 423–438 (1977).

48. Pouget, J. P. *et al.* Dimerization of a linear Heisenberg chain in the insulating phases of V1-xCrxO2. *Phys. Rev. B* **10,** 1801–1815 (1974).

49. Atkin, J. M. *et al.* Strain and temperature dependence of the insulating phases of VO2 near the metal-insulator transition. *Phys. Rev. B - Condens. Matter Mater. Phys.* **85,** 1–4 (2012).

50. Tanaka, H., Takami, H., Kanki, T., Hattori, A. N. & Fujiwara, K. Artificial three dimensional oxide nanostructures for high performance correlated oxide nanoelectronics. *Jpn. J. Appl. Phys.* **53,** 05FA10 (2014).

51. Liu, M. *et al.* Symmetry breaking and geometric confinement in VO2: Results from a three-dimensional infrared nano-imaging. *Appl. Phys. Lett.* **104,** 121905 (2014).

52. Nagashima, K., Yanagida, T., Tanaka, H. & Kawai, T. Influence of ambient atmosphere on metal-insulator transition of strained vanadium dioxide ultrathin films. *J. Appl. Phys.* **100,** 1–5 (2006).

53. Ruzmetov, D., Senanayake, S., Narayanamurti, V. & Ramanathan, S. Correlation between metal-insulator transition characteristics and electronic structure changes in vanadium oxide thin films. *Phys. Rev. B* **77,** 1–5 (2008).

54. Tao, Z. *et al.* Decoupling of Structural and Electronic Phase Transitions in VO2. *Phys. Rev. Lett.* **109,** 1–5 (2012).

55. Kim, H. T. *et al.* Monoclinic and correlated metal phase in VO2 as evidence of the mott transition: Coherent phonon analysis. *Phys. Rev. Lett.* **97,** 10–13 (2006).

56. Pashkin, a. *et al.* Ultrafast insulator-metal phase transition in VO2 studied by multiterahertz spectroscopy. *Phys. Rev. B - Condens. Matter Mater. Phys.* **83,** 1–9 (2011).

57. Yuan, X., Zhang, W. & Zhang, P. Hole-lattice coupling and photoinduced insulator-metal transition in VO2. *Phys. Rev. B - Condens. Matter Mater. Phys.* **88,** 1–6 (2013).

58. Wegkamp, D. *et al.* Instantaneous band gap collapse in photoexcited monoclinic VO2 due to photocarrier doping. *Phys. Rev. Lett.* **113,** 2–6 (2014).

59. Cocker, T. L. *et al.* Phase diagram of the ultrafast photoinduced insulator-metal transition in vanadium dioxide. *Phys. Rev. B - Condens. Matter Mater. Phys.* **85,** 1–11 (2012).

60. Mott, N. F. & Peierls, R. Discussion of the paper by de Boer and Verwey. *Proc. Phys. Soc.* **49,** 72–73 (1937).

61. Hubbard, J. Electron Correlations in Narrow Energy Bands. *Proc. R. Soc. London* **276,** 238 (1963).

62. Kotliar, G. & Vollhardt, D. Strongly Correlated Materials: Insights From Dynamical Mean-Field Theory. *Phys. Today* **57,** 53 (2004).

63. Georges, A., Kotliar, G., Krauth, W. & Rozenberg, M. J. Dynamical mean-field theory of strongly correlated fermion systems and the limit of infinite dimensions. *Rev. Mod. Phys.* **68,** 13–125 (1996).

64. Lee, S., Bock, J. a., Trolier-McKinstry, S. & Randall, C. a. Ferroelectric-thermoelectricity and Mott transition of ferroelectric oxides with high electronic conductivity. *J. Eur. Ceram. Soc.* **32,** 3971–3988 (2012).

65. Edwards, P. P. & Sienko, M. J. Universality aspects of the metal-nonmetal transition in condensed media. *Phys. Rev. B* **17,** 2575–2581 (1978).

66. Brinkman, W. F. & Rice, T. M. Application od Gutzwiller´s Variational Method to the Metal-Insulator Transition. *Phys. Rev. B* **2,** 4302 (1970).

67. Slater, J. C. Magnetic effects and the Hartree-Fock equation. *Phys. Rev.* **82,** 538–541 (1951).

68. McWhan, D. B. & Remeika, J. P. Metal-insulator transition in (V1-xCrx)2O3. *Phys. Rev. B* **2,** 3734–3750 (1970).

69. Gray, A. X. *et al.* Correlation-driven insulator-metal transition in near-ideal vanadium dioxide films. doi:arXiv:1503.07892v1

70. Pergament, A. Metal – insulator transition : the Mott criterion and coherence length. *J. Phys.Condens. Matter* **15,** 3217–3223 (2003).

71. Blanchard, L. a & Hancu, D. Green processing using ionic liquids and CO2. *Nature* **399,** 28–29 (1999).

72. Ono, S., Seki, S., Hirahara, R., Tominari, Y. & Takeya, J. High-mobility, low-power, and fast-switching organic field-effect transistors with ionic liquids. *Appl. Phys. Lett.* **92,** 1–4 (2008).

73. Goldman, a. M. Electrostatic Gating of Ultrathin Films. *Annu. Rev. Mater. Res.* **44,** 45–63 (2014).

74. Kim, B. J., Hwang, E., Kang, M. S. & Cho, J. H. Electrolyte-Gated Graphene Schottky Barrier Transistors. *Adv. Mater.* **27,** 5875–5881 (2015).

75. Helmholtz, H. Ueber einige Gesetze der Vertheilung elektrischer Ströme in körperlichen Leitern mit Anwendung auf die thierisch-elektrischen Versuche. *Pogg Ann* **89,** 211 (1853).

76. Gouy, M. Sur la constitution de la charge électrique á la surface d´un électrolyte. *J Phys Theor Appl* **9,** 457 (1910).

77. Chapman, D. L. A contribution to the theory of electrocapillarity. *Philos. Mag.* **25,** 475 (1965).

78. Stern, O. No Title. *Z Elektrochem* **30,** 508 (1924).

79. Graves, a D. The electrical double layer in molten salts: Part 1. The potential of zero charge. *J. Electroanal. Chem. Interfacial Electrochem.* **25,** 349–356 (1970).

80. Graves, a D. & Inman, D. The electrical double layer in molten salts: Part 2. The double-layer capacitance. *J. Electroanal. Chem. Interfacial Electrochem.* **25,** 357–372 (1970).

81. Fujimoto, T. & Awaga, K. Electric-double-layer field-effect transistors with ionic liquids. *Phys. Chem. Chem. Phys.* **15,** 8983–9006 (2013).

82. Yang, Z., Zhou, Y. & Ramanathan, S. Studies on room-temperature electric-field effect in ionic-liquid gated VO2 three-terminal devices. *J. Appl. Phys.* **111,** 2–6 (2012).

83. Zhou, Y. & Ramanathan, S. Relaxation dynamics of ionic liquid-VO2 interfaces and influence in electric double-layer transistors. *J. Appl. Phys.* **111,** 084508 (2012).

84. Ji, H., Wei, J. & Natelson, D. Modulation of the Electrical Properties of VO2 Nanobeams Using an Ionic Liquid as a Gating Medium. *Nano Lett.* **12,** 2988–2992 (2012).

85. Karel, J. *et al.* Distinct Electronic Structure of the Electrolyte Gate-Induced Conducting Phase in Vanadium Dioxide Revealed Spectroscopy. *ACS Nano* **8,** 5784–5789 (2014).

86. Jeong, J. *et al.* Giant reversible, facet-dependent, structural changes in a correlated-electron insulator induced by ionic liquid gating. *Proc. Natl. Acad. Sci. U. S. A.* **112,** 1013–1018 (2015).

87. Ahn, C. H., Triscone, J.-M. & Mannhart, J. Electric field effect in correlated oxide systems. *Nature* **424,** 1015–1018 (2003).

88. Shukla, N. *et al.* A steep-slope transistor based on abrupt electronic phase transition. *Nat. Commun.* **6,** 7812 (2015).

89. Nakano, M. *et al.* Collective bulk carrier delocalization driven by electrostatic surface charge accumulation. *Nature* **487,** 459–462 (2012).

90. Mannhart, J. & Haensch, W. Device physics: Put the pedal to the metal. *Nature* **487,** 436–437 (2012).

91. Sánchez, A. M. *et al.* Toward all-oxide magnetic tunnel junctions: epitaxial growth of SrRuO3/CoFe2O4/La2/3Sr1/3MnO3 trilayers. *Cryst. Growth Des.* **12,** 954 (2012).

92. Chrisey, D. B. & Hubler, G. K. *Pulsed Laser Deposition of Thin Films*. (1994).

93. Braun, W. *Applied RHEED - Reflection high-Energy Electron Diffraction During Crystal Growth*. (1999).

94. Rijnders, G. J. H. M., Koster, G., Blank, D. H. A. & Rogalla, H. In-situ growth monitoring during PLD of oxides using RHEED at high oxygen pressure. *Mater. Sci. Eng. B* **56,** 223–227 (1998).

95. Phani, G., Tulloch, G., Vittorio, D. & Skryabin, I. Titania solar cells : new photovoltaic technology. *Renew. Energy* **22,** 303–309 (2001).

96. Savage, N. *et al.* Composite n - p semiconducting titanium oxides as gas sensors. *Sensors Actuators B* **79,** 17–27 (2001).

97. Ramires, P. A., Giuffrida, A. & Milella, E. Three-dimensional reconstruction of confocal laser microscopy images to study the behaviour of osteoblastic cells grown on biomaterials. *Biomaterials* **23,** 397–406 (2002).

98. Xi, B. *et al.* TiO2 Thin Films Prepared via Adsorptive Self-Assembly for Self-Cleaning Applications. *ACS Appl. Mater. Interfaces* **4,** 1093 (2012).

99. Czanderna, A. W., Ramachandra, C. N. & Honig, J. M. The anatase-rutile transition. *Trans. Faraday Soc.* **54,** 1069–1073 (1958).

100. Grant, F. A. Properties of Rutile (Titanium dioxide). *Rev. Mod. Phys.* **31,** 646 (1959).

101. Fröhlich, K. *et al.* Epitaxial growth of high-κ TiO2 rutile films on RuO2 electrodes. *J. Vac. Sci. Technol. B Microelectron. Nanom. Struct.* **27,** 266 (2009).

102. Diebold, U. The surface science of titanium dioxide. *Surf. Sci. Rep.* **48,** 53–229 (2003).

103. Müller, K. A. & Burkard, H. SrTiO3: An intrinsic quantum paraelectric below 4 K. **19,** (1979).

104. Sakudo, T. & Unoki, H. Dielectric Properties of SrTiO3 at Low Temperatures. **26,** 851–853 (1971).

105. Sawaguchi, E., Kikuchi, A. & Y, K. Dielectric Constant of Strontium Titanate at Low Temperatures.

106. Grupp, D. E. & Goldman, A. M. Giant Piezoelectric Effect in Strontium Titanate at Cryogenic Temperatures. *Science (80-.).* **276,** 392–394 (1997).

107. Haeni, J. H. *et al.* Room-temperature ferroelectricity in strained SrTiO3. *Nature* **430,** 758 (2004).

108. Ohta, S., Nomura, T., Ohta, H. & Koumoto, K. High-temperature carrier transport and thermoelectric properties of heavily La- or Nb- doped SrTiO3 single crystals. *J. Appl. Phys.* **97,** 034106 (2005).

109. Schooley, J. F., Hosler, W. R. & Cohen, M. L. Superconductivity in semiconducting SrTiO3. *Phys. Rev. Lett.* **12,** 474 (1964).

110. Schooley, J. F., Hosler, W. R., Ambler, E. & Becker, J. H. Dependence of the superconducting transition temperature on carrier concentration in semiconducting SrTiO3. *Phys Rev Lett* **14,** 305–307 (1965).

111. Binnig, G., Baratoff, A., Hoenig, H. E. & Bednorz, J. G. Two-Band Superconductivity in Nb-Doped SrTiO3. *Phys. Rev. Lett.* **45,** 1352 (1980).

112. Kawasaki, M., Maeda, T., Tsuchiya, R. & Koinuma, H. Atomic control of the SrTiO3 Crystal Surface. *Science (80-.).* **226,** 1540 (1994).

113. Chang, J., Park, Y.-S. & Kim, S.-K. Atomically flat single-terminated SrTiO3 (111) surface. *Appl. Phys. Lett.* **92,** 152910 (2008).

114. Simon, R. W. *et al.* Low-loss substrate for epitaxial growth of high-temperature superconductor thin films. *Appl. Phys. Lett.* **53,** 2677 (1988).

115. Yao, J., Merrill, P. B., Perry, S. S., Marton, D. & Rabalais, J. W. Thermal stimulation of the surface termination of LaAlO3 {100}. *J. Chem. Phys.* **108,** 1645–1652 (1998).

116. Hayward, S. a. *et al.* Transformation processes in LaAlO3: Neutron diffraction, dielectric, thermal, optical, and Raman studies. *Phys. Rev. B - Condens. Matter Mater. Phys.* **72,** 1–17 (2005).

117. Liu, Z. Q. *et al.* Atomically flat interface between a single-terminated LaAlO3 substrate and SrTiO3 thin film is insulating. *AIP Adv.* **2,** 0–5 (2012).

118. Abramov, Y. A., Tsirelson, V. G., Zavodnik, V. E., Ivanov, S. A. & Brown, I. D. The chemical bond and atomic displacements in SrTiO3 from X-ray diffraction analysis. *Acta Crystallogr. Sect. B* **51,** 942–951 (1995).

119. Butler, S. R. & Gillson, J. L. Crystal growth, electrical resistivity and lattice parameters of RuO2 and IrO2. *Mater. Res. Bull.* **6,** 81–89 (1971).

120. Koster, G. *et al.* Structure, physical properties, and applications of SrRuO 3 thin films. *Rev. Mod. Phys.* **84,** 253–298 (2012).

121. Suzuki, Y., Hwang, H. Y. & Dover, R. B. Van. The role of strain in magnetic anisotropy of manganite thin films. *Appl. Phys. Lett.* **71,** 140–142 (2001).

122. Jeong, J. *et al.* Suppression of metal-insulator transition in VO2 by electric field-induced oxygen vacancy formation. (Supplementary materials). *Science* **339,** 1402–5 (2013).

123. Kim, B. J., Lee, Y. W., Choi, S. & Kim, H. T. Analysis of the Surface Morphology and the Resistance of VO2 Thin FIlms on M-Plane Al2O3. *J. Korean Phys. Soc.* **50,** 653 (2007).

124. Kim, D. H. & Kwok, H. S. Pulsed laser deposition of VO2 thin films. *Appl. Phys. Lett.* **65,** 3188–3190 (1994).

125. Wong, F. J., Zhou, Y. & Ramanathan, S. Epitaxial variants of VO2 thin films on complex oxide single crystal substrates with 3m surface symmetry. *J. Cryst. Growth* **364,** 74–80 (2013).

126. Schwingenschloegl, U. & Eyert, V. The vanadium Magneli phases VnO(2n-1). 36 (2004). doi:10.1002/andp.200410099

127. Katzke, H., Toledano, P. & Depmeier, W. Theory of morphotropic transformations in vanadium oxides. *Phys. Rev. B* **68,** 024109 (2003).

128. Griffiths, C. H. & Eastwood, H. K. Influence of stoichiometry on the metal-semiconductor transition in vanadium dioxide. *J. Appl. Phys.* **45,** 2201–2206 (1974).

129. Bahlawane, N. & Lenoble, D. Vanadium oxide compounds: Structure, properties, and growth from the gas phase. *Chem. Vap. Depos.* **20,** 299–311 (2014).

130. Yang, Z., Ko, C. & Ramanathan, S. Oxide Electronics Utilizing Ultrafast Metal-Insulator Transitions. *Annu. Rev. Mater. Res.* **41,** 337–367 (2011).

131. Koide, S. & Takei, H. Epitaxial growth of VO2 single crystals and their anisotropic properties in electrical resistivities. *J. Phys. Soc. Japan* **22,** 946–947 (1967).

132. Makarevich, A. M. *et al.* Chemical synthesis of high qiality epitaxial vanadium dioxide films with sharp electrical and optical switch properties. *J. Mater. Chem. C* **3,** 9197–9205 (2015).

133. Zhang, H. *et al.* Wafer-scale growth of VO2 thin films using a combinatorial approach. *Nat. Commun.* **6,** 1–8 (2015).

134. Tashman, J. W. *et al.* Epitaxial growth of VO2 by periodic annealing. *Appl. Phys. Lett.* **104,** 2012–2017 (2014).

135. Borek, M., Qian, F., Nagabushnam, V. & Singh, R. K. Pulsed laser deposition of oriented VO2 thin films on R-cut sapphire substrates. *Appl. Phys. Lett.* **63,** 3288–3290 (1993).

136. Garry, G., Durand, O. & Lordereau, a. Structural, electrical and optical properties of pulsed laser deposited VO2 thin films on R- and C-sapphire planes. *Thin Solid Films* **453-454,** 427–430 (2004).

137. Narayan, J. & Bhosle, V. M. Phase transition and critical issues in structure-property correlations of vanadium oxide. *J. Appl. Phys.* **100,** (2006).

138. Bialas, H., Dillenz, a, Downar, H. & Ziemann, P. Epitaxial relationships and electrical properties of vanadium oxide films on r-cut sapphire. *Thin Solid Films* **338,** 60–69 (1999).

139. Wu, Z. P. *et al.* Single-crystalline epitaxy and twinned structure of vanadium dioxide thin film on (0001) sapphire. *J. Phys. Condens. Matter* **10,** L765–L771 (1999).

140. Muraoka, Y. & Hiroi, Z. Metal-insulator transition of VO2 thin films grown on TiO 2 (001) and (110) substrates. *Appl. Phys. Lett.* **80,** 583–585 (2002).

141. Nagashima, K., Yanagida, T., Tanaka, H. & Kawai, T. Interface effect on metal-insulator transition of strained vanadium dioxide ultrathin films. *J. Appl. Phys.* **101,** 21–23 (2007).

142. Sambi, M., Sangiovanni, G., Granozzi, G. & Parmigiani, F. Growth and the structure of epitaxial VO2 at the TiO2 (110) surface. *Phys. Rev. B* **55,** 7850–7858 (1997).

143. Lappalainen, J., Heinilehto, S., Saukko, S., Lantto, V. & Jantunen, H. Microstructure dependent switching properties of VO2 thin films. *Sensors Actuators, A Phys.* **142,** 250–255 (2008).

144. Berglund, C. & Jayaraman, a. Hydrostatic-Pressure Dependence of the Electronic Properties of VO, Near the Semiconductor-Metal Transition Temperature. *Phys. Rev.* **1022,** (1969).

145. Liu, M. *et al.* Phase transition in bulk single crystals and thin films of VO2 by nanoscale infrared spectroscopy and imaging. *Phys. Rev. B* **91,** 245155 (2015).

146. Liu, M., Wagner, M., Zhang, J., Mcleod, A. & Basov, D. N. Symmetry breaking and geometric confinement in VO2: Results from a three-dimensional infrared nano-imaging. *Appl. Phys. Lett.* **104,** 121905 (2014).

147. Ohring, M. *Materials Science of Thin Films*. (Academic Press, 2001).

148. Suh, J. Y., Lopez, R., Feldman, L. C. & Haglund, R. F. Semiconductor to metal phase transition in the nucleation and growth of VO2 nanoparticles and thin films. *J. Appl. Phys.* **96,** 1209–1213 (2004).

149. Aliev, R. A. *et al.* Effect of Grain Sizes on the Metal – Semiconductor Phase Transition in Vanadium Dioxide Polycrystalline Thin Films. *Phys. Solid State* **48,** 929–934 (2006).

150. Lopez, R., Haynes, T., Boatner, L., Feldman, L. & Haglund, R. Size effects in the structural phase transition of VO2 nanoparticles. *Phys. Rev. B* **65,** 224113 (2002).

151. Nazari, M. *et al.* Finite size effect on the phase transition of vanadium dioxide. *Appl. Phys. Lett.* **103,** 043108 (2013).

152. Pauli, S. A. *et al.* X-ray diffraction studies of the growth of vanadium dioxide nanoparticles. *J. Appl. Phys.* **102,** 073527 (2007).

153. Klimov, V. A., Timofeeva, I. O., Khanin, S. D. & Shadrin, E. B. Hysteresis Loop Construction for the Metal – Semiconductor Phase Transition in Vanadium Dioxide Films. *Tech. Phys.* **47,** 1134–1139 (2002).

154. Challa, M. S. S. & Landau, D. P. Finite-size effects at temperature-driven first-order transition. *Phys. Rev. B* **34,** 1841 (1986).

155. Qazilbash, M. M. *et al.* Electrodynamics of the vanadium oxides VO2 and V2O3. *Phys. Rev. B* **77,** 115121 (2008).

156. Elbaum, L. K., Wittmer, M., Yee, D. S., Wittmer, M. & Vee, D. S. Characterization of reactively sputtered ruthenium dioxide for very large scale integrated metallization. *Appl. Phys. Lett.* **1879,** 50–53 (1987).

157. Wittmer, M. Barrier layers : Principles and applications in microelectronics. *J. Vac. Sci. Technol. A Vacuum, Surfaces, Film.* **2,** 273 (1984).

158. Kolawa, E. *et al.* Reactively sputtered RuO2 diffusion barriers. *Appl. Phys. Lett.* **50,** 854 (1987).

159. Jia, Q. X. & Anderson, W. A. Sputter deposition of YBa2Cu3O7−x films on Si at 500 °C with conducting metallic oxide as a buffer layer. *Appl. Phys. Lett.* **57,** 304 (1990).

160. Jia, Q. X. *et al.* Role of substrates for heteroepitaxial growth of low roomtemperature resistivity RuO2 thin films deposited by pulsed laser deposition. *J. Vac. Sci. Technol. A Vacuum, Surfaces, Film.* **14,** 1107 (1996).

161. Gibert, M., Zubko, P., Scherwitzl, R., Íñiguez, J. & Triscone, J. Exchange bias in LaNiO 3 – LaMnO 3 superlattices. *Nat. Mater.* **11,** 195–198 (2012).

162. Aydogdu, G. H., Kuru, Y. & Habermeier, H. Structural and electrical properties of La0.5Ca0.5MnO3 films deposited on differently oriented SrTiO3 substrates. *Mater. Sci. Eng. B* **144,** 123–126 (2007).

163. Chakraverty, S., Ohtomo, A., Okude, M. & Ueno, K. Epitaxial Structure of (001)- and (111)-Oriented Perovskite Ferrate Films Grown by Pulsed-Laser Deposition. *Cryst. Growth Des.* **10,** 1725 (2010).

164. Chang, J., Lee, J. & Kim, S. Layer-by-layer growth of SrFeO(3-d) thin films on atomically flat single-terminated SrRuO3/SrTiO3 (111) surfaces. *J. Cryst. Growth* **312,** 621–623 (2010).

165. Gray, B. *et al.* Local electronic and magnetic studies of an artificial La2FeCrO6 double perovskite. *Appl. Phys. Lett.* **97,** 013105 (2010).

166. Lee, M. K. *et al.* Synthesis and properties of epitaxial thin films of c-axis oriented metastable four- layered hexagonal BaRuO 3 Synthesis and properties of epitaxial thin films of c-axis oriented. *Appl. Phys. Lett.* **77,** 364 (2000).

167. Middey, S. *et al.* Epitaxial growth of (111)-oriented LaAlO3 / LaNiO3 ultra-thin superlattices. *Appl. Phys. Lett.* **101,** 261602 (2012).

168. Tasker, P. W. The stability of ionic crystal surfaces. *J. Phs. C Solid State Phys.* **12,** 4977 (1979).

169. Noguera, C. Polar oxide surfaces. *J. Phys.Condens. Matter* **12,** R367 (2000).

170. Nakagawa, N., Hwang, H. Y. & Muller, D. A. Why some interfaces cannot be sharp. *Nat. Mater.* **5,** 204–209 (2006).

171. Blok, J. L., Wan, X., Koster, G., Blank, D. H. A. & Rijnders, G. Epitaxial oxide growth on polar (111) surfaces. *Appl. Phys. Lett.* **99,** 151917 (2011).

172. Scott, J. F. *Ferroelectric Memories*. (2000).

173. Gausepohl, S. C., Lee, M., Antognazza, L. & Char, K. Magnetoresistance probe of spatial current variations in high-Tc YBa2Cu3O7-SrRuO3-YBa 2Cu3O7 Josephson junctions. *Appl. Phys. Lett.* **67,** 1313 (1995).

174. Takahashi, K. S. *et al.* Inverse tunnel magnetoresistance in all-perovskite junctions of La0.7Sr0.3Mn03/SrTiO3/SrRuO3. *Phys. Rev. B* **67,** 094413 (2003).

175. Chen, C. L. *et al.* Epitaxial SrRuO3 thin films on (001) SrTiO3. *Appl. Phys. Lett.* **71,** 1047 (1997).

176. Rijnders, G., Blank, D. H. a, Choi, J. & Eom, C. B. Enhanced surface diffusion through termination conversion during epitaxial SrRuO3 growth. *Appl. Phys. Lett.* **84,** 505–507 (2004).

177. Gan, Q., Rao, R. a. & Eom, C. B. Control of the growth and domain structure of epitaxial SrRuO3 thin films by vicinal (001) SrTiO3 substrates. *Appl. Phys. Lett.* **70,** 1962 (1997).

178. Jiang, J. C., Pan, X. Q. & Chen, C. L. Microstructure of epitaxial SrRuO 3 thin films on (001) SrTiO 3. *Appl. Phys. Lett.* **72,** 909–911 (1998).

179. Maria, J.-P., Trolier-McKinstry, S., Schlom, D. G., Hawley, M. E. & Brown, G. W. The influence of energetic bombardment on the structure and

properties of epitaxial SrRuO3 thin films grown by pulsed laser deposition. *J. Appl. Phys.* **83,** 4373 (1998).

180. Zakharov, N. D., Satyalakshmi, K. M., Koren, G. & Hesse, D. Substrate temperature dependence of structure and resistivity of SrRuO3 thin films grown by pulsed laser deposition on (100) SrTiO3. *J. Mater. Res.* **14,** 4385–4394 (1999).

181. Choi, J., Eom, C. B., Rijnders, G., Rogalla, H. & Blank, D. H. a. Growth mode transition from layer by layer to step flow during the growth of heteroepitaxial SrRuO3 on (001) SrTiO3. *Appl. Phys. Lett.* **79,** 1447–1449 (2001).

182. Chang, J., Lee, J. W. & Kim, S. K. Layer-by-layer growth of SrFeO3-?? thin films on atomically flat single-terminated SrRuO3/SrTiO3 (111) surfaces. *J. Cryst. Growth* **312,** 621–623 (2010).

183. Rubi, D., Vlooswijk, a. H. G. & Noheda, B. Growth of flat SrRuO3 (111) thin films suitable as bottom electrodes in heterostructures. *Thin Solid Films* **517,** 1904–1907 (2009).

184. Foerster, M., Piano, S., Rigato, F., Mellor, C. J. & Fontcuberta, J. Andreev reflection and spin polarization of SrRuO3 thin films on SrTiO3 (111). *J. Phys. Conf. Ser.* **303,** 012068 (2011).

185. Funakubo, H., Oikawa, T., Higashi, N. & Saito, K. Metal organic chemical vapor deposition growth of epitaxial SrRuO3 and CaRuO3 thin films with different orientations as the bottom electrode for epitaxial ferroelectric thin film. *J. Cryst. Growth* **235,** 401–406 (2002).

186. Sumi, a. *et al.* MOCVD growth of epitaxial SrIrO3 films on (111)SrTiO3 substrates. *Thin Solid Films* **486,** 182–185 (2005).

187. Chang, J., Lee, J. W. & Kim, S. K. Layer-by-layer growth of SrFeO(3-d) thin films on atomically flat single-terminated SrRuO3/SrTiO3 (111) surfaces. *J. Cryst. Growth* **312,** 621–623 (2010).

188. Toyota, D. *et al.* Thickness-dependent electronic structure of ultrathin SrRuO3 films studied by in situ photoemission spectroscopy. *Appl. Phys. Lett.* **87,** 162508 (2005).

189. Boschker, H. *et al.* Optimized fabrication of high-quality La0.67Sr0.33MnO3 thin films considering. *j. Phys. D Appl. Phys.* **44,** 205001 (2011).

190. Donnell, J. O. *et al.* Colossal magnetoresistance magnetic tunnel junctions grown by molecular-beam epitaxy. *Appl. Phys. Lett.* **76,** 1914 (2000).

191. Bowen, M. *et al.* Nearly total spin polarization in La2/3Sr1/3MnO3 from tunneling experiments. *Appl. Phys. Lett.* **82,** 233 (2003).

192. Postma, F. M. *et al.* Epitaxial diodes of a half-metallic ferromagnet on an oxide semiconductor. *J. Appl. Phys.* **95,** 7324 (2004).

193. Hikita, Y., Nishikawa, M., Yajima, T. & Hwang, H. Y. Termination control of the interface dipole in La0.7Sr0.3MnO3/Nb:SrTiO3 (001) Schottky junctions. *Phys. Rev. B* **79,** 073101 (2009).

194. Garcia, V. *et al.* Giant tunnel electroresistance for non-destructive readout of ferroelectric states. *Nature* **460,** 81 (2009).

195. Eerenstein, W., Wiora, M., Prieto, J. L., Scott, J. F. & Mathur, N. D. Giant sharp and persistent converse magnetoelectric effects in multiferroic epitaxial heterostructures. *Nat. Mater.* **6,** 348 (2007).

196. Hajo, J. *et al.* Magnetoelectric Effects in Complex Oxides with Competing Ground States. *Adv. Mater.* **2T,** 3470–3474 (2009).

197. Dagotto, E., Hotta, T. & Moreo, A. Colossal magnetoresistant materials: the key role of phase separation. *Phys. Rep.* **344,** 1–153 (2001).

198. Hallsteinsen, I., Boschker, J. E., Nord, M., Lee, S. & Rzchowski, M. Surface stability of epitaxial La0.7Sr0.3MnO3 thin films on (111)-oriented SrTiO3. *J. Appl. Phys.* **113,** 183512 (2013).

199. Chang, J., Park, Y., Lee, J. & Ã, S. K. Layer-by-layer growth and growth-mode transition of SrRuO3 thin films on atomically flat single-terminated SrTiO3(111) surfaces. *J. Cryst. Growth* **311,** 3771–3774 (2009).

200. Urushibara, a., Arima, T., Asamitsu, A., Kido, G. & Tokura, Y. Insulator-metal transition and giant magnetoresistance in La1-xSrxMnO3. *Phys. Rev. B* **51,** 14103–14109 (1995).

201. Stankevic, V. *et al.* Uniaxial stress influence on electrical conductivity of thin epitaxial lanthanum-strontium manganite films. *Thin Solid Films* **540,** 194–201 (2013).

202. Balevicius, S. *et al.* Two-phase structure of ultra-thin La-Sr-MnO films. *Thin Solid Films* **515,** 691–694 (2006).

203. Z, L. *et al.* Origin of the metal-insulator transition in ultrathin films of La2/3Sr1/3MnO3. *Phys. Rev. B* **92,** 125123 (2015).

204. Angeloni, M. *et al.* Suppression of the metal-insulator transition temperature in thin La0.7Sr0.3MnO films. *J. Appl. Phys.* **96,** 6387 (2004).

205. Huijben, M. *et al.* Critical thickness and orbital ordering in ultrathin La0.7Sr0.3MnO3 films. *Phys. Rev. B* **78,** 094413 (2008).

206. Tebano, A. *et al.* Evidence of orbital reconstruction at interfaces in ultrathin La0.67Sr0.33MnO3 Films. *Phys. Rev. Lett.* **100,** 2–5 (2008).

207. Hallsteinsen, I. *et al.* Crystalline symmetry controlled magnetic switching in epitaxial (111) La0.7Sr0.3MnO3 thin films. *APL Mater.* **3,** 0–7 (2015).

208. Ohtomo, a & Hwang, H. Y. A high-mobility electron gas at the LaAlO3/SrTiO3 heterointerface. *Nature* **427,** 423–426 (2004).

209. Mannhart, J. & Schlom, D. G. Oxide Interfaces - An opportunity for Electronics. *Science (80-.).* **327,** 1607–1611 (2010).

210. Liao, Y. C., Kopp, T., Richter, C., Rosch, A. & Mannhart, J. Metal-insulator transition of the LaAlO3-SrTiO3 interface electron system. *Phys. Rev. B* **83,** 075402 (2011).

211. Herranz, G., Sánchez, F., Dix, N., Scigaj, M. & Fontcuberta, J. High mobility conduction at (110) and (111) LaAlO3/SrTiO3 interfaces. *Sci. Rep.* **2,** 3–7 (2012).

212. Atanacio, A. J., Bak, T. & Nowotny, J. Niobium Segregation in Niobium Doped Titanium Dioxide (Rutile). *J. Phys. Chem. C* **118,** 11174 (2014).

213. Sheppard, L. R. Niobium surface segregation in polycrystalline niobium-doped titanium dioxide. *J. Phys. Chem. C* **117,** 3407–3413 (2013).

214. Bibes, M. *et al.* Growth and characterization of TiO2 as a barrier for spin-polarized tunneling. *Appl. Phys. Lett.* **82,** 3269–3271 (2003).

215. Hikita, Y., Susaki, T., Takagi, H. & Hwang, H. Y. Characterization of the Schottky Barrier in SrRuO3/Nb:SrTiO3 Junctions. at <https://arxiv.org/ftp/cond-mat/papers/0703/0703358.pdf>

216. Rana, K. G., Khikhlovskyi, V. & Banerjee, T. Electrical transport across Au/Nb:SrTiO 3 Schottky interface with different Nb doping. *Appl. Phys. Lett.* **100,** 98–101 (2012).

217. Russell, B. C. & Castell, M. R. (13x13)R13.9° and (7x7)R19.1° reconstructions of the polar SrTiO3 (111) surface. *Phys. Rev. B - Condens. Matter Mater. Phys.* **75,** 1–7 (2007).

218. Sekiguchi, S. Atomic force microscopic observation of SrTiO3 polar surface. *Solid State Ionics* **108,** 73–79 (1998).

219. Sato, T., Masuda, G. & Takagi, K. Electrochemical properties of novel ionic liquids for electric double layer capacitor applications. *Electrochim. Acta* **49,** 3603–3611 (2004).

220. McCann, D. M., Misek, M., Kamenev, K. V. & Huxley, A. D. Pressure-Temperature Phase Diagram of Ionic Liquid Dielectric DEME-TFSI. *Phys. Procedia* **75,** 252–258 (2015).

221. Pfanzelt, G. Herstellung von Heterostrkuturen mit integrierten Flüssigkeitsvolumima. (2016).

222. Hormoz, S. & Ramanathan, S. Limits on vanadium oxide Mott metal-insulator transition field-effect transistors. *Solid. State. Electron.* **54,** 654–659 (2010).

223. Brinkman, W. F., Dynes, R. C. & Rowell, J. M. Tunneling conductance of asymmetrical barriers. *J. Appl. Phys.* **41,** 1915–1921 (1970).

224. Simmons, J. G. Generalized Formula for the Electric Tunnel Effect between Similar Electrodes Separated by a Thin Insulating Film. *J. Appl. Phys.* **34,** 1793–1803 (1963).

225. Wolf, E. L. *Principles of electron tunneling spectroscopy*. (Oxford University Press, 1985).

226. Miller, C. W., Li, Z. P., Åkerman, J. & Schuller, I. K. Impact of interfacial roughness on tunneling conductance and extracted barrier parameters. *Appl. Phys. Lett.* **90,** 88–91 (2007).

227. Simmons, J. G. Electric Tunnel Effect between Dissimilar Electrodes Separated by a Thin Insulating Film. *J. Appl. Phys.* **2581,** 2581 (1963).